ISSN: 2150-4091 (Print), 2150-4105 (Online) Volume 1, Number 1, June 2009

Scientific Research

# Natural Science

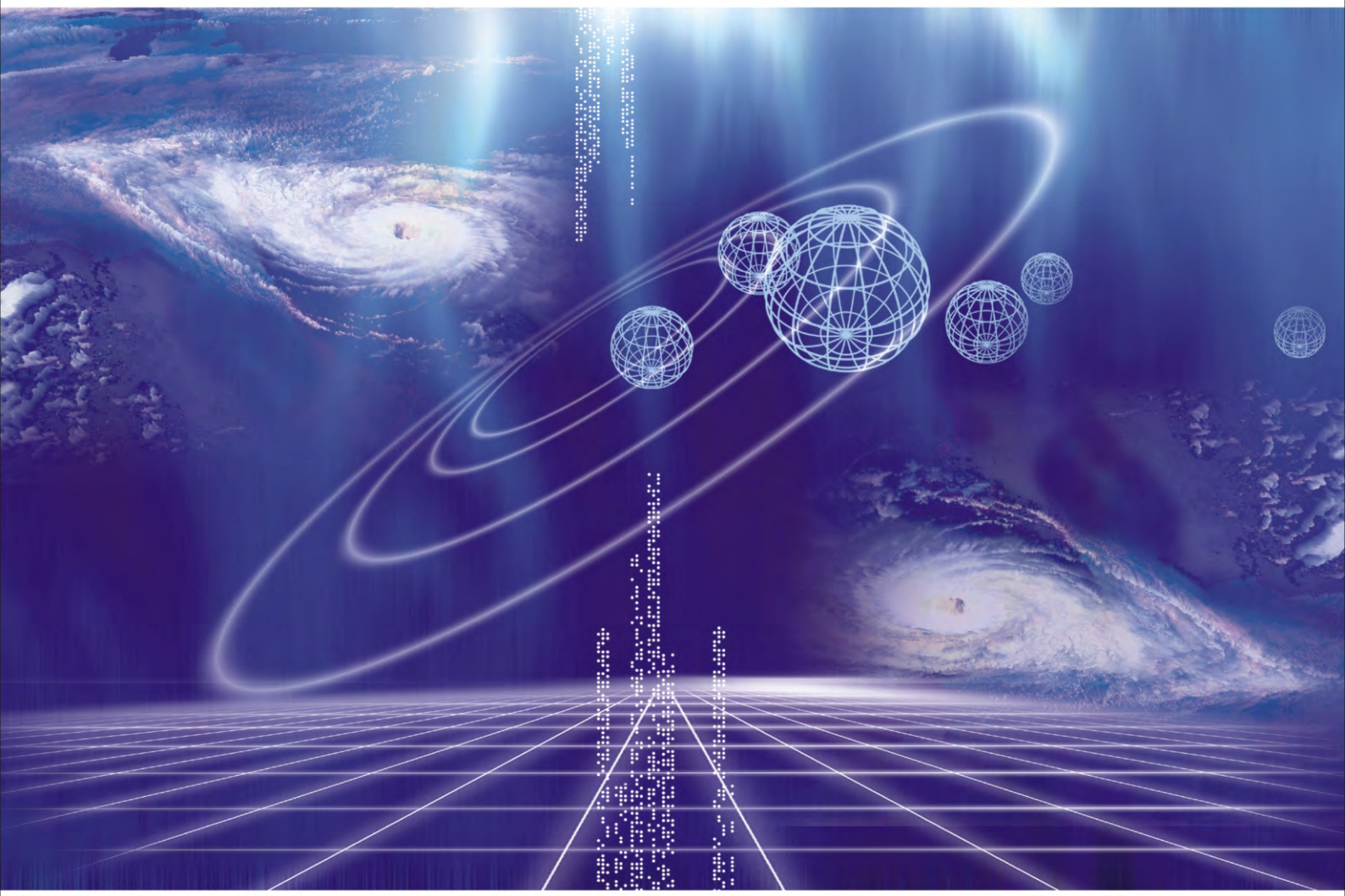

www. scirp. org/journal/ns/

# Journal Editorial Board

ISSN: 2150-4091 (Print) ISSN: 2150-4105 (Online)
http://www.scirp.org/journal/ns/

**Natural Science, 2009, 1, 1-62**
Published Online June 2009 in SciRes (http://www.SciRP.org/journal/NS).

# TABLE OF CONTENTS

## Volume 1, Number 1, June 2009



 

# Natural Science

# Journal Information

## SUBSCRIPTIONS

The *Natural Science* (Online at Scientific Research Publishing, www.SciRP.org) is published quarterly by Scientific Research Publishing, Inc., USA.

E-mail: ns@scirp.org

**Subscription rates:** Volume 1 2009

Print: $50 per copy.

Electronic: free, available on www.SciRP.org.

To subscribe, please contact Journals Subscriptions Department, E-mail: ns@scirp.org

**Sample copies:** If you are interested in subscribing, you may obtain a free sample copy by contacting Scientific Research Publishing, Inc at the above address.

## SERVICES

**Advertisements**

Advertisement Sales Department, E-mail: ns@scirp.org

**Reprints (minimum quantity 100 copies)**

Reprints Co-ordinator, Scientific Research Publishing, Inc., USA.

E-mail: ns@scirp.org

## COPYRIGHT



## PRODUCTION INFORMATION

For manuscripts that have been accepted for publication, please contact:

E-mail: ns@scirp.org

**Natural Science, 2009, 1, 1-1**

# News and Announcement

We are pleased to announce that the Editorial Board Member of **NS**, Kuo-Chen Chou, has been identified by Science Watch (http://sciencewatch.com/ana/fea/09maraprFea/) as the author with the highest numbers of Hot Papers published over the preceding two years (2007 and 2008). Among the 13 authors listed in the table of "Scientists with Multiple Hot Papers" by Science Watch, Professor Dr. Kuo-Chen Chou of Gordon Life Science institute and Shanghai Jiaotong University ranks No.1 with 17 hot papers.

Meanwhile, the review article by Kuo-Chen Chou and Hong-Bin Shen, entitled "Recent Progresses in Protein Subcellular Location Prediction" published in Analytical Biochemistry, has been identified by Science Watch as the New Hot Paper in the field of Biology & Biochemistry (http://sciencewatch.com/dr/nhp/2009/09marnhp/09marnhpChou/).

For more information about the hot research and hot papers, go to visit the web-sites at http://www.sciencenet.cn/htmlnews/2009/3/216833.html; http://sciencewatch.com/ana/fea/pdf/09maraprFea.pdf; and http://sciencewatch.com/dr/nhp/2009/pdf/09marnhpChou.pdf.

Please join us to send our sincere and warm congratulations to our fellow board member, Kuo-Chen Chou, for his prominent contributions in science. Meanwhile, we hope this announcement can attract more researchers to submit their best papers to **NS**, the journal that publishes the highest quality of research and review articles in all important aspects of natural sciences and their intersection.

**NS** Editorial Office

**Natural Science, 2009, 1, 2-9** **NS**

# Structural mapping of coastal plain sands using engineering geophysical technique: Lagos Nigeria case study

**A. A. Adepelumi[1], M. O. Olorunfemi[2], D. E. Falebita[3], O.G. Bayowa[4]**

[1,2,3]Department of Geology, Obafemi Awolowo University, Ile-Ife, Nigeria; [4]Department of Earth Sciences, Ladoke Akintola University, Ogbomoso, Nigeria. [1]Phone: +234-8067163658.
Corresponding author: [1]adepelumi@yahoo.co.uk

Received 20 May 2009; revised 1 June 2009; accepted 2 May 2009.

## ABSTRACT

**An engineering geological survey using the cone penetrometer and finite element method was carried out to characterize sand-fill thicknesses in a reclaimed area of Lagos, SW Nigeria. A previously developed finite element program was modified in order to allow for predicting the sand-fill thicknesses, and have an understanding of the geomorphic shallow structures existing pre-sand-fill. The program was tested using the obtained cone penetrometer test results from the Lekki-Peninsula area. The finite element predicted thicknesses show good correlation with the penetrometer obtained thicknesses. Six zones with thick sand-fill thicknesses varying from 1.25 to 6.0m were identified from the isopach maps, these zones correlate with major/minor depression associated with river/stream channels and creeks. These are the main shallow geomorphic structural features present in the area pre-sand fill. The structural trends of the depressions are largely influenced by the oceanic fracture pattern.**

**Keywords:** Sand-Fill; Finite Element; Nigeria; Penetrometer; Depression

## 1. INTRODUCTION

Engineering site investigation requires determination of thicknesses either to competent bedrock in foundation works or of sand-fill columns in a reclaimed site. Accurate mapping of bedrock topography or reliable estimation of sand-fill in a reclaimed site requires that thicknesses are known at several test points. The more the number of test points, the better the bedrock topography definition and the more accurate is the estimation of spatial volume. However, the more the number of test points, the higher is the cost of investigation and the longer is the survey duration, most especially where the survey area runs into tens of square kilometers [1].

Geophysical methods, cone penetrometer tests, and direct borehole drilling are some of the various means of determining thicknesses or depths to a particular bedrock [2,3,4]. Of the three methods outlined above, geophysical methods remain the cheapest. But geophysical data interpretation requires some level of control usually in terms of subsurface information (e.g. lithological logs) obtained from drilling. Hence geophysical investigation is often complemented by borehole investigation with a consequently increasing cost. Survey cost and duration can be reduced if a predictive technique, with significant level of accuracy, can be developed that utilises few initial accurately determined thicknesses to predict thicknesses at other location where tests have not been carried out.

Finite element automated approach to the prediction of heads have been utilised by a number of authors. These include Fenner [5], Agbede [6] and Wang and Anderson [7]. These methods are iterative procedures that utilise various elemental geometries such as polygons, rectangles and triangles. The Finite element program, developed by Wang and Anderson [7] was slightly modified and used to predict formation thicknesses. The viability of the technique was tested using cone penetrometer test results from a reclaimed Lekki Peninsula area of Lagos. In the present study, the main objective is to determine the thicknesses of sand-fill using the cone penetrometer tests and finite element methods. And, to have an understanding of the geomorphic shallow structures existing pre sand-fill in the reclaimed Lekki Peninsula area of Lagos Nigeria.

## 2. THE STUDY AREA

The Lekki-Peninsula area of Lagos was reclaimed by hydraulic sand-fill. It is located within the western coastal zone which consists largely of coastal creeks and lagoons developed by barrier beaches associated with sand deposition [8,9]. The study area can be found in the south eastern part of Lagos State, southwest, Nigeria, lying between latitude 6° 25'44.62" and 6° 27'38.16" N

and longitudes 3° 27'16.70" and 3° 28' 55.80 E (**Fig. 1**).

The surface geology of the study area is made up of the Benin Formation (Miocene to Recent), recent littoral alluvial, lagoons and coastal plain sand deposits. The sand range in size from coarse to medium grained clean white loose sandy soil which graded into one another towards the lagoons and near the mouth of the larger rivers. The low-lying beach ridges of sand called berm and barrier beach ridges of sand are ubiquitous in the area and are said to be derived from one or more of the following, sand brought in along the coast and reworked alluvial sands originally deposited by the south flowing rivers drawing the Dahomey basement of the western Nigerian during the late Pleistocene, Wurm-Wisconsn [10]. The superficial deposit in the pre-sand fill is composed mainly of the clay/peat deposits. The recent littoral and alluvium deposits, the continental Benin sands and the Ilaro Formations were identified as the major aquifers. The water bearing aquifers consist of sands, gravels or a mixture of the two [11]. Within Lagos metropolis, three major aquifer zones at depths shallower than 200 m were delineated. The first is a water table aquifer that is prone to pollution. The second and third aquifers are confined aquifers made up of an alternating sequence of sand and clay. They are harnessed through boreholes and are the basis of mini-water works in Lagos area. The third aquifer is the most productive and most exploited.

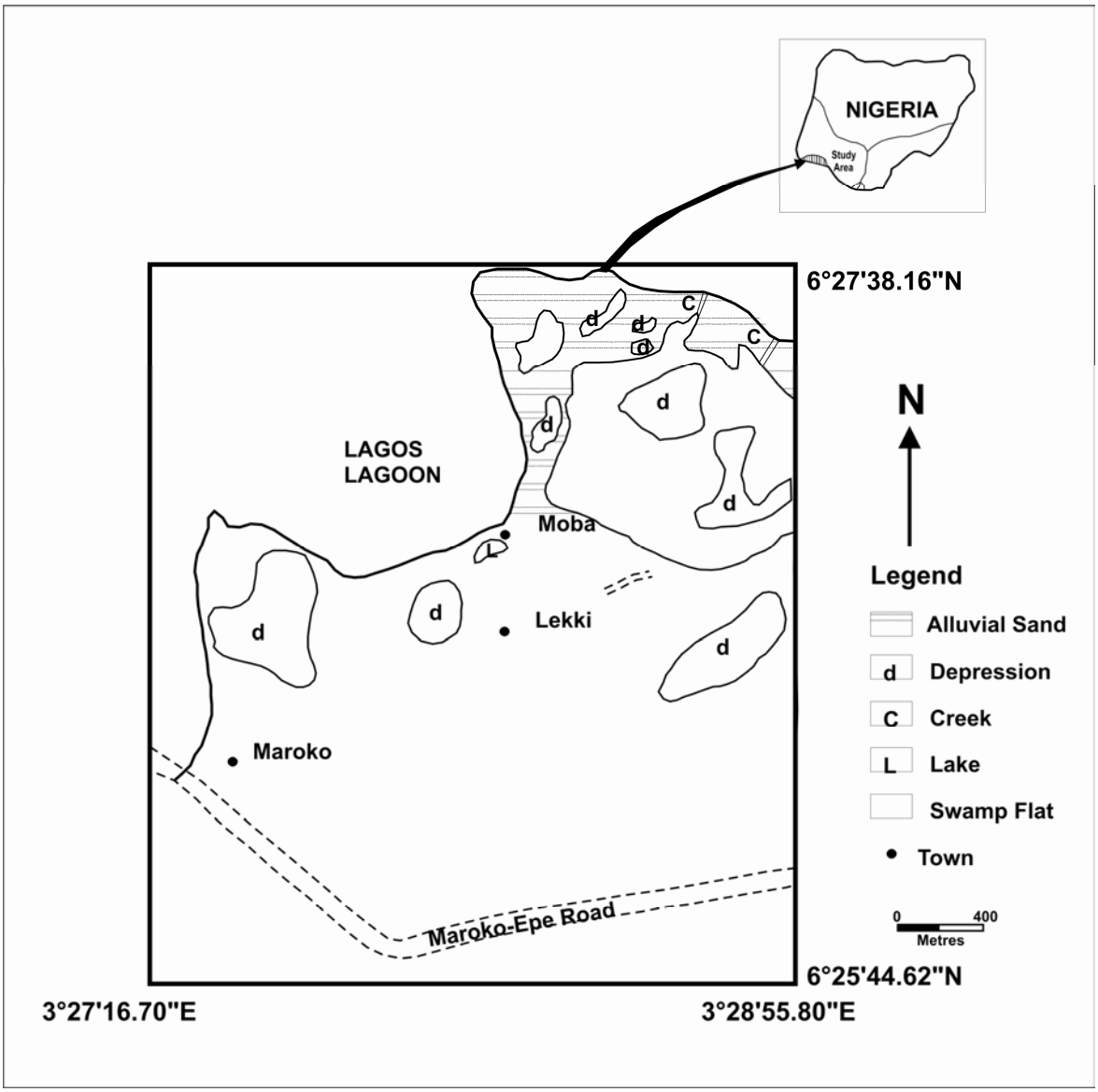


**Figure 1.** Location map of Lekki-Peninsula, Lagos, Southwestern Nigeria.

 

Cone penetrometer tests were first carried out in the study area in order to determine the hydraulic sand-fill thicknesses. For the computation of the unknown thicknesses using the finite element program, the survey area was broken into 191 triangular meshes with 147 test points. The input data are the, number of nodes, the number of elements and the nodal coordinates for each node.

## 3. METHODOLOGY

### 3.1. Cone Penetrometer

Cone penetrometer test is one of the most widely used direct methods in soil testing. The application of the method in geotechnical practice has been reviewed by Sanglerat [12] and de Ruiter [13]. It was designed as a control for the indirect geophysical method [14] and to determine the properties of the insitu soil like its sequence or profile. The penetrometer test was carried at one hundred stations with stations coinciding with the nodes of the finite element triangular meshes.

The force required to drive the probe into the ground (that is, penetration resistance) and the depth of penetration were recorded at each station. The penetration

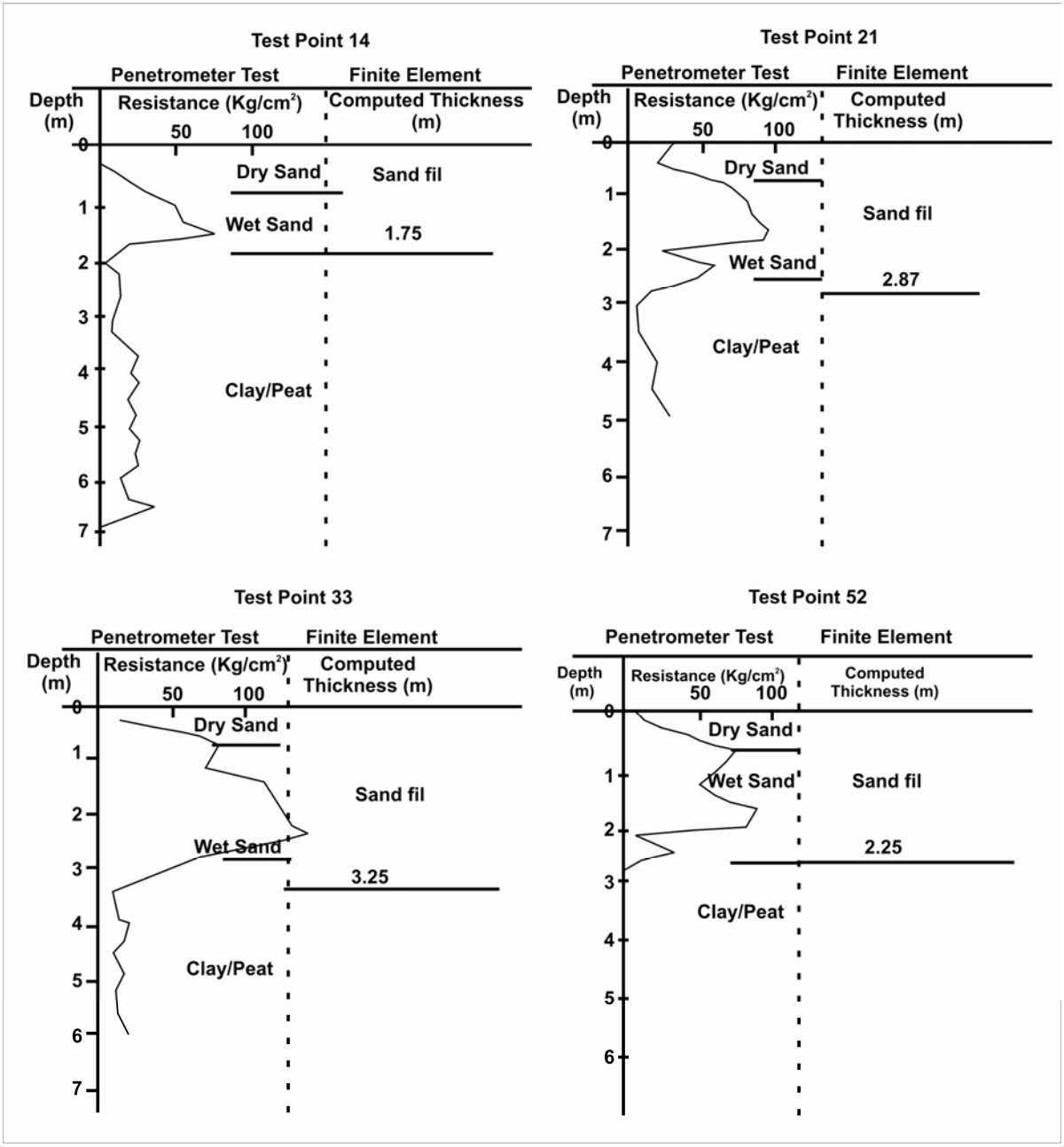


 

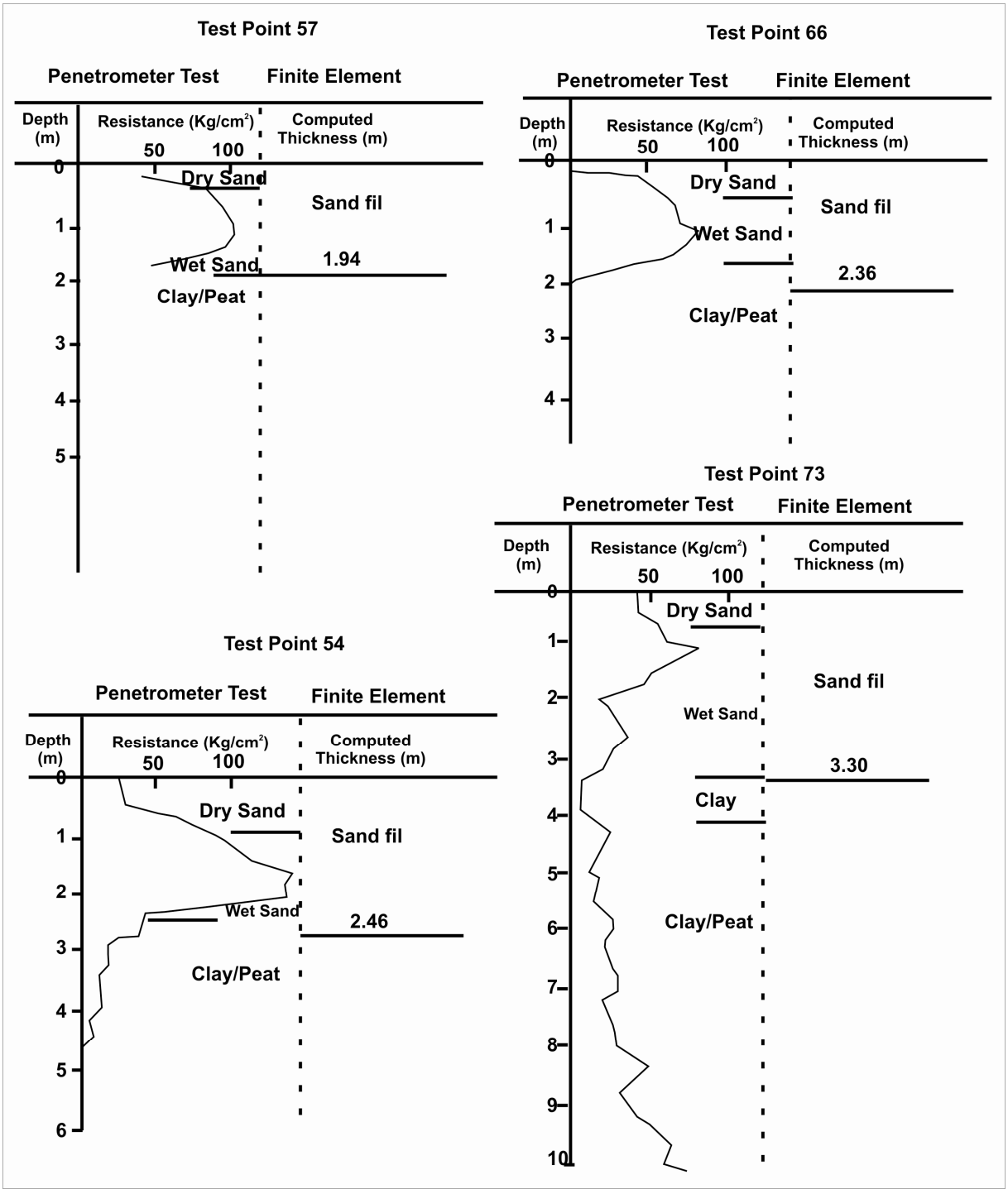


**Figures 2a & b.** Comparison of the penetrometer curves with the finite element results.

resistance in Kg/cm$^2$ was plotted against depth of penetration. In view of the envisaged resistance contrast between the sand-fill and peat/clay or sandy clay bedrock, this method was chosen for the study. The inflection points of the penetrometer curves were interpreted as the interface between the different lithologies.

## 3.2. Finite Element Method

The program presented here is based on the application of variational or weighted residual principle. The problem domain is visualized as a triangular element with four nodes at the corners. The nodes are the points within the problem domain at which thicknesses are computed

 

Fenner [5]. The residual at each point in the problem domain is a measure of the degree to which the thickness does not satisfy the governing equation. A trial solution t(x,y) is built up as a continuation of the basis function

**Table 1.** Comparison of the penetrometer tests ad finite element results.

| **NODE NUMBER** | PENETROMETER THICKNESS (m) | FINITE ELEMENT THICKNESS (m) | **NODE NUMBER** | PENETROMETER THICKNESS (m) | FINITE ELEMENT THICKNESS (m) | **NODE NUMBER** | PENETROMETER THICK-NESS (m) | FINITE ELEMENT THICKNESS (m) |
|---|---|---|---|---|---|---|---|---|
| 1 | 1.25 | - | 51 | 2.75 | - | 101 | 2 | 2.07 |
| 2 | - | 1.5 | 52 | 2.25 | 2.25 | 102 | 2.5 | 2.32 |
| 3 | 1.5 | - | 53 | 2.25 | - | 103 | 2 | |
| 4 | 1.75 | - | 54 | 2.25 | 2.46 | 104 | 2 | 1.8 |
| 5 | 1.75 | - | 55 | 2.25 | - | 105 | - | 1.51 |
| 6 | 1.5 | - | 56 | 6.75 | - | 106 | | 1.4 |
| 7 | - | 1.75 | 57 | 1.94 | 1.94 | 107 | | 1.37 |
| 8 | 1.5 | - | 58 | 1 | - | 108 | 2.25 | 2.1 |
| 9 | - | - | 59 | 2.5 | - | 109 | 2.5 | 2.06 |
| 10 | - | - | 60 | - | 1.5 | 110 | 2 | 1.76 |
| 11 | 2 | - | 61 | - | 1.4 | 111 | - | 1.49 |
| 12 | 1.75 | - | 62 | - | 4.36 | 112 | 2 | - |
| 13 | 1.6 | - | 63 | 2 | - | 113 | - | 1.37 |
| 14 | 1.75 | 1.75 | 64 | 5.6 | - | 114 | - | 1.33 |
| 15 | 3.25 | 3.25 | 65 | 2 | 3.43 | 115 | 2.25 | 2.16 |
| 16 | 2 | 2 | 66 | 1.7 | 2.36 | 116 | 2.25 | 2.14 |
| 17 | 1.7 | - | 67 | 2.14 | - | 117 | 3 | 1.74 |
| 18 | 3.4 | - | 68 | 1.5 | 1.63 | 118 | 2.5 | 1.47 |
| 19 | - | 3.9 | 69 | - | 1.56 | 119 | - | 1.34 |
| 20 | - | 3.39 | 70 | 3 | - | 120 | - | 1.3 |
| 21 | 2.5 | 2.87 | 71 | - | 2.71 | 121 | 2 | 2.24 |
| 22 | 2 | 2.88 | 72 | 2 | 2.82 | 122 | 2.75 | - |
| 23 | 2.5 | 3.2 | 73 | 3.2 | 3.3 | 123 | 2.75 | 1.81 |
| 24 | 2.25 | 2.86 | 74 | 1.2 | 2.26 | 124 | - | 1.47 |
| 25 | - | 4.42 | 75 | 2 | 1.89 | 125 | 2.2 | - |
| 26 | - | 4.36 | 76 | 1.5 | - | 126 | - | 1.31 |
| 27 | 2.5 | 3.17 | 77 | 2 | - | 127 | - | 1.25 |
| 28 | 2.2 | - | 78 | 2.2 | 2.61 | 128 | 3.5 | 2.01 |
| 29 | 2.5 | 3.78 | 79 | 2 | 2.44 | 129 | 3.5 | 1.79 |
| 30 | 2 | 3.03 | 80 | 1.75 | 2.26 | 130 | 2.5 | 1.46 |
| 31 | - | 4.49 | 81 | 1.5 | 1.86 | 131 | - | 1.46 |
| 32 | 6 | - | 82 | - | 1.63 | 132 | - | 1.27 |
| 33 | 3.25 | 3.54 | 83 | 2.2 | - | 133 | - | 1.19 |
| 34 | 3.5 | 3.77 | 84 | - | 1.49 | 134 | 3 | 1.88 |
| 35 | 3.75 | 4.59 | 85 | 2 | 1.45 | 135 | 2.25 | - |
| 36 | 2.2 | 3.05 | 86 | 2.2 | - | 136 | 2.5 | 1.98 |
| 37 | 2 | - | 87 | 3.25 | 2.33 | 137 | 1.25 | - |
| 38 | - | 2.91 | 88 | 1.75 | - | 138 | - | 1.48 |
| 39 | 3 | - | 89 | 1.5 | 1.72 | 139 | - | 1.23 |
| 40 | 3.5 | 3.77 | 90 | - | 1.55 | 140 | - | 1.12 |
| 41 | 3 | - | 91 | - | 1.45 | 141 | 1.6 | - |
| 42 | 2 | 2.8 | 92 | - | 1.42 | 142 | 1.5 | - |
| 43 | 2 | 3.04 | 93 | 1.5 | 2.29 | 143 | 2.5 | - |
| 44 | - | 2 | 94 | 2.25 | - | 144 | 2.5 | - |
| 45 | - | 2 | 95 | 2 | 2.17 | 145 | 1.5 | - |
| 46 | 2 | 2.5 | 96 | 2.25 | 1.75 | 146 | 1.2 | - |
| 47 | - | 2 | 97 | - | 1.53 | 147 | 1 | - |
| 48 | 1.75 | - | 98 | 2.25 | - | | | |
| 49 | 3.2 | - | 99 | - | 1.43 | | | |
| 50 | 2 | - | 100 | - | 1.39 | | | |

expressed as a series summation.

$$t(x,y) = \sum_{L=1}^{NNODE} tLN_L(x,y) \quad (1)$$

L = The nodal number

$t$ = An approximate or trial solution

For the computation of the unknown thicknesses by the program, the triangular mesh was digitized at equal intervals of 500m. The accuracy of the predicted thicknesses is strongly dependent on the accuracy of the initial guess or starting thicknesses and the size of the nodal spacing. The thicknesses were predicted for stations (nodes) at which penetrometer tests have been carried out and at which no penetrometer tests were carried so as to cover the entire survey site.

## 4. RESULTS AND DISCUSSION

The typical cone penetration curves obtained in the study area are shown in **Fig. 2**. As can be seen from the figures, the curves generally show relatively low resistance (0-60 Kg/cm$^2$) within the uppermost layer of loose/ uncompacted dry sand. This increases to some 60–150 Kg/cm$^2$ in the wet compacted sand, dropping sharply to between 5 and 45 Kg/cm$^2$ in the underlying clay peat and sandy clay horizons. The penetrometer tests delineated three to four lithologic units. The topsoil of dry and loose sand, wet sand, sand clay/clay or peat bedrock. It was observed in general that, the first two layers constitute the sand-fill (**Fig. 2**) whose thicknesses vary from 1.25 to 6.00 m (**Table 1**).

The finite element predicted thicknesses are presented in **Table 1**. The results were compared with the penetrometer obtained sand-fill thicknesses. It is observed that the finite element derived thicknesses are in good agreement with the penetrometer test thicknesses with a few exceptions at stations 29, 30, 35, 65, 74 and 93, where very high percentage deviation of between 51 to 88% were obtained; these fairly large deviation may be due to insufficient input data to act as control around these stations.

The good correlation between the finite element predicted thicknesses and that obtained from the penetrometer test results imply that, given a limited accurate thicknesses as input data, the finite element program would predict the thicknesses at unknown stations to within a reasonable level of accuracy. The close agreement also indicates that the finite element predicted thicknesses could be reliably used for formation thickness estimation in the absence of sufficient penetrometer test results.

**Fig. 3** is an isopach map prepared from finite element predicted thicknesses. The map shows sand thick-

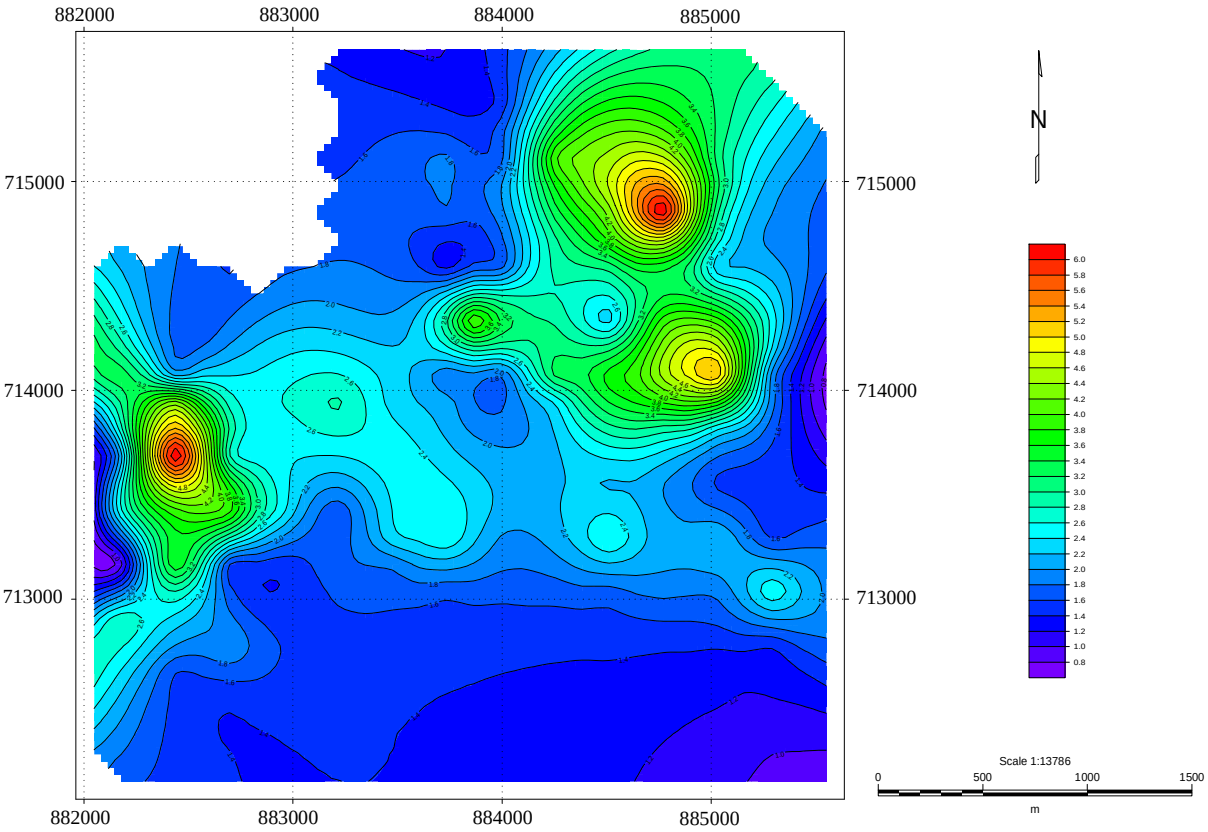


**Figure 3.** Isopach map of the sand-fill using the computed finite element result.

 

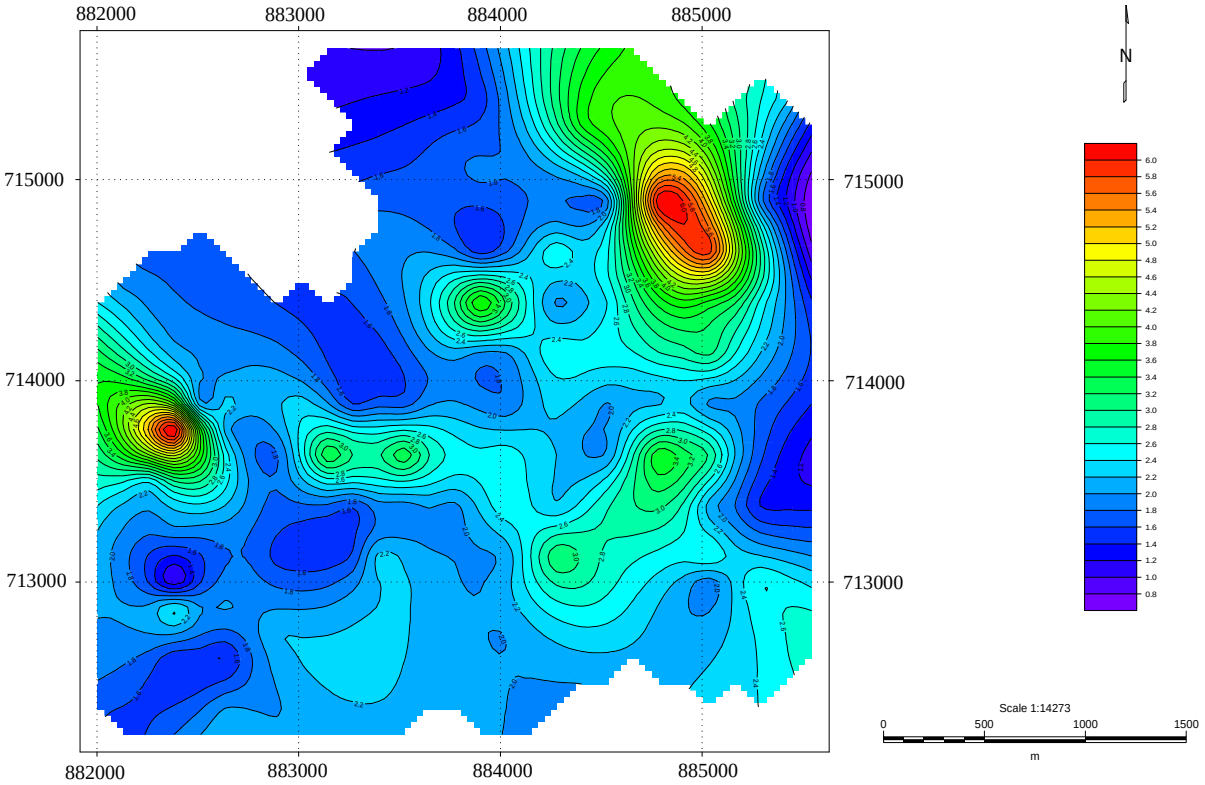


**Figure 4.** Isopach map of the sand-fill using the penetrometer obtained thicknesses.

nesses varying from 1.25 to 6.0 m in the area labeled t1, t2, t3, t4, t5 and t6. This zone corresponds to basement depression associated with river/stream channels and creeks in the area which are the main shallow structural features in the surveyed are pre-sand fill. The structural trend of the depressions is largely influenced by the oceanic fracture pattern (NW-SE, NNE-SSW, N-S, and E-W) earlier delineated by Emery *et al.* [15]. This map compares well with the isopach map prepared from penetrometer obtained thicknesses (**Fig. 4**) with thick sand zone correlating.

## 5. CONCLUSIONS

The qualitative and quantitative interpretation of the penetrometer test results provided adequate information regarding the structural disposition of the geomorphic shallow structures existing pre-sand-fill. From the penetrometer test, the first two layers constitute the sand-fill with thicknesses varying from 1.25 to 6.00 m. Good correlations exist between the finite element, and the penetrometer thicknesses with few exceptions. The isopach maps show area of basement depression corresponding to ancient river/stream channels and creeks with structural disposition trending in the NE-SW, NW-SE, NNE-SSW, N-S and E-W. The result shows that, finite element method is an efficient means of predicting formation thicknesses that can help considerably in reducing engineering geophysics survey costs.

## REFERENCES

[1] Adepelumi, A. A. and Olorunfemi, M. O. (2000) Engineering geological and geophysical investigation investigation of the reclaimed Lekki Peninsula, Lagos, Southwest Nigeria. Bulletin of Engineering, Geology and the Environment, **58**, 125−132.

[2] Kearey, P. and Brooks, M. (1984) An introduction to geophysical exploration. Blackwell Scientific Publication, Oxford, 198−217.

[3] Olorunfemi, M. O. and Mesida, A. (1987) Engineering geophysics and its application in engineering site investigations (Case study from Ile-Ife area). The Nigerian Engineering, **22(2)**, 57−66.

[4] Olorunfemi, M. O. and Okhue, E. T. (1992) Hydrogeologic and geologic significance of a geoelectric survey at Ile-Ife, Nigeria. Journal of Mining and Geology, **28(2)**, 221−229.

[5] Fenner, R. (1975) Finite element method for engineers. Macmillan Press Ltd. London, 171−171.

[6] Agbede, A. A. (1981) The finite element analysis of the opa river dam. Unpublished M. Sc. Thesis, Obafemi Awolowo University, Ile-Ife, 32−32.

[7] Wang, H. F. and Anderson, M. P. (1982) Groundwater modelling with finite difference and finite element methods. Elsevier Publishing, Amsterdam, 1−137.

 

[8] Buchanan K. M. and Pugh J. C. (1955) Land and people in Nigeria: The human geography of Nigeria and its environmental background. London, University of London Press.

[9] Webb J. E. and Hill M. B. (1958) Ecology of Lagos lagoons (II): The topography and physical features of Lagos harbor & Lagos lagoons. Philosophical Transaction of Royal Society, London, **B24**, 319−333.

[10] Durotoye, A. B. (1975) Quaternary sediments in Nigeria. Geology of Nigeria, Elizabeth Press, Lagos, 431−451.

[11] Bureau de Recherches Geologiques et Minieres (1979) Pre-drilling hydrogeological report area 18 and 19 submitted to the Federal Department of Water Resources, Lagos, Nigera, 1−60.

[12] Sanglerat, G. (1972) The penetration and soil exploration. Development in geotechnical engineering, Elsevier Scientific Publishing, New York, 52−80.

[13] De Rutter, J. (1981) Current penetrometer practice. American Society of Civil Engineers Convention, St. Louis, State of the Art report, Session **35**, 64−64.

[14] Scott, C. R. (1969) An introduction to soil mechanics and foundations. Applied Science Publishers Ltd, London, 379−399.

[15] Emery, K. O. E., Uchupi, J. P., Bowin, C. and Mascle, J. (1975) Continental margin off western Africa-Angola to Sierra Leone. American Association of Petroleum Geologist Bulletin, **59**, 2209−2265.

 

**Natural Science, 2009, 1, 10-16** **NS**

# Studies on the effects of pretreatment on production hydrogen from municipal sludge anaerobic fermentation

**Feng Wu[1,2], Shao-Qi Zhou[1,*], Yang-Lan Lai[1], Wen-Jiao Zhong[2]**

[1]College of Environmental Science and Engineering, South China University of Technology, Guangzhou, 510006, China; [2]Guangdong Provincial People's Armed School, Guangzhou, 510006, China.
Corresponding author: [*]fesqzhou@scut.edu.cn

Received 31 March 2009; revised 15 April 2009; accepted 21 April 2009.

## ABSTRACT

**Municipal sludge was rich in organic matter, period of natural degradation was long and low efficiency, leachate would pollute underground water. In this paper, a comparative study of the ways of pretreatment with acid alkali treatment, heat digestion and ultrasonic treatment were done. The results showed that the dehydrogenase activity was increased, the SCOD (soluable chemical oxygen demand, SCOD) increased more than 2.47~2.83, 1.70~1.76, 2.6~2.77 times respectively. The hydrogen yield increased more than 11.5~12.2, 24.1~24.7, 34.2~34.9 mL.g$^{-1}$ (VS) respectively. The period of pro-hydrogen was shorten to 7.5, 8.0, 6.5 d respectively. The degradation rate was up to 72.04%, 81.4%, 80% respectively, the methane concentration in the gas was close to "zero" and ultrasonic treatment was better than others. Gompertz model curve fitting on hydrogen production was carried out. All the values of correlation factor R2 were more than 0.97.**

**Keywords:** Municipal Sludge; Pretreatment; Anaerobic Digestion; Biological Pro-Hydrogen

## 1. INTRODUCTION

The wastesolid treatment mainly includes filleading, compost and incineration. Filleading and heap in brief results in resource waste and pollute the body of water, even endanger the human health. Which don't attach to coincidence method of "circulation economy". The wastesolid anaerobic fermentation producted hydrogen develope a new road of wastesolid resource. And many research workers are interested in it [1,2,3,4,5,6,7]. Gomez [8] has study on the two stages of bio-hydrogen production, hydrogen production and methanogenic, using organic solid waste and slaughterhouse waste as substrate, high temperature activated sludge as inoculum. Levin's study [9] showed the wooden fiber of delignification is a good hydrogen production substrate. Liliana [6] use anaerobic sludge to degraded organic solid waste and synthetic wastewater in UASB whose capacity is 3.85 L, and produce hydrogen successfully. The volume content and hydrogen production rate of $H_2$ is 47%, 99 N mL.g$^{-1}$(VS); 51%, 127 N mL.g$^{-1}$(VS) respectively. Zuo Yi [10] used river sediments as seed sludge, at the optimal condition of the pH of 5.0-5.2, temperature of 35℃, and HRT of 6-8 h, a steady anaerobic bio-hydrogen production was obtained in a lab scale reactor successfully with gluose as substrate. The highest hydrogen production was 6.7 L.d$^{-1}$. Tai Mulin [11] showed that the optimal initial pH for bio-hydrogen production from sewage sludge was around 11.0, Under this optimal condition, the bio-hydrogen yield of raw sludge was 8.1 mL.g$^{-1}$, and it would reach to 16.9 mL.g$^{-1}$ when the sludge was pretreated by alkali. Steven W. Van Ginkel [12] used food wastewater as substrate indicated Biogas produced from all four food processing wastewaters consistently contained 60% hydrogen, with the balance as carbon dioxide. Heguang Zhua [13] showed enhanced hydrogen production potential as compared with All combinations of the feedstocks (FW+PS, FW+WAS and FW+PS+WAS). A mixing ratio of 1:1 was found to be the best among the ratios tested and hydrogen yield of 112 mL.g$^{-1}$ volatile solid (VS). M. Krupp and R. Widmann [14] studied Biohydrogen production by dark fermentation, the result showed The gas amount varied with the different OLRs, but could be stabilised on a high level as well as the hydrogen concentration in the gas with 44~52%. Ela Eroglua [15] introduced Biological hydrogen production from olive millwastewater with two-stage processes. In some cases of dark-fermentation, activated sludge was initially acclimatized to the OMW to provide the adaptation of microorganisms to the extreme conditions of OMW. The highest hydrogen production potential obtained was 29 L $H_2$/LOMW. Dongmin Li [16] used corn straw as substrate, Hydrogen was produced by simultaneous saccharification and fermentation from steam-exploded corn straw (SECS) using *Clostridium butyricum* AS1.209.

Maximum specific hydrogen production rate and maximal hydrogen yield were 126 $mL.g^{-1}$ (VSS) d and 68 $mL.g^{-1}$ SECS, respectively. The yield of soluble metabolites was 197.7 $mg.g^{-1}$ SECS. Acetic acid accounted for 46% of the total was the most abundant product and this shows that hydrogen production from SECS was essentially acetate-type fermentation.

Consequently, fermentative bio-hydrogen production technique is at the stage of laboratory research, many hydrogen production bottlenecks binding factors are urgently needed to be solved. This study focused on the factors of fermentative bio-hydrogen production of municipal sludge. In this paper, a comparative study on the effect of pretreatment-acid alkali treatment, heat digestion and ultrasonic treatment on hydrogen production were done, and the optimum pretreatment approach was ascertained, which break new a way for sludge treatment.

## 2. MATERIALS AND METHODS

### 2.1. Source and Characteristic of Sludge

Concentrated sludge came from a sewage treatment plant in Guangzhou, China. **Table 1** showed The characteristics of the municipal sludge. In the experiment, the proper complement of N, P and inorganic micronutrients should be added in the sludge. The nutrient solution contained: $NH_4HCO_3$ 2.0 $g{\cdot}L^{-1}$, $MgSO_4{\cdot}7H_2O$ 50 $mg{\cdot}L^{-1}$, NaCl 10 $mg{\cdot}L^{-1}$, $Na_2MoO_4{\cdot}2H_2O$ 10 $mg{\cdot}L^{-1}$, $CaCl_2{\cdot}2H_2O$ 10 $mg{\cdot}L^{-1}$, $MnSO_4{\cdot}7H_2O$ 15$mg{\cdot}L^{-1}$, $FeCl_2$ 70 $mg{\cdot}L^{-1}$, $KH_2PO_4$ 10 $mg{\cdot}L^{-1}$.

### 2.2. Experimental Equipment

Cylindrical anaerobic reactor (patent number: ZL 20052 0053384.X) with the dimensions: $ø_{diameter}$ = 22 cm, $ø_{external\ diameter}$ = 24 cm, h = 30 cm, effective volume = 11 liters; JY99-IID ultrasonic cell disruptor (Ningbo Xinzhi); XLJ-IIB low-speed tabletop centrifuge (Shanghai an ting Scientific Instruments and Apparatus Co.); SC-15 thermostatic water-circulator bath box (Ningbo Xinzhi); JJ-4 digital display motor stirrer (Jintan City Zhengji Instruments Co. Ltd); BSD0.5 wet-gas flow meter (Shanghai Blue Jewelry); GC-7900 gas chromatograph, thermal conductivity detector, and FID detector (Shanghai Tianmei); ZXZ-1 sliding vane rotary vacuum pump (Zhejiang Huangyanqiujing, modified as shown in **Fig. 1**).

### 2.3. Experimental Methods

1kg dried sludge was dissolved in 10 L water，stirred uniformly, divided into A, B, C group. This sample would carry out acid alkali treatment, heat digestion and ultrasonic treatment, using 2#, 3#, 4# to mark the sample performed cid alkali treatment, 5#, 6#, 7# to mark the sample performed heat digestion and 8#, 9#, 10# to mark the sample performed ultrasonic treatment. Put 200 mL the liquor in a cone type bottle as reference object which was marked 1#. They were respectively performed anaerobic digestion in shaking table whose rate was 1,050 rpm at 36℃.

### 2.4. Analysis Methods

Gas components were detected using a gas chromatograph (model: GC-7,900). A flame ionization detector (FID) and a 2-m stainless steel column packed with 5A

**Table 1.** Characteristics of condensed sludge from municipal wastewater treatment plan.

| pH | SS (g/Kg) | Water content (%) | TN | COD |
|---|---|---|---|---|
| 6.7~7.9 | 13~27 | 78.7~90 | 1750~2000 | 3900~5000 |

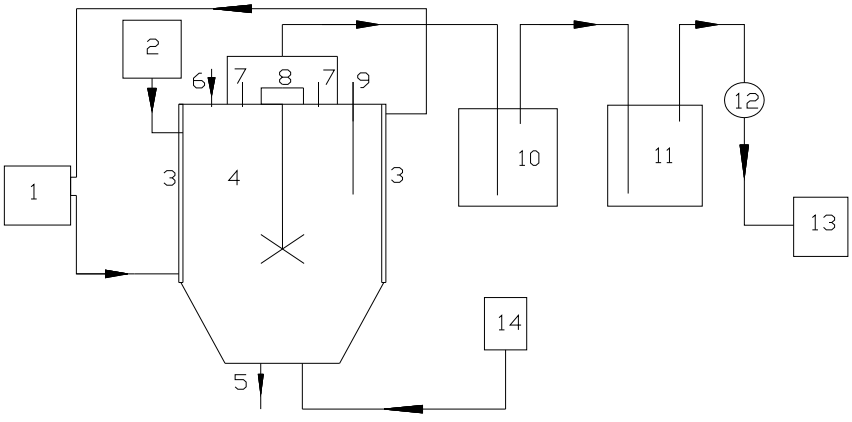


1. SC-15 water bath; 2. pH adjusting port; 3. organic reactor; 4. agitating blade; 5. reaction substrate outlet; 6. material inlet; 7. vent; 8. digital stirrer; 9. thermometer; 10. CO2 removal; 11. desiccant; 12. wet gas flowmeter; 13. GC-7900 gas chromatography; 14. nitrogen purging port.

**Figure 1.** Equipment and sequence of steps in the anaerobic digestion of sludge.

 

Molecular Sieve were used to analyze the methane concentration. The temperatures of the injector, detector, and packed column were, respectively, 150, 180, and 100°C. $H_2$ was used as the carrier gas at a flow rate of 30 mL·min$^{-1}$. The $N_2$ flow rate was 30 mL·min$^{-1}$ and the air velocity 260 mL·min$^{-1}$. The hydrogen concentration was analyzed using a thermal conductivity detector (TCD) and a 2-m stainless steel column packed with 5A Molecular Sieve. The temperatures of the injector, detector, and packed column were, respectively, 180, 200, and 100°C. $N_2$ was used as the carrier gas at a flow rate of 29 mL·min$^{-1}$. The injection volume was 10 μL. Quantitative analysis was carried out using external standards.

Otherwise, The quantity of chemical oxygen demand in sludge supernatant fluid was used to estimate the performance of sludge disintegration. The value of TCOD was equal to that of waste activated sludge supernatant fluid. The value of SCOD was equal to that of COD of sludge supernatant fluid which has been treated by centrifugal separation and filtration [17]. Determination of COD followed the standard methods [18]. The centrifuge worked for 20 min at 1,050 rpm, COD was determined according to International Standard [3]. Dehydrogenase activity of sludge was determined according to the method reported in the literature [19,20].

### 2.5. Cumulative Hydrogen Yield

Cumulative hydrogen yield was estimated using the following equation [21,22]:

$$V=V_0\gamma_i+\sum V_i\gamma_i \quad (1)$$

where V is the cumulative hydrogen yield (mL), $V_0$ the volume above the liquid level in the reactor (mL), $V_i$ the volume of gas extracted in phase i (i=1,2,3...) (mL), and $\gamma_i$ the concentration of hydrogen in the gas extracted in phase i (i = 1, 2, 3...) (i = 1, 2, 3...)(%).

### 2.6. Kinetic Model of Hydrogen Production

The Gompertz equation was used in the regression analysis of the anaerobic hydrogen production data in order to determine the lag time of hydrogen production, the hydrogen production potential, and the hydrogen production rate [22,23]:

$$H = P_s \exp\left\{-\exp\left[\frac{R_s e}{P_s}(\lambda - t)+1\right]\right\} \quad (2)$$

where H is the cumulative hydrogen yield (mL), $P_s$ the maximum hydrogen yield (mL), $R_s$ the maximum hydrogen yield rate (mL.h$^{-1}$), and λ the lag time of hydrogen production (h).

## 3. RESULTS AND DISCUSSIONS

### 3.1. Effect of Acid and Alkali Treatment on Hydrogen Production

Under normal temperature, the SCOD value of different sludge changed. 2#, 3#, 4# were used to mark the sludge pH = 10, 11, 12, respectively. 1# is control group, it is neutral. **Fig. 2** showed the changes of SCOD value of sludge treated by acid alkali treatment. **Fig. 3** showed the state of sludge anaerobic digestion bio-hydrogen production. **Fig. 2** showed that the SCOD value of 2#, 3#, 4# changed with time in the same regular but in different level: 9,266, 9,477, 10,624.5 mg.L$^{-1}$. Compared with 1#, The SCOD value of 2#, 3#, 4# were separately increased 2.47, 2.53, 2.83 times, The data indicated the dissolution of organic increased because of acid alkali treatment. The value of SCOD reached maximum at 24th hour, beginning to decrease at about 24-28th hour. The degradation rate was up to 72.04% from 60.4%, increased by 12%. The reason was that after the sludge was treated by acid alkali treatment, most of the organic has been dissolved, some of the difficult dissolved or-

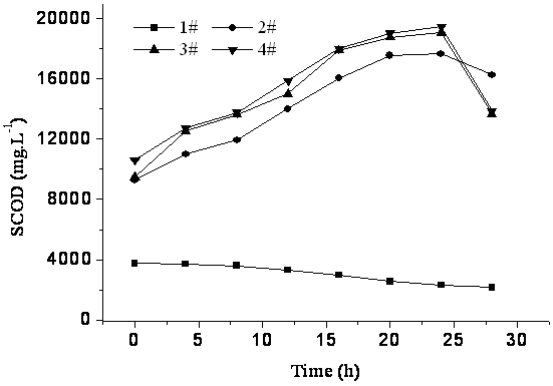


**Figure 2.** Change of SCOD about Sludge for anaerobic digestion.

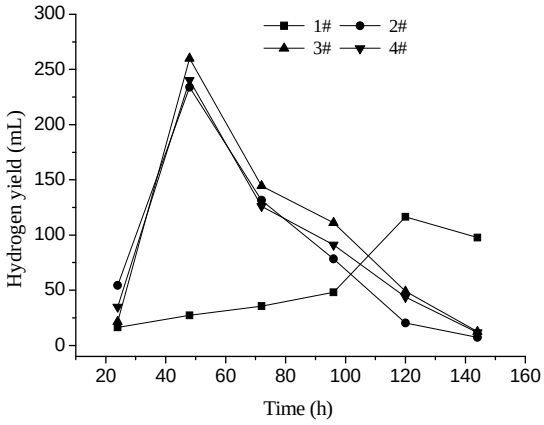


**Figure 3.** Change of hydrogen production about Sludge for anaerobic digestion ed and modified , and then solidified.

ganic lignose, cellulose and hemicellulose etc had structural changes, hydrolyzed by cellulase, ligninase, etc. 24h after start-up, almost all the organic absorbed by sludge has dissolved. The rate of organic dissolution was faster than that of bio-degradation result in the accumulation of organic in liquor, therefore, SCOD value rose obviously. 28~32 h after start-up, the number of biomass and live bacteria is max in the system. Plenty of carbon source was needed to maintain biological metabolism, so the anaerobic digestion speeded up, the organic was consumed by anaerobic bacteria as nutrient, and the COD started to decline. At the moment a large number of small bubbles attached to the conical flask because of biohydrogen bacterium starting to produce enormous hydrogen. In order to facilitate gas emissions, turn down the rate of shaking table to 1,050 rpm to reduce gas-liquid interface pressure. The peak hydrogen productionin was observed at 32−48th hour, then the sludge hydrogen production ability weakened gradually, and the hydrogen content began to decline. 7.5 d after start-up, litter hydrogen was produced. The hydrogen production yield of 2#, 3#, 4# were 11.5, 12.2, 11.7 $mL.g^{-1}$ (VS) respectively. A little gas was produced at the first day in 1#, and the hydrogen content was low, Less than 30%. The amount of hydrogen started to increase linearly in the second day and reach its peak at the sixth day, but the maximum rate of hydrogen production lasted no more than 2 h. Until the 13th day the gas was too little to collected, therefore the hydrogen production period is 13d. hydrogen production yield is 9.2 $mL.g^{-1}$ (VS). Consequently, after the sludge was treated by acid alkali treatment, the period of hydrogen production was shortened obviously, acid alkali treatment is an effective solution to the problem that the hydrogen production period is too long in sludge anaerobic digestion system. After acid pretreatment, the amount of dissolved organic in sludge increased, which is the same as the effect of alkali pretreatment. The difference between acid pretreatment and alkali pretreatment was that acid pretreatment provided methanogen a good growth condition because of the acidification of substrate and the formation of menthanogenic phase, in order to maintain the systems ability of hydrogen production, it is needed to control the pH value or to use methanogen inhibitor such as acetylene, BES to make the system pro-hydrogen instead of methane.

## 3.2. Effect of Heat Digestion Pretreatment on Bio-Hydrogen Production

**Fig. 4** showed the amount of SCOD in 5#, 6#, 7# rose linearly with the heat digestion time extended and the temperature rose. When the sludge temperature is 80~100℃, the amount of dissolved organic increased obviously. The dissolution rate reached the peak at 93℃, however the rate decreased when the temperature rose

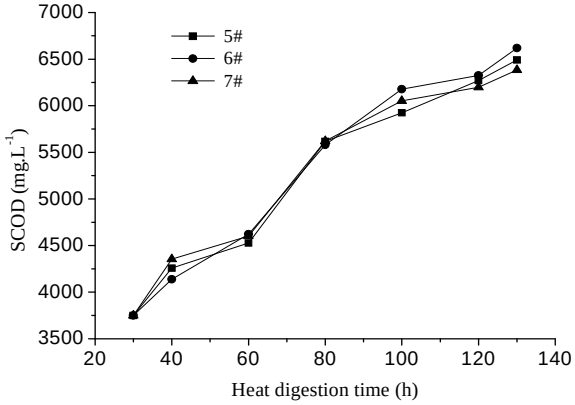


**Figure 4.** Change of SCOD about Sludge for heat digestion.

to 120℃. There was refractory fiber as well as easily degradable organic in the sludge. **Fig. 5** showed the structure of the fiber. When the temperature was higher than 120℃, the fiber structure was destroyed, decomposing into cellobiose and penta-disaccharide, and then transforming into glucose, degraded by bacteria finally. Therefore, the SCOD value increased slowly. The amount of SCOD in 5#, 6#, 7# were separately increased 1.73, 1.76, 1.70 times. The changes of fermentative bio-hydrogen production were depicted in **Fig. 6** hydrogen production of 5#, 6#, 7# increased considerablely 27 h after start-up, and reached the peak in 40~48h, then declined. Little gas could be collected at the 8th day, which was considered as the end of cycle period. The hydrogen production yield of 5#, 6#, 7# is 24.7, 24.1, 24.1 $mL.g^{-1}$ (VS). Heat digestion dissolved the de-lipid of cell, weakened the tolerance ability of cell wall against heat, promoting the hydrolysis of sludge. It was observed that the color of sludge mixed liquor turned into reddish-brown, and the liquor was covered by a layer of film because of the effect of heat. the reason maybe a part of microbiology protein dissolve.

## 3.3. Effects of Ultrasound Treatment on Anaerobic Sludge Digestion Hydrogen Production

**Fig. 7** illustrated changes of anaerobic sludge digestion hydrogen production. On the conditions of P = 1,800 W and f = 35 kHz, the sludge samples 8#, 9#, 10# are treated with ultrasound for 20 min respectively. An increase of dissolved chemical oxygen demand of sludge was observed. The rate of organic matter dissolution can be calculated by Equation (2).

$$DDCOD = \frac{SCOD_t - SCOD_{t0} - SCOD_{pH}}{TCOD - SCOD_0} \times 100\% \qquad (3)$$

In the equation:

DDCOD——rate of organic matter dissolution, %;

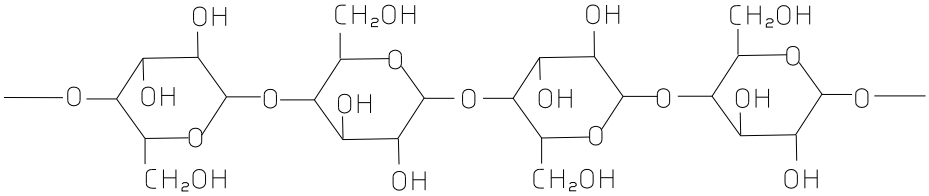


**Figure 5.** The schematic diagram about the structure of the cellulose.

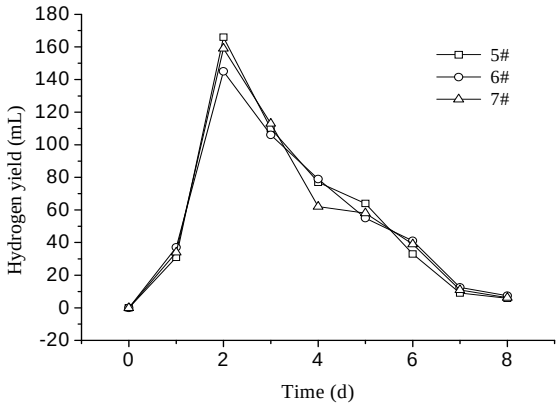


**Figure 6.** production hydrogen of anaerobic digestion from sludge by heat digestion.

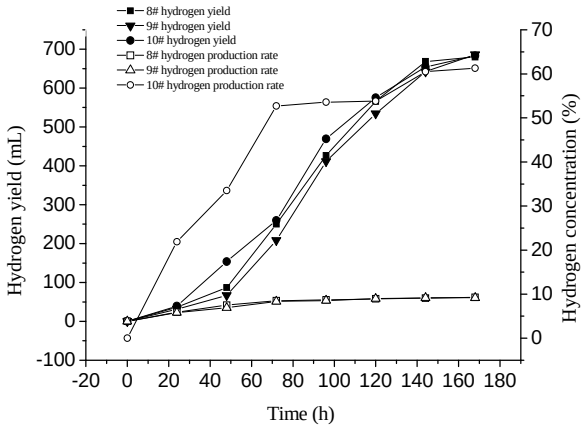


**Figure 7.** production hydrogen of anaerobic digestion from sludge by ultrasonic wave.

TCOD——the COD of supernatant obtained from the sludge solution, mg/L;

$SCOD_{pH}$——the COD of filtering supernatant of sludge solution under pH, $mg \cdot L^{-1}$;

$SCOD_{t0}$——the COD of supernatant obtained from the sludge solution been centrifuged, $mg \cdot L^{-1}$;

$SCOD_t$——the COD of filtering supernatant of sludge solution under different radiation time, $mg \cdot L^{-1}$.

The SCOD value was 2.70, 2.77, 2.64 times than that of 1# respectively, organic solution rate was 48~65%. Adaptation time of hydrogen-producing bacteria is 17.4 h, and logarithmic phase time is 9 h. The growth and reproduction of microorganisms went into stationary phase after 26 h, which has the largest biomass and the most hydrogen production. Simultaneously, hydrogen production of 8#, 9#, 10# went into the peak phase, and the production of 10# reached 210 $mL.d^{-1}$, then the production began to decline. 7 days after start-up, hydrogen production was less than 10 $mL.d^{-1}$ reaching almost zero at the end of the cycle period. Degradation rate of COD is more than 80%, and the hydrogen production yield is 34.2, 34.9, 34.5 $mL.g^{-1}$ (VS) respectively, and the methane concentration close to "zero". The analysis showed that sludge solution was affected by ultrasonic energy experience dynamic processes of vibration, growth, collapse and closure. At the moment of the collapse of the bubble, high-temperature and high pressure will be created in a very small space around the bubble, which will destruct the floceulent structure of sludge and crush the cell of microorganisms. Intermolecular hydrogen bond of Cellulose which is refractory broke by ultrasonic irradiation, producing organic matter easily biodegradable such as sugar. Consequently the dissolved organic, which provided enough carbon source for the growth and reproduction of anaerobic microbe, multiplied in sludge solution. It was also found that after ultrasonic irradiation, the permeability of cell membrane and cell wall have changed, and the looseness of extracellular polymers increased, which promoted biological mass-transfer and improved the enzyme activity, so the TF (The activity of dehydrogenase was evaluated by the amount of TF which generated by the reaction between per unit mixture liquid sludge and TTC in unit time, the unit is $mg \cdot L^{-1} \cdot h^{-1}$) value rose. **Fig. 7** showed the change trend of dehydrogenase activity. because of the ultrasound pretreatment, the catalysis of dehydrogenase and nitrogenase etc. was improved, as well as the decomposition and absorption ability of anaerobic bacteria and facultative anaerobe [24]. Therefore the degradation of organic speed up. In the stage of peak hydrogen production lots of bio-hydrogen heterotrophic bacteria were observed, such as clostridium, enterobacter, Escherichia coli, Citrobacter, Bacillus, Thiobacillus, etc. by microscopic examination, the most bacteria were enterobacter aerogenes, candida maltose. Synergistic effect between strain is good, which inhibited the accumulation of metabolites and then provided a good environment for hydrogenogens, therefore it was given full play to hydro-

genogens, the hydrogen production yield rose.

### 3.4. Effect of Dehydrogenase Activity by Pretreatment Sludge

Dehydrogenase activity is defined as the TF volume per unit time, with the unit $mg \cdot L^{-1} \cdot h^{-1}$ [25]. From **Fig. 8**, the initial TF was 60.6 $mg \cdot L^{-1} \cdot h^{-1}$, after pretreatment TF were 71.2, 69.9, 78.8 $mg \cdot L^{-1} \cdot h^{-1}$ respectively.12h later, TF declined to 32, 31.2, 27.7 $mg \cdot L^{-1} \cdot h^{-1}$ respectively. The result showed Dehydrogenase activity was increased with pretreatment. the permeability of cell membrane and cell wall changed because of pretreatment, which promoted the mass transfer, the production and activity of cell enzyme, so the metabolism speeded up. Moreover, NAD+ or NADP+ regenerated by cell can absorb and transport substrate or TTC effectively, therefore the amount of TF increased [26].

### 3.5. Analyzing Kinetic Model of Hydrogen Production Bacteriaons

**Fig. 3**, **Fig. 6**, and **Fig. 7** showed hydrogen production closely related to the microbial growth regularity. The change of hydrogen yield contain four phases: lag phase, beginning of hydrogen production, continuous hydrogen production and attenuation of hydrogen production. The lag phase was short (0~11 h). There was no hydrogen production until a stable hydrogen production flora formed after acclimation, cultivation and propagation. Subsequently, hydrogen yield increased gradually with the exponential increase of bacteria. Hydrogen content rose when the growth rate of bacteria was maximum. About 27 h later, the organic content of substrate declined because of the rapid bacteria propagation consuming considerable organic material. Meanwhile, the accumulation of metabolites poisoned bacteria, and bacteria death rate rose. When the growth rate balanced the death rate, the amount of bacteria in the system was maximum. After 80h nutrition was exhausted, the bacteria performed endogenous respiration and even formed spore, hydrogen yield declined until the end. The reaction period was about 160 h. No methane was observed during the reaction. Gompertz model curve fitting on hydrogen production was carried out. All the values of correlation factor R2 were more than 0.97. Therefore the fitting effect of Gompertz model on describing the bio-hydrogen production process was good.

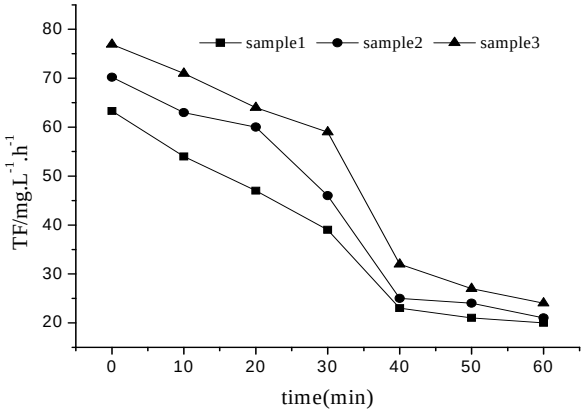


**Figure 8.** Variation of dehydrogenase activity with pretreatment.

## 4. CONCLUSIONS

The sludge been treated by acid and alkali, heat digestion, ultrasonic treatment, most of the refractory organic transformed into easily degradable carbohydrate. Compared with control group, the dehydrogenase activity was increased, the SCOD was increased 2.47~2.83, 1.70~1.76, 2.6~2.77 times respectively, the hydrogen production yield were 11.5~12.2, 24.1~24.7, 34.2~34.9 $mL.g^{-1}(VS)$ respectively, the period of hydrogen production was shorten to 7.5, 8.0, 6.5 d respectively. Remove of the COD was up to 72.04%, 81.4%, 80% respectively. the methane concentration in the gas was close to "zero". The hydrogen concentration can reach 99.3% after the bio-gas was purified by $Ca(OH)_2$ saturated solution. Gompertz model curve fitting on hydrogen production was carried out. All the values of correlation factor R2 were more than 0.97.

## ACKNOWLEDGEMENTS

The authors wish to thank the New Century Outstanding Young Teacher Grant of the Ministry of Education of China for financial support (NCET-04-0819).

## REFERENCES

[1] Liliana, M., Alzate-Gaviria, Sebastian, P. J., *et al*. (2007) Comparison of two anaerobic systems for hydrogen production from the organic fraction of municipal solid waste and synthetic wastewater [J]. Hydrogen Energy, **3(4)**, 1−6.

[2] Zabut, B., Kahlout, K. E., Yücel, M., *et al*. (2006) Hydrogen gas production by combined systems of Rhodobacter sphaeroides O. U. 001 and Halobacterium salinarum in a photobioreactor [J]. Hydrogen Energy, **31(11)**, 1553− 1562.

[3] Venkata, M. S., Lalit, B. V. and Sarma, P. N. (2007) Anaerobic biohydrogen production from dairy wastewater treatment in sequencing batch reactor (AnSBR): effect of organic loading rate [J]. Enz Micro Technology, **3(3)**, 1−10.

[4] Tan, T. W., Wang, F. and Deng, L. (2003) Present situation and prospect for bioenergy [J]. Modern chemical industry, **23(9)**, 8−14.

[5] Wang, Q. H., Ma, H. Z., Wang, X. M., *et al*. (2004) Resource recycling technology of foodwastes [J]. Modern Chemical Industry, **24(7)**, 56−59.

[6] Ren, N. Q., Lia, J. Z., Lib, B. K., *et al*. (2006) Bio-hydrogen production from molasses by anaerobic fermenta-

tion with a pilot-scale bioreactor system [J]. International Journal of Hydrogen Energy, **31**, 2147−2157.

[7] Li, Y. J., Li, A. M. and Gao, N. B. (2002) An approach to a subject of innocuous in cineration of municipal sold-waste [J]. Journal of Shenyang Institute of Aeronautical Engineering, **19(3)**, 57−60.

[8] Gomez, X., Moran, A., Cuetos, M. J., *et al*. (2006) The production of hydrogen by dark fermentation of municipal solid wastes and slaughterhousewaste: A two-phase process [J]. Sour, **157**, 727−732.

[9] Levin, D. B., Islam, R., Cicek, N. and Sparling, R. (2006) Hydrogen production by Clostridium thermocellum 27405 from cellulosic biomass substrates [J]. Hydrogen Energy, **31(11)**, 1496−1503.

[10] Zuo, Y., Zuo, J. N., Zhang, W., *et al*. (2004) A study on steady anaerobic bio-hydrogen production using river sediments as seed sludge [J]. China biogas, **22(4)**, 22−25.

[11] Tai, M. L. and Liu J. X. (2005) Factors of effecting hydrogen production from anaerobic fermentation of excess seweage sludge [J]. Environmental Science, **26(2)**, 98−111.

[12] Ginkel, S. W., Oha, S.-E. and Logan, B. E. (2005) Biohydrogen gas production from food processing and domestic wastewaters [J]. International Journal of Hydrogen Energy, **30**, 1535−1542.

[13] Zhu, H. G., Parker, W., Basnar R., *et al*. (2008) Biohydrogen production by anaerobic co-digestion of municipal food waste and sewage sludges [J]. International Journal of Hydrogen Energy, **33**, 3651−3659.

[14] Krupp, M. and Widmann, R. (2008) Biohydrogen production by dark fermentation: Experiences of continuous operation in large lab scale [J]. International Journal of Hydrogen Energy, **28**, 1−8.

[15] Ela Eroglu, Inci Erolu, Ufuk Gündüzb, *et al*. (2006) Biological hydrogen production from olive mill wastewater with two-stage processes [J]. International Journal of Hydrogen Energy, **31**, 1527−1535.

[16] Li, D. M. and Chen, H. Z. (2007) Biological hydrogen production from steam-exploded strawby simultaneous saccharification and fermentation [J]. International Journal of Hydrogen Energy, **32**, 1742−1748.

[17] Zabut, B., Kahlout, K. E., Yücel M., *et al*. (2006) Hydrogen gas production by combined systems of Rhodobacter sphaeroides O. U. 001 and Halobacterium salinarum in a photobioreactor [J]. International Journal of Hydrogen Energy, **31(11)**, 1553−1562.

[18] State Environmental Protection Administration of China (2002) Detecting methods of water and wastewater (Edition Ⅳ) [M]. Beijing, China Environmental Science Press.

[19] Zhu, N. W., Min, H., Cheng, M. C., *et al*. (1996) The study of Determination on TTC-Dehydrogenase Activity [J]. China Biogas, **14(2)**, 3−5.

[20] An, L. C., Niu, H., Zeng C., *et al*. (1996) A Study on the Measurement of dehydrogenase activity in activated sludge [J]. Pollution control Technology, **9(3)**, 186−188.

[21] Pan, C. M., Fan, Y. T., Xing, Y., *et al*. (2008) Statistical optimization of process parameters on bio-hydrogen production from glucose by Clostridium sp. Fanp2 [J]. Bioresour Biotechchnol, **99**, 3146−3154.

[22] Lay, J. J., Lee, Y. J. and Noike, T. (1999) Feasibility of biological hydrogen production from organic fraction of municipal solid waste [J]. Wat. Res, **33(11)**, 2579−2586.

[23] Cai, M. L. and Liu, J. X. (2005) Factors of effecting hydrogen production from anaerobic fermentation of excess sewage sludge [J]. Environmental Science, **26(2)**, 97−100.

[24] Bartons, Bullock, C. and Weir, D. (1996) The effects of uktrasound on the activities of some glycosidase enzymes of industrial importance [J]. Enzyme Microbe Technology, **18(3)**, 190−194.

[25] Tang, N., Chai, L. Y., Min X. B., *et al*. (2005) Characteristic bacterial number of anaerobic activated sludge with dehydrogenase activity as indicator [J]. Journal of Microbiology, **25(2)**, 31−34.

[26] Jeffcres T. W. and Kurtzman C. P. (1994) Strain selection, taxonony, and genetics of xylose-fermentation yeast [J]. Enzyme Microb Technology, **16**, 922−931.

 

**Natural Science, 2009, 1, 17-22** **NS**

# Research on the Graft Copolymerization of EH-lignin with acrylamide

**Run Fang[1,2], Xian-Su Cheng[*1], Jian Fu[1], Zuan-Bin Zheng[1]**

[1]College of Material Science and Engineering, Fuzhou University, Fuzhou 350002, China; [2]Department of Chemistry and Chemical Engineering, Minjiang University, Fuzhou 350011, China.
[*]Corresponding author: chengxiansu@fzu.edu.cn

Received 13 April 2009; revised 14 May 2009; accepted 23 May 2009.

## ABSTRACT

**Lignin isolated from enzymatic hydrolyzed cornstalks (EH-lignin) is a renewable natural polymer noted for its versatility and applicability in a variety of uses. Graft copolymerization of EH-lignin with acrylamide (AM) and the application of this copolymer as a flocculant in dye wastewater treatment were studied in this article. The influences of some factors on yield of copolymer and the grafting ratio were investigated and the structure of EH-lignin/AM graft copolymer was characterized by FT-IR. According to the yield and the grafting ratio, the optimum conditions for graft copolymerization were as follows: initiator $K_2S_2O_8$-$Na_2S_2O_3$ with a quantity 3 wt% of EH-lignin, mass ratio of AM to EH-lignin was 2~3, reaction time 4h and temperature at 50℃. It was found that the absorption capacity of graft copolymer to two azo-dyes was enhanced with the increase of grafting ratio. Furthermore, the residue concentration of EH-lignin/AM graft copolymer remained in the supernatant after flocculation was much lower than that of pure EH-lignin.**

**Keywords:** Lignin; Acrylamide; Graft Copolymerization; Dye Wastewater; Decoloration

## 1. INTRODUCTION

At present, the fossil resources are rapidly running out and the environmental pollutions are getting even more serious throughout the world. Great attention has been paid to the development of sustainable technologies based on renewable raw materials [1,2,3,4]. As a natural polymer, lignin is a renewable and biodegradable resource and noted for its versatility and applicability in a variety of uses. Making use of these biomaterials will not only enhance the economic benefit of bioengineering but also diminish environmental pollutions [5,6].

EH-lignin is a novel ornanosolv lignin isolated from the residue of enzymatically hydrolyzed cornstalks as a by-product of fuel ethanol industry [7]. Compared with traditional lignosulfonate or alkali lignin, EH-lignin possesses some valuable characteristics: lower content of sugar, less impurities and narrow molecular weight distribution. Furthermore, since the enzymatic hydrolysis process of the cornstalks is carried out under relatively mild conditions, many functional groups such as phenolic hydroxyl, alcoholic hydroxyl and methoxyl are well preserved in EH-lignin [8,9,10].

Due to its abundant functional groups, EH-lignin can be used in dye wastewater treatment by adsorbing dyes through hydrogen bonding under acidic conditions. However, the concentration of residue lignin remains in supernatant after flocculation is very high, which may leads to a secondary pollution. In order to minimize the potential secondary pollution, graft copolymerization of EH-lignin with acrylamide (AM) was studied in this paper. The effects of some factors on the copolymerization were investigated. The structure of EH-lignin/AM copolymer was analyzed by FT-IR and its application in the dye wastewater treatment was evaluated. The residue concentration of this flocculant remains in the supernatant after flocculation was measured.

## 2. EXPERIMENTAL

### 2.1. Materials

EH-lignin was supplied by Tianguang fuel ethanol company (He'nan, China) in powder form and purified in laboratory according to procedures described in our previous article [4]. Characteristics of purified EH-lignin are shown in **Table 1**. The details of two azo-dyes, acid red 274 (AR 274) and reactive red X-3B (RR X-3B), were shown in **Fig. 1** and **Table 2**. Acrylamide were purchased from Guanghua chemical reagent Co., Ltd, China. All other reagents were of analytical grade.

**Table 1.** Characteristics of EH-lignin.

| EHLignin | Residual sugar/% | Ash /% | Phenolic hydroxyl/mmol.g$^{-1}$ | Mw | Mw/Mn |
|---|---|---|---|---|---|
| | 0.22 | 0.39 | 4.25 | 2062 | 1.22 |

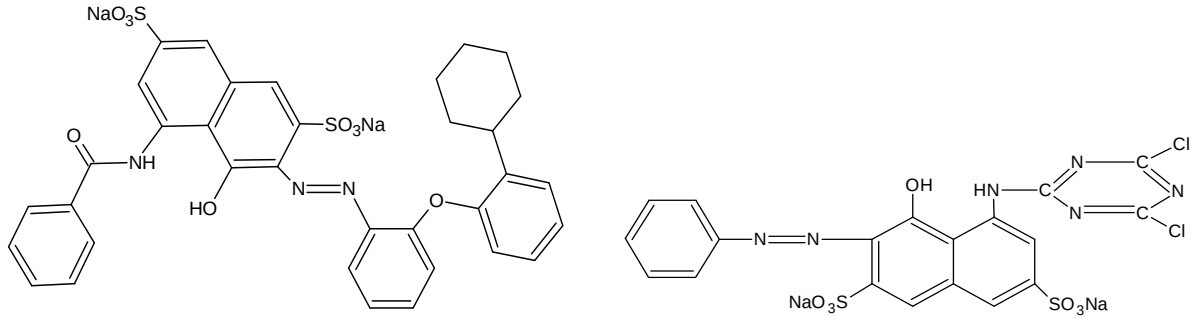


(a) (b)

**Figure 1.** Molecular structure of (a) Acid red 274 and (b) Reactive red X-3B.

**Table 2.** Details of the dyes.

| Dyes | Abbreviation | Molecular formula | CAS number | λmax(nm) |
|---|---|---|---|---|
| Acid red 274 | AR 274 | $C_{35}H_{31}N_3Na_2O_9S_2$ | 72828-83-2 | 527 |
| Reactive red X-3B | RR X-3B | $C_{19}H_{10}Cl_2N_6Na_2O_7S_2$ | 12226-03-8 | 538 |

## 2.2. Synthesis and Characteristics of EH-lignin/ AM Graft Copolymer

Graft copolymerization reactions were carried out in a jacketed reactor flask equipped with a stirrer and a reflex condenser under $N_2$ protection. Appropriate amount of EH-lignin, AM and initiators were dissolved in NaOH aqueous solution and then reacted at different temperatures for a period of time. When a reaction was finished, copolymer product was precipitated by acidification and isolated in a centrifuge. In order to remove monomers, EH-lignin/AM graft copolymers were washed by distilled water and then vacuum dried.

Viscosity measurement of lignin/AM copolymer in water solution was conducted by an Ubbelohde type viscometer at 30.0±0.1℃. Extrapolation procedure from data obtained for 5 concentrations of solutions was used to calculate [η] from Huggins equation, $\eta_{sp}/c=[\eta]+k[\eta]^2c$. The intrinsic viscosity was then used to evaluate the molecular weight of graft copolymers prepared with different initiators.

The chemical structure of graft copolymer was analyzed using FT-IR2000 spectrometer (Perkinelmer, U. S.) and the spectra were recorded in the range of 500-4000 $cm^{-1}$.

Yield of EH-lignin/AM copolymer and the grafting ration were determined by **Eq.1** and **Eq.2** respectively.

Yield

$$Y(\%)=\frac{W_2}{W_0+W_1}\times 100\% \quad (1)$$

Grafting ratio

$$GR(\%)=\frac{W_2-W_0+W_3}{W_0-W_3}\times 100\% \quad (2)$$

where $W_0$ is the weight of EH-lignin; $W_1$ is the weight of AM monomer; $W_2$ is the weight of the graft copolymer; $W_3$ is the weight of lignin remained in the supernatant.

## 2.3. Adsorption and Decoloration of AR 274 and RR X-3B Dye Wastewater

The adsorption and decoloration of AR 274 and RR X-3B dye wastewater by EH-lignin and EH-lignin/AM grafted copolymer was investigated by static adsorption method. Firstly, a certain amount of flocculant was weighed and dissolved in 2ml 1%NaOH aqueous solution. Afterward, 200ml dye wastewater with a concentration of 500mg/L was added into aforesaid copolymer solution, stirring 3 min to make sure the mixture well-mixed and then kept undisturbed for 1h. Finally, the solution was acidified with HCl to pH=4 and then filtered after another 10 min standing. The concentrations of dye wastewater before and after treatment were measured at λmax mentioned in **Table 2** by UV-2450 spectrophotometer. The total organic carbon (TOC) content of the supernatant was measured by TOC-V analyzer (Shimadzu, Japan) to evaluate the residue amount of the flocculant and the dyes remained in the supernatant after flocculation. The absorption amount, decoloration rate and TOC removal can be calculated by **Eq.3**, **Eq.4** and **Eq.5** respectively.

Adsorption amount

$$Q=\frac{(C_0-C)\times V}{W} \quad (3)$$

Decoloration rate

$$E=\frac{A_0-A}{A_0}\times 100\% \quad (4)$$

TOC removal rate

$$R = \frac{B_0 - B}{B_0} \times 100\% \quad (5)$$

where Q is the adsorption amount, mg/g; $C_0$ and C are the concentrations of the dye solution before and after treatment, mg/L; V is the volume of dye solution, L; W is the amount of graft copolymer, g; E is decoloration rate; $A_0$ and A are the absorbance of the dye solution before and after treatment; R is the TOC removal rate; $B_0$ and B are the TOC values of the dye solution before and after treatment.

## 3. RESULTS AND DISCUSSION

The effects of various factors on the yield of copolymer and the grafting ratio were investigated to determine the optimum conditions for graft copolymerization. The basic reaction conditions of these experiments were as follows: the dosage of EH-lignin was 2.0g, acrylamide was 4.0g, 100g 1% NaOH aqueous solution was used as solvent, the amount of $K_2S_2O_8$-$Na_2S_2O_3$ was 3% of the weight of EH-lignin, the reaction temperature was 50℃ and the reaction time was 4h.

### 3.1. Effects of Some Factors on Graft Copolymerization

#### 3.1.1. Effects of Different Kinds of Initiators on Graft Copolymerization

The graft copolymerization of EH-lignin with AM was carried out in aqueous solution, therefore six water-soluble radical initiators were chosen and their effect on grafted copolymerization was studied. The results were showed in **Table 1** and the synthesis conditions were as follows: weight of lignin was 2.0g, acrylamide 4.0g, reaction temperature was 50℃, reaction time was 4h and the dosage of initiator was 3% of the weight of EH-lignin.

Since the raw materials and the reaction procedures are identical, the chemical structure of lignin/AM copolymers initiated by different initiators is quite similar to each other. Therefore, higher [η] of a lignin/AM copolymer's aqueous solution may indicates a larger molecular weight of this copolymer. It can be seen in **Table 1**

**Table 3.** Effects of different initiators on yield and intrinsic viscosity of the graft copolymers.

| Initiator | Yield/% | [η]/mL.g$^{-1}$ |
|---|---|---|
| $Fe^{2+}$-$H_2O_2$ | 34.30 | 35.76 |
| $(NH_4)_2Ce(NO_3)_6$ | 30.86 | 34.51 |
| $K_2S_2O_8$ | 37.83 | 35.37 |
| $(NH_4)S_2O_8$ | 34.55 | 37.15 |
| $K_2S_2O_8$-$NaHSO_3$ | 37.40 | 36.93 |
| $K_2S_2O_8$-$Na_2S_2O_3$ | 39.60 | 37.86 |

that the graft copolymer initiated by $K_2S_2O_8$-$Na_2S_2O_3$ has the largest yield and highest intrinsic viscosity, which means this binary-initiating system is more effective in grafting AM onto EH-lignin. For this reason, $K_2S_2O_8$-$Na_2S_2O_3$ was employed in our further research on the graft copolymerization of EH-lignin with AM.

#### 3.1.2. Effect of Initiator Dosage on Graft Copolymerization

The effect of initiator dosage on graft copolymerization was evaluated considering the yield of copolymer and the grafting ratio. The results were shown in **Fig. 2**. It was found that the yield of the copolymer and the grafting ratio increased with increasing initiator dosage at first. However, when the initiator dosage was more than 3% of the weight of lignin, Y(%) and GR(%) increased slowly and then decreased when the dosage of initiator reach 5%.

In the process of the copolymerization, the binary-initiating system of $K_2S_2O_8$-$Na_2S_2O_3$ generated free radicals to initiate the polymerization of PAM and the graft copolymerization of EH-lignin with AM or with PAM chains. On one hand, high free radical concentration may enhance the possibility of graft copolymerization and increase the yield and molecular weight of copolymer; on the other hand, it will lower the polymerization degree of PAM that may graft onto EH-lignin and decrease the molecular size of copolymer. Therefore, Y(%) and GR(%) reach their maximum when the contradiction reaches a equilibrium and the optimum dosage of initiator is 3% of the weight of EH-lignin.

#### 3.1.3. Effect of Acrylamide Dosage on Graft Copolymerization

The mass ratio of acrylamide to EH-lignin is another important factor that may affect the yield of copolymer and the grafting ratio. It can be found in **Fig. 3** that when the dosage of AM was no more than 6g, the grafting ratio of EH-lignin/AM copolymer increased quickly

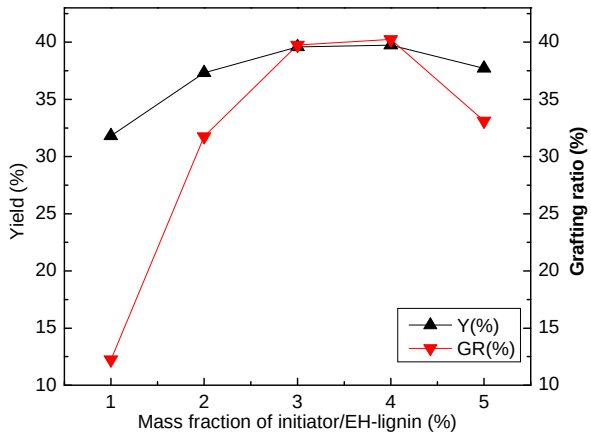


**Figure 2.** Effect of initiator dosage on the yield of copolymer and the grafting ratio.

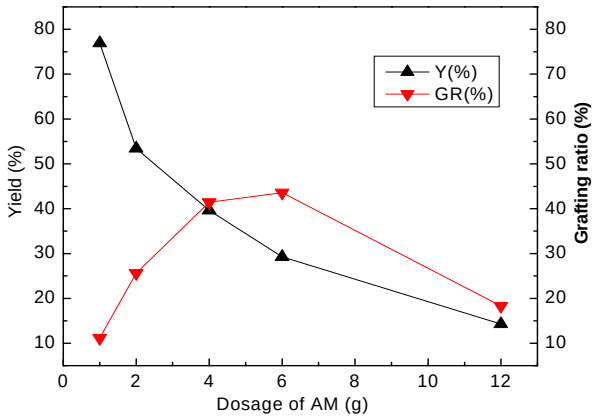


**Figure 3.** Effect of AM dosage on the yield of copolymer and the grafting ratio (the dosage of EH-lignin is 2g).

as the mass ratio of AM to EH-lignin increased. This is because the higher AM concentration can make it easier for EH-lignin to come into contact with monomer and then speed up graft copolymerization and improve grafting ratio. However, when the concentration of the AM is higher than a certain level, the probability of the homopolymerization of AM will increase rapidly. This reaction, which leads to the formation of PAM, will compete with graft copolymerization and diminish the grafting ratio. The yield of copolymer, on the contrary, decreased gradually as the dosage of AM increased from 1g to 12g. This phenomenon can be ascribed to the rising water-solubility of the copolymer. It has been mentioned above that higher monomer concentration will enhance the probability of homopolymerization of AM and extend the length of some PAM chains that have been grafted onto EH-lignin. Thus, the water-solubility of EH-lignin/AM copolymer increases with the rise of AM dosage and the quantity of copolymer that can be separated from aqueous solution declines simultaneously. We can see from the above analysis that the ideal dosage of acrylamide is 4~6g or the mass ratio of AM to EH-lignin is 2~3.

### 3.1.4. Effects of Reaction Time and Reaction Temperature on Graft Copolymerization

The effects of reaction time and reaction temperature on the yield of copolymer and the grafting ratio were shown in **Fig. 4** and **Fig. 5** respectively. From **Fig. 4**, we could see the yield and grafting ratio improved rapidly as the reaction time increased from 2h to 4h. When the reaction time was further prolonged, the growth of yield and grafting ratio became unremarkable. This phenomenon is similar to the regular pattern of radical polymerization. The graft copolymerization took place mostly in the period of initiation and the speed of the copolymerization was high at first. However, as the concentration of acrylamide and initiators declined with elapsed time, the graft copolymerization slowed down and the yield and grafting ratio stopped growing.

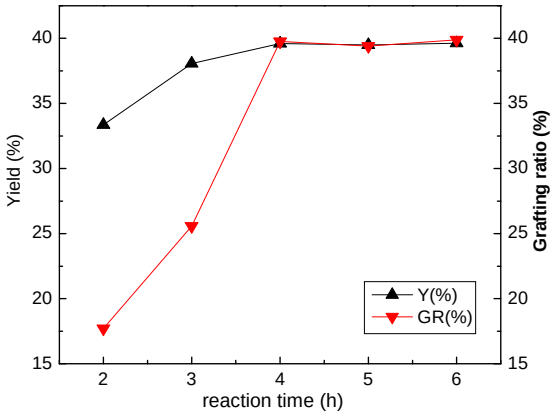


**Figure 4.** Effect of reaction time on graft copolymerization.

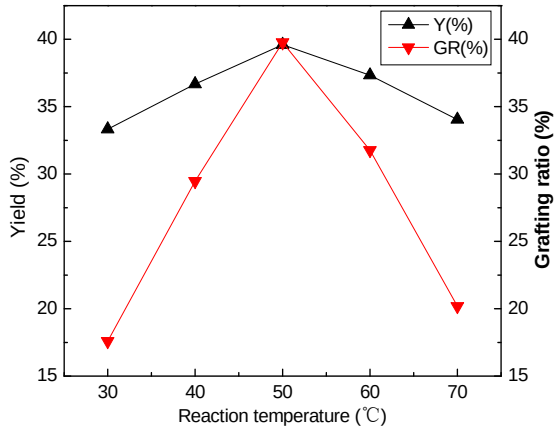


**Figure 5.** The influence of reaction temperature on graft copolymerization.

The influence of different reaction temperature on graft copolymerization was shown in **Fig. 5**. The highest yield and grafting ratio can both be reached at 50℃ and this is the ideal reaction temperature for the binary-initiating system of $K_2S_2O_8$-$Na_2S_2O_3$. It is well known that low reaction temperature will postpone the decomposition of initiator and restrain the copolymerization. On the contrary, when the reaction temperature was higher than 50℃, the decomposition of initiator would be too fast and the possibility of radical transfer would be greatly enhanced, both of which will lead to the decrease of yield and grafting ratio.

## 3.2. FT-IR Spectral Analysis

The FT-IR spectra of EH-lignin and EH-lignin/AM copolymer were shown in **Fig. 6**. It can be seen from the FT-IR spectrum of EH-lignin/AM copolymer, compared with pure EH-lignin, the relative intensity of the band at about 1700 $cm^{-1}$ increased significantly. This adsorption peak is assigned to the vibration absorbance of C=O and the rise of its intensity implies that AM have been grafted onto EH-lignin. Furthermore, the intensity of the

 

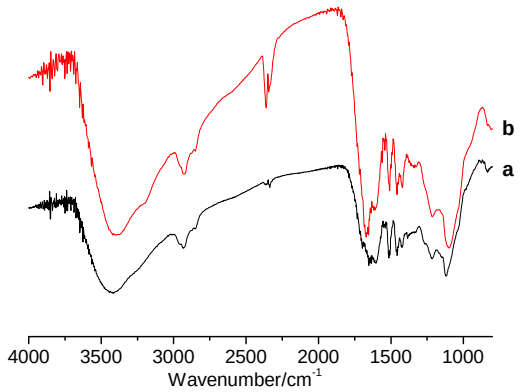


**Figure 6.** FT-IR spectra of EH-lignin and EH-lignin/ AM copolymer (a EH-lignin; b EH-lignin/AM copolymer).

band at 1020 $cm^{-1}$, which is assigned to the absorbance of N-H, also increased and this is another proof of the successful graft copolymerization. All the information provided by FT-IR analysis had indicated that the product is an EH-lignin/AM copolymer with numerous functional groups, such as phenolic hydroxyl (3400$cm^{-1}$), carbonyl (1700$cm^{-1}$) and amide (1550 and 1020$cm^{-1}$) groups [11,12].

### 3.3. Adsorption and Decoloration of Dye-Wastewater by EH-lignin/AM Copolymer

The adsorption and decoloration of AR 274 and RR X-3B dye wastewater by EH-lignin/AM grafted copolymer and pure EH-lignin was investigated according to the procedures described in 2.3. The effect of grafting ratio on the adsorption capacity of graft copolymer was shown in **Fig. 7**. It was found that the absorption capacity of EH-lignin/AM copolymer to both dye wastewaters increased remarkably with the rising of grafting ratio. When the grafting ratio was 43.6 %, the maximum adsorption amount of AR 274 and RR X-3B by graft copolymer may reach 751mg/g and 512mg/g respectively.

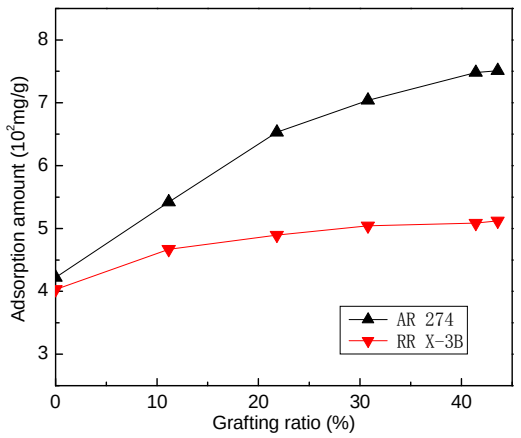


**Figure 7.** Effect of grafting ratio on the adsorption capacity of EH-lignin/AM copolymer.

The flocculation of dye colloids result from various mechanisms, including electrostatic attraction, sorption (related to protonated amine groups and phenolic hydroxyl), and bridging (related to the high molecular weight of the polymer) [13]. There are sulfonic, carbonyl and amino groups in AR 274 and RR X-3B. The sulfonic groups can be electrostatic attracted by protonated amide groups of the EH-lignin/AM graft copolymer and the amino groups can from hydrogen bonding with phenolic hydroxyl groups of the copolymer and EH-lignin. Thus, higher grafting ratio will help to strengthen the supramolecular interaction between dyes and graft copolymers, which can bind copolymer molecules closer, trap and flocculate dyes more effectively.

The relationship between the dosage of coagulants and the decoloration rate of dye wastewater was shown in **Fig. 8**. The concentration of AR 274 dye wastewater was 500mg/L and the grafting ratio of EH-lignin/AM copolymer was 30.8%. It can be seen in **Fig. 8** that the decoloration rate of dye wastewater increased rapidly as the dosage of both flocculants increased from 50mg/L to 200mg/L. When the dosage of flocculant reached 800mg/L, the AR 274 dye had almost been removed completely.

Results also showed that both pure EH-lignin and EH-lignin/AM graft copolymer performed well in the removal of AR 274 from dye wastewater when the dosage of flocculant is higher than 200mg/L. As has been mentioned in 3.2, EH-lignin and lignin/AM copolymer possess lots of functional groups, such as phenolic hydroxyl, carbonyl and amide groups. Meanwhile, AR 274 also contains alcoholic hydroxyl and carbonyl groups, which leads to the adsorption of dye molecules on EH-lignin and EH-lignin/AM copolymer through hydrogen bonding. Subsequently, the flocculant molecules bridge to each other under acidic environment and form large flocs, which will trap the dyes dissolved in wastewater and then precipitate simultaneously.

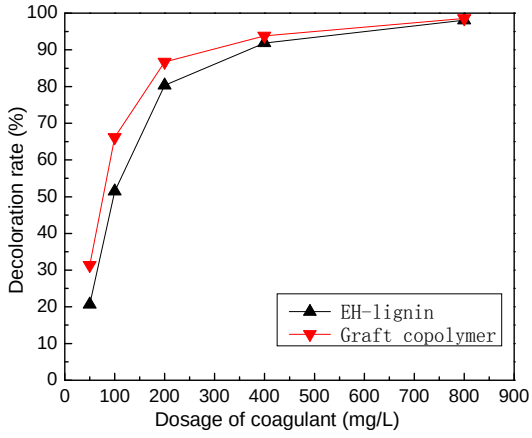


**Figure 8.** Effect of coagulant dosage on the decoloration rate of AR 274 wastewater.

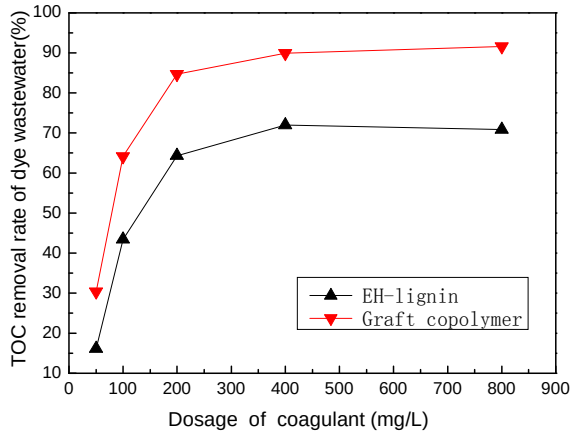


**Figure 9.** TOC removal rate of dye wastewater after flocculation.

The residue of EH-lignin and EH-lignin/AM copolymer in the supernatant after flocculation was measured by TOC test to evaluate the potential secondary pollution of this flocculant. These experiments were carried out with various dosage of flocculant at pH=4. It can be found in **Fig. 9** that, compared with the decoloration rate of AR 274 wastewater flocculated by both flocculants, the TOC removal rate of these samples are much lower. This phenomenon implies that part of EH-lignin and EH-lignin/AM copolymer remains in the supernatant after flocculation. Furthermore, TOC removal rate of the dye wastewater treated by EH-lignin/AM graft copolymer is much higher than that of pure EH-lignin, which means the graft copolymerization of EH-lignin with AM will help to minimize the residue amount of this copolymer in wastewater and diminish the potential secondary pollution.

## 4. CONCLUSIONS

The preparation and the application of EH-lignin/AM graft copolymer were presented in this article. The optimum synthesis conditions were discussed and the functional groups of the copolymer were characterized by FT-IR The adsorption and decoloration of two azo-dye wastewater by EH-lignin/AM grafted copolymer and pure EH-lignin was investigated.

1) The optimum conditions for the graft copolymerization of EH-lignin with acrylamide were as follows: initiator $K_2S_2O_8$-$Na_2S_2O_3$ with a quantity 3 wt% of EH-lignin, mass ratio of AM to EH-lignin was 2~3, reaction time 4h and temperature at 50℃.

2) FT-IR spectrum of EH-lignin/AM copolymer indicated that acrylamide had been grafted onto EH-lignin successfully and the copolymer had numerous functional groups, such as phenolic hydroxyl, carbonyl and amide groups.

3) The absorption capacity of EH-lignin/AM copolymer to dye wastewater was enhanced with the increase of grafting ratio. Both pure EH-lignin and EH-lignin/AM graft copolymer performed well in the removal of AR 274 from dye wastewater when the dosage of flocculant is higher than 200mg/L. However, the residue concentration of EH-lignin/AM graft copolymer remained in the supernatant after flocculation was much lower than that of pure EH-lignin.

## ACKNOWLEDGEMENTS

The author thanks Key Laboratory of Cellulose and Lignocellulosics Chemistry, Guangzhou Institute of Chemistry, Chinese Academy of Sciences for financial support (LCLC-2004-158).

## REFERENCES

[1] Rafael, L., Lorenzo, H. D. and Juan, M. (2008) Biofuels: A technological perspective. Energy Environ. Sci., **1**, 542−564.

[2] Roussy, J., Van, V. M. and Dempsey, B. A. (2005) Influence of chitosan characteristics on the coagulation and the flocculation of bentonite suspensions. Water Research, **39(14)**, 3247−3258.

[3] Sarasa, J., Roche, M. P. and Ormad, M. P. (1998) Treatment of a wastewater resulting from dyes manufacturing with ozone and chemical coagulation. Water Research, **32(9)**, 2721−2727.

[4] Bousher, A., Shen, X. and Edyvean, R. G. (1997) Removal of coloured organic matter by adsorption onto low-cost waste materials. Water Research, **31(8)**, 2084−2092.

[5] Wu, Y., Zhang, S. and Guo, X. (2008) Adsorption of chromium (III) on lignin. Bioresource Technology, **99(16)**, 7709−7715.

[6] Dizhbite, T., Zakis, G. and Kizima, A. (1999) Lignin-a useful bioresource for the production of sorption-active materials. Bioresource Technology, **67(3)**, 221−228.

[7] Cheng, X. S. and Liu X. L. (2006) Separation of lignin from cornstalks residue by enzymatic hydrolysis and its properties. Modern Chemical Industry, **26**, Supplement, 99−102.

[8] Fang, R., Chen, Y. P. and Cheng X. S. (2007) Application of organosolv lignin on polymer synthesis and modification. Journal of Cellulose Science and Technology, **15(3)**, 56−60.

[9] Zhang, X. H., Cheng, X. S. and Tang, J. (2006) Adsorption of bromelain with HBS lignin and its derivatives. Chinese Journal of Process Engineering, **6**, 87−90.

[10] Chen, Y. P., Zhang, T. T. and Cheng X. S. (2005) The adsorption of phenol by high boiling solvent lignin. Journal of Cellulose Science and Technology, **13(2)**, 20−25.

[11] Zhao, B. Y., Hu, K. A., Fan, Y. Z., Zhu, P. F. and Wu, R. J. (2000) Infrared spectroscopic study on lignosulfonic acid and its derivatives. Chinese Journal of Analytical Chemistry, **28**, 716−719.

[12] Chen, Y. P. and Cheng X. S. (2008) Preparation and characteristic analysis of rice husk high boiling solvent lignin. Journal of Forestry Research, **19**, 159−163.

[13] Roussy, J., Van, V. M. and Dempsey, B. A. (2005) Influence of chitosan characteristics on the coagulation and the flocculation of bentonite suspensions. Water Research, **39(14)**, 3247−3258.

 

**Natural Science, 2009, 1, 23-29** **NS**

# Optimization of solvent extraction conditions for total carotenoids in rapeseed using response surface methodology

**Ling Wang[1], Yun Liu[1,*]**

[1]College of Life Science and Technology, Huazhong University of Science and Technology, Wuhan 430074, P. R. China.
Email: [*]liuyunprivate@sina.com

Received 10 May 2009; revised 16 May 2009; accepted 19 May 2009.

## ABSTRACT

**The optimum total carotenoids (TC) extraction from rapeseed with solvent extraction method by UV-visible spectrophotometer determination was investigated by using response surface methodology (RSM). Extraction duration, repeated extraction cycles, solvent-solid ratio and extraction temperature were assumed to be the most important factors affecting solvent extraction for the determination of TC. Optimum solvent extraction conditions for maximizing the determination of TC were: extraction duration 7.3h, repeated extraction three times, ratio of solvent-solid (v/w, mL/mg) 29:1, extraction temperature 42°C. Under the optimal conditions, the yield of TC was up to 4.79 mg /100g. The model had a satisfactory coefficient of $R^2$ (= 0.912) and verified experimentally. The results showed that the conditions were mild and useful for maximizing a quantitative spectrophotometer determination of TC in rapeseed.**

**Keywords:** Carotenoids; Optimization; Solvent Extraction; Response Surface Methodology; Rapeseed

## 1. INTRODUCTION

Carotenoids are a group of phytochemical bioactive compounds that are responsible for different colors of various plants and microorganisms but not animals [1]. It has been found that carotenoids can play an important role in the prevention of various types of cancer as well as other important ‘‘lifestyle- related’’ diseases, such as cardiovascular disease and age-related macular degeneration due to their antioxidant activity [2,3,4]. In addition to being potent antioxidants some carotenoids also contribute to provitamin A function [5]. Although the chemistry properties of carotenoids have been extensively studied their bioavailability, metabolism and biological functions are only investigated recently [6,7]. In recent years the antioxidant properties of carotenoids have become the major focuses for researches, particularly focused on the role of lycopene in human health [8,9]. About 90% of the carotenoids in the diet and human body are represented by β-carotene, α-carotene, lycopene, lutein and cryptoxanthin [10].

As the increasing of health-conscious and the demand for carotenoids, researchers shifted their attentions from chemical synthesis to natural products isolated from plants and microorganisms biological sources [11,12]. Rapeseed containing around 40% oil is one of the most important vegetable oil materials in the world. The total production of rapeseed plant all over the world was 46.2 Mt in 2005 [13]. Rapeseed contains rich carotenoids, such as β-carotein, α-carotein and lutein, which can contribute to prolong the rapeseed oil shelf life and increase oil nutrition [14,15]. Many effective methods for carotenoids extraction from biological sources have been intensively employed, such as solvent extraction, solid phase extraction (SPE) and supercritical fluid extraction (SFE) [12,16,17]. Above these methods, solvent extraction method is universally application for extraction total carotenoids (TC) because solvent extraction method is relative simple and low cost [18,19,20,21]. However, the extraction of TC from rapeseed was rarely reported so far.

The most commonly used techniques for TC detection are UV-visible spectrophotometry, mass spectrometry and hydrogen or carbon nuclear magnetic resonance spectroscopy ($^1$H-NMR, $^{13}$C-NMR), coupled or not with chromatographic techniques [22,23]. Regardless of the technique utilized, carotenoid extraction is highly influenced by procedural variables such as type of sample, type and ratio of solvents, extraction duration, repeated extraction times, storage conditions, etc. Therefore, the objective of this work was to establish a solvent extraction method for a quantitative spectrophotometer determination of TC. Rapeseed was selected as representative due to its abundance all over the world. Response sur-

face methodology (RSM) was employed to optimize the extraction conditions, which could maximize the determination of TC in rapeseed.

## 2. MATERIALS AND METHODS

### 2.1 Materials

Rapeseed (Brassica napus L.) was provided by Rapeseed Engineering Center of Huazhong University of Agriculture. The raw material consisted of moisture 2.9 ± 0.05%, kernel 73.4 ± 0.26%, and seed capsule 26.6 ± 0.02%. Hexamethylene, petroleum ether, chloroform, acetone and methanol were of analytic grade.

### 2.2 Experimental Design

Six extraction solvents of hexamethylene, petroleum ether, chloroform, acetone, methanol and mixture of petroleum ether and acetone were tested to select the most optimum extraction solution for TC extraction. 3-5 g rapeseed was grinded into powder in a glass mortar and screened with 100 mesh sieve. Portions of ground rapeseed powder of 50mg (dry weight) were transferred to 40mL beakers added with 5mL extraction solvent and wrapped with aluminum foil. The samples were constantly agitated (Sisatom magnetic agitator) according to the extraction duration, protected from light at room temperature (23°C). In the preliminary study, variables affecting TC extraction were solid-solvent ratio, extraction duration, extraction repeated cycles and extraction temperature. Response surface methodology (RSM) was used to optimize the above parameters. A four-factor- five-level centre composite design was adopted to optimize the extraction conditions for analysis of the TC in rapeseed. The quadratic response surface model fitted **Eq.1**:

$$Y = b_0 + \sum_{i=1}^{k} bi\ Xi + \sum_{i=1}^{k} bii\ X_i^2 + \sum_{i=1}^{k}\sum_{j>i}^{k} b_{ij}\ X_i\ X_j + \mathrm{e} \quad (1)$$

where Y standed for the total carotenoids yield, b0 denoted the model intercept, i and j were the linear and quadratic coefficients, respectively, bi, bii and bij were the regression coefficient, k was the number of factors studied and optimized in the experiment and e was the random error. Statistical Analysis System (SAS Institute Inc, Cary, NC, USA) was used to fit the second order polynomial equation to the experimental data.

The goodness of fit of the model was evaluated by the coefficient of determination ($R^2$) and the analysis of variance (ANOVA). Quadratic polynomial equations were attained by holding one of the independent variances at a constant value and changing the level of the other variables.

### 2.3 Total Carotenoids Quantification

After extraction, the samples were filtered on filter paper, their volume was made up to 3mL, and they were stored in an amber flask (~10mL) filled with $N_2$. To determine the amount of total carotenoids extracted, UV-visible spectrophotometer (UNICO UV-2802, USA) was used for a spectral window between 380 and 750 nm, in triplicate. The absorbance value of carotenoids extract was monitored at 445 nm. The total carotenoids (TC) yield (mg/100g) was calculated according to the following **Eq.2**:

$$TC\,(mg/100g) = \frac{A \times y(mL) \times 10^6}{A_{1cm}^{\%} \times 1000 \times w} \quad (2)$$

where A was the absorbance value of extract at 445 nm, y was the volume of extract, $A_{1cm}^{\%}$ was the extinction coefficient of carotenoids, and w was the weight of rapeseed powder (g).

### 2.4 Verification of Model

Optimizations of extraction conditions, including reaction temperature, solid-solvent ration, extraction duration, and extraction repeated cycles for maximizing a quantitative UV-visible spectrophotometer determination of TC in the rapeseed were calculated by using the predictive equation from RSM. The actual determination of TC was carried out by UV-visible spectrophotometer after extraction at the optimum conditions, and the result was compared to the predicted value.

## 3. RESULTS AND DISCUSSIONS

### 3.1. The Effect of Extraction Solvents on TC Yield

Six different extraction solvents, hexamethylene, petroleum ether, chloroform, acetone, methanol and petroleum ether/acetone mixture, were employed to choose the most suitable solvent for TC extraction from rapeseed. The experimental results were shown in **Table 1**.

It was indicated from **Table 1** that the mixture solvent of petroleum ether and acetone (1:1, v/v) was the most effective solvent for TC extraction from rapeseed. As known, rapeseed contains polar carotenoid such as lutein, and nonpolar carotenoids such as β-carotene and carotenoids ester, the former is easily dissolved in polar solvent (e.g. acetone) while the latter is easily dissolved in nonpolar solvent (e.g. petroleum ether). Therefore, the

**Table 1.** Effects of extraction solvent on TC yield.

| Extraction solvents | TC yield (mg/100g) |
|---|---|
| Hexamethylene | 0.617±0.065 |
| Petroleum ether | 0.972±0.038 |
| Chloroform | 2.110±0.052 |
| Acetone | 2.438±0.063 |
| Methanol | 2.312±0.075 |
| Petroleum ether/acetone mixture(1:1,v/v) | 3.890±0.093 |

mixture solvent of petroleum ether and acetone was most suitable solvent for the TC extraction from rapeseed among the tested solvents.

## 3.2 Optimization of Extraction Conditions by RSM

In our preliminary study, variables affecting TC extraction were solid-solvent ratio, extraction duration, extraction repeated cycles and extraction temperature. The optimum experiments were conducted by using a five-level-four-factor central composite design with twelve replicates at the central point. The coded and actual levels of the three variables in **Table 2** were selected to maximize the UV-visible spectrophotometer determination of total carotenoids (TC).

**Table 2.** Coded and actual levels of four variables.

| Factors | Duration ($X_1$, h) | Repeated cycle ($X_2$) | Solid-solvent ratio ($X_3$, g/mL) | Temperature ($X_4$, °C) |
|---|---|---|---|---|
| r=2 | 10 | $5^{th}$ | 1:50 | 60 |
| 1 | 8 | $4^{th}$ | 1:40 | 50 |
| 0 | 6 | $3r^{d}$ | 1:30 | 40 |
| -1 | 4 | $2^{nd}$ | 1:20 | 30 |
| -r=-2 | 2 | $1^{st}$ | 1:10 | 20 |
| △x | 2 | 1 | 10 | 10 |

**Table 3** showed the treatments with coded levels and their experimental results of TC in rapeseed.

The TC yield ranged from 2.762mg/100g to 4.863mg /100g, and the run=20 and the run=27 had the minimum and maximum yield, respectively. Using the designed experimental data (**Table 3**), the polynomial model describing the correlation between TC yield and the four variables or conditions was obtained as follows:

**Table 3.** Coded level combinations for a four-variable central composite orthogonal and rotatable design (CCD).

| Runs | X1 | X2 | X3 | X4 | TC(Y1, mg/100g) |
|---|---|---|---|---|---|
| 1 | -1 | -1 | -1 | -1 | 3.046 ±0.061 |
| 2 | -1 | -1 | -1 | 1 | 3.726±0.053 |
| 3 | -1 | -1 | 1 | -1 | 3.192±0.047 |
| 4 | -1 | -1 | 1 | 1 | 4.006 ±0.035 |
| 5 | -1 | 1 | -1 | -1 | 3.999±0.018 |
| 6 | -1 | 1 | -1 | 1 | 3.110 ±0.009 |
| 7 | -1 | 1 | 1 | -1 | 3.665±0.016 |
| 8 | -1 | 1 | 1 | 1 | 3.898 ±0.024 |
| 9 | 1 | -1 | -1 | -1 | 4.226±0.034 |
| 10 | 1 | -1 | -1 | 1 | 4.140±0.018 |
| 11 | 1 | -1 | 1 | -1 | 3.123±0.017 |
| 12 | 1 | -1 | 1 | 1 | 2.760±0.005 |
| 13 | 1 | 1 | -1 | -1 | 3.314±0.032 |
| 14 | 1 | 1 | -1 | 1 | 4.325±0.029 |
| 15 | 1 | 1 | 1 | -1 | 4.348±0.034 |
| 16 | 1 | 1 | 1 | 1 | 3.935±0.015 |
| 17 | -2 | 0 | 0 | 0 | 4.437±0.012 |
| 18 | 2 | 0 | 0 | 0 | 4.088±0.011 |
| 19 | 0 | -2 | 0 | 0 | 4.542±0.065 |
| 20 | 0 | 2 | 0 | 0 | 2.762±0.002 |
| 21 | 0 | 0 | -2 | 0 | 3.664±0.041 |
| 22 | 0 | 0 | 2 | 0 | 4.135±0.036 |
| 23 | 0 | 0 | 0 | -2 | 3.159±0.025 |
| 24 | 0 | 0 | 0 | 2 | 3.834±0.015 |
| 25 | 0 | 0 | 0 | 0 | 4.768±0.023 |
| 26 | 0 | 0 | 0 | 0 | 4.805±0.025 |
| 27 | 0 | 0 | 0 | 0 | 4.863±0.031 |
| 28 | 0 | 0 | 0 | 0 | 4.763±0.015 |
| 29 | 0 | 0 | 0 | 0 | 4.822±0.028 |
| 30 | 0 | 0 | 0 | 0 | 4.719±0.017 |
| 31 | 0 | 0 | 0 | 0 | 4.768±0.021 |
| 32 | 0 | 0 | 0 | 0 | 4.805±0.018 |
| 33 | 0 | 0 | 0 | 0 | 4.343±0.014 |
| 34 | 0 | 0 | 0 | 0 | 4.712±0.010 |
| 35 | 0 | 0 | 0 | 0 | 4.802±0.034 |
| 36 | 0 | 0 | 0 | 0 | 4.779±0.016 |

$TC(Y_1, mg/100g)=4.77896+0.034687*X_1-0.049457*X_2-0.00073*X_3+0.097412*X_4-0.154353*X_1*X_1+0.060615*X_1*X_2-0.169996*X_1*X_3-0.043019*X_1*X_4-0.307039*X_2*X_2+0.197118*X_2*X_3-0.068865*X_2*X_4-0.245239*X_3*X_3-0.027968*X_3*X_4-0.345873*X_4*X_4$

**Table 4** showed the analysis of variance (*F*-test) for this model, and the coefficient of determination ($R^2$) was shown as 91.16%. The regression analysis showed that 91.16% of the variations were explained by the model. This indicated that the accuracy and general availability of the polynomial model was good, analysis of the response trends using the model was considered to be reasonable.

The contour and three-dimensional plots presented in Figs. 1-6 were produced for each pair of factors, whereas the other two factors were taken as a constant at their middle level.

**Fig. 1** shows the effects of extraction duration and repeated extraction cycle on the determination of TC in rapeseed. The maximum TC could be obtained with both extraction duration and repeated extraction cycle locating in the medium levels. Both Higher duration and extended extraction cycle resulted in the decrease of TC, which could be due to the equilibrium of TC dissolving

**Tab1e 4.** Analysis of variance.

| Source | D. F. | Sum of Squares | Mean of Squares | F Value | Pr＞F |
|---|---|---|---|---|---|
| Linear | 4 | 0.3153 | 0.0788 | 0.3677 | 0.8290 |
| Quadratic | 4 | 9.5318 | 2.3829 | 11.1137 | 0.0001** |
| Cross product | 6 | 1.2609 | 0.2101 | 0.9801 | 0.461 |
| Lack of fit | 10 | 4.4821 | 0.4482 | 23.8511 | 0.073 |
| Model | 14 | 11.1080 | 0.7934 | 5.7004 | 0.0035** |
| $R^2$=0.9116 | | Adj. $R^2$=0.7193 | | | |

D. F. denotes degree of freedom; **p<0.005

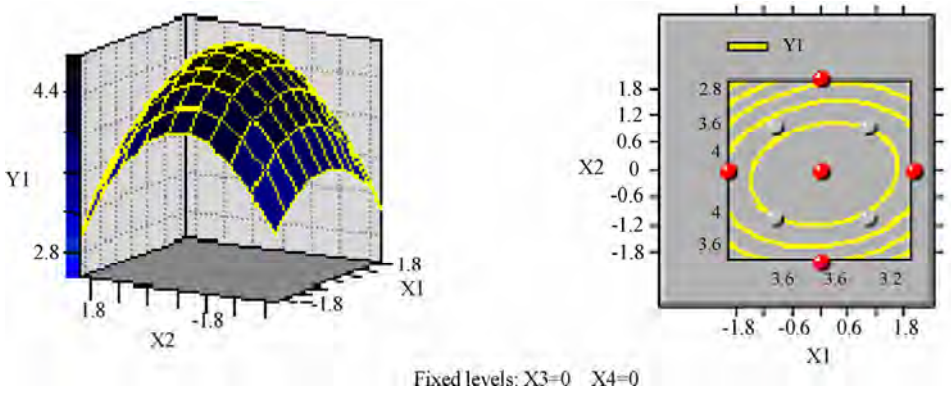


($X_1$: duration/h; $X_2$: repeated extraction cycle; $Y_1$: TC yield/(mg/100g))

**Figure 1.** Combined effect of duration and repeated extraction cycle on TC yield.

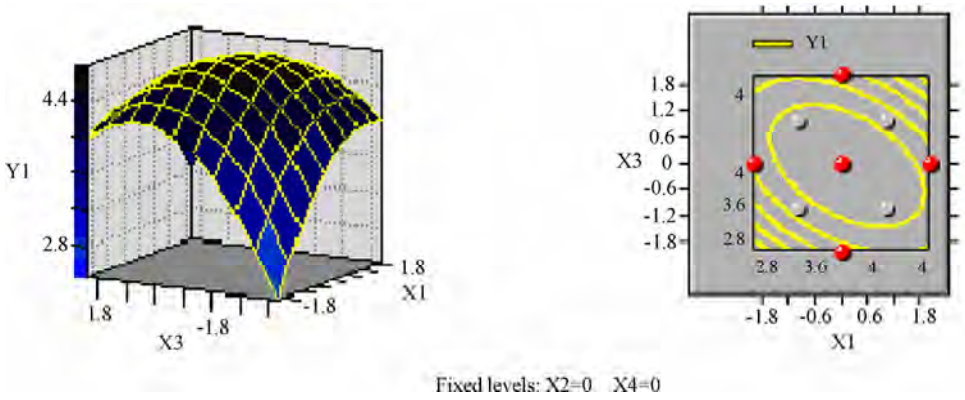


($X_1$: duration/h; $X_3$:solid-solvent ratio/(g/mL); $Y_1$: TC yield/(mg/100g))

**Figure 2.** Combined effects of extraction duration and solid-solvent ratio on TC yield.

 

into solvent obtained at 6 h and some other compounds also extracted together with TC with further increasing repeated extraction cycles.

**Fig. 2** illustrated the effects of extraction duration and solid-solvent ratio on the determination of TC in rapeseed. The maximum TC was obtained with extraction duration locating at 6h and solid-solvent ratio locating between 1:20 and 1:30. Higher extraction duration and solid-solvent ratio tended to result in a decrease of TC. This also could be due to the equilibrium of TC dissolving into solvent obtained at 6 h and some other compounds also extracted together with TC with further increasing extraction solvent.

**Fig. 3** represented the effects of extraction duration and extraction temperature on the determination of TC in rapeseed. The maximum TC was obtained with extraction duration locating at 6h and temperature locating between 40°C and 45°C. Higher extraction duration and temperature led to a decrease of TC. The reason was that the equilibrium of TC dissolving into solvent was obtained at 6 h and the cateronoids was degraded at higher temperature.

**Fig. 4** showed the effects of extraction repeated cycles and solid-solvent ratio on the determination of TC in rapeseed. The maximum TC was obtained with the extraction repeated cycles at three times and solid-solvent ratio with 1:30.

**Fig. 5** illustrated the effects of extraction repeated cycles and extraction temperature on the determination of TC in rapeseed. The maximum TC was obtained with extraction repeated cycles locating at three times and extraction temperature locating between 40°C and 45°C.

**Fig. 6** listed the effects of solid-solvent ratio and extraction temperature on the determination of TC in rapeseed. The maximum TC was obtained with solid- solvent ration locating at 1:29 and extraction temperature locating between 40°C and 45°C.

From the shape of contour plots (**Figs. 1−6**), the interaction strength as well as the optimal values range of the independent variables could be observed. Therefore the contour plots are generally the graphical representation of the regression equation for the optimization of extraction conditions for TC extraction from rapeseed.

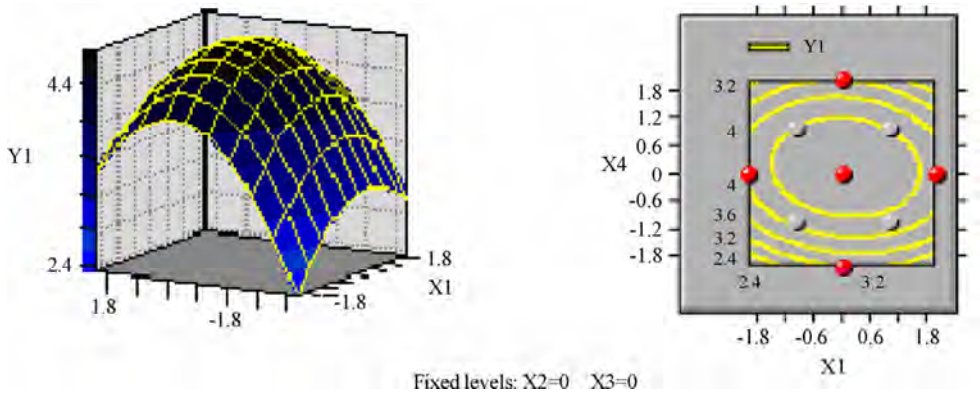


($X_1$: extraction duration/h; $X_4$: extraction temperature/°C; $Y_1$: TC yield/(mg/100g))

**Figure 3.** Combined effects of extraction duration and extraction temperature on TC yield.

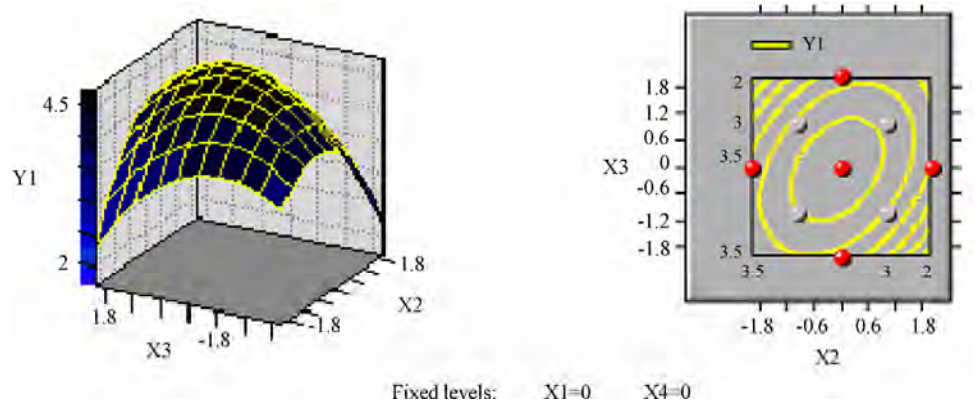


($X_2$: repeated cycle;$X_3$: solid-solvent ratio/(g/mL); $Y_1$: TC yield/(mg/100g))

**Figure 4.** Combined effects of repeated cycles and solid-solvent ratio on TC yield.

 

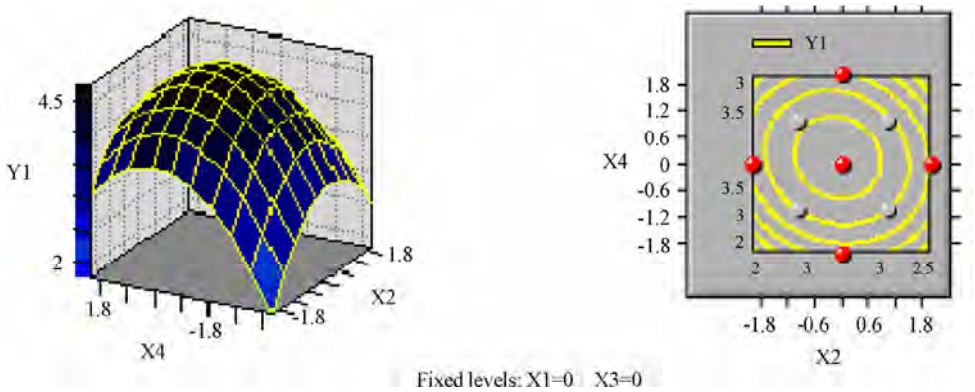


($X_2$: repeated cycle; $X_4$: temperature/°C; $Y_1$: TC yield/(mg/100g))

**Figure 5.** Combined effects of repeated cycle and temperature on TC yield.

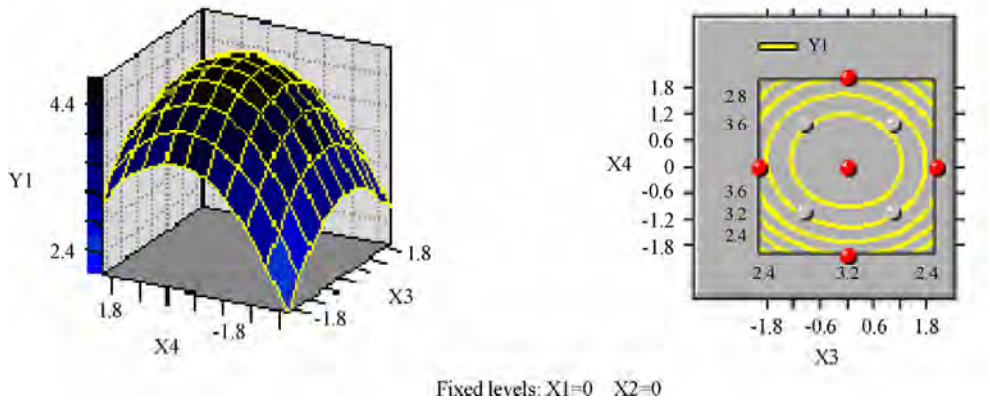


($X_3$: solid-solvent ratio/(g/mL); X4: temperature/°C; $Y_1$: TC yield/(mg/100g))

**Figure 6.** Combined effects of solid-solvent ratio and temperature on TC yield.

### 3.3. Verification of the Model

The optimal parameters for TC extraction from rapeseed were evaluated by RSM and a maximal TC yield of 4.791 mg/100g could be achieved at the optimal conditions: extraction duration 7.3h，repeated cycles 3rd, solid-solvent ratio 1:29, extraction temperature 42°C. The accuracy of the model was validated with triplicate experiments. The experimental value of TC yield was 4.77 ± 0.02mg/100g, which agreed well with the predicted value (4.79 mg/100g), which relative error between experimental value and predicted value was 0.42 ± 0.04%. The verification studies proved that the predicted value of TC for the model could be realistically achieved within a 95% confidence interval of experimental values. Therefore, the model from central composition design was considered to be accurate and reliable for predicting TC yield extraction from rapeseed.

## 4. CONCLUSIONS

Response surface method was proved to be a powerful tool for the optimization of extraction conditions for TC extraction from rapeseed. The conditions were optimized using a five-level-four-factor central composite design. Under optimal conditions (duration 7.3h，repeated cycle 3rd, solid-solvent ratio 1:29, extraction temperature 42°C), the value of the yield of carotenoids was 4.79mg /100g. Validation experiments were also carried out to verify the availability and the accuracy of the model, and the result showed that the predicted value was in well agreement with the experimental value.

## ACKNOWLEDGEMENT

The authors are very thankful for Dr. Lin Qinxiong for providing UV-visible spectrophotometer in the experiments.

## REFERENCES

[1] Holden, J. M., Eldridge, A. L. and Beeeher, G. R. (1999) Carotenoid content of U.S. food: An update of the database. Journal of Food Composition and Analysis, **12(3)**, 169−196.

[2] Sotirios, K. and Vassiliki, O. (2006) Antioxidant properties of natural carotenoid extracts against the AAPH-initiated oxidation of food emulsions. Innovative Food Science and Emerging Technologies, **7(1)**, 132−139.

 

[3] Jamal, J. and Chieri, K. (2006) Variation of lycopene, antioxidant activity, total soluble solids and weight loss of tomato during post harvest storage. Post harvest Biology and Technology, **41(2)**, 151−155.

[4] Rao, A. V. and Rao, L. G. (2007) Carotenoids and human health. Pharmacological Research, **55(3)**, 207−216.

[5] Meléndez-Martínez, A. J., George, B. and Isabel, M. V. (2007) Relationship between the colour and the chemical structure of carotenoid pigments. Food Chemistry, **101(3)**, 1145−1150.

[6] Meléndez-Martínez, A. J., Vicario, I. M. and Heredia, F. J. (2007) Review: Analysis of carotenoids in orange juice. Journal of Food Composition and Analysis, **20(7)**, 638−649.

[7] Andrew, J. and Young, G. M. (2001) Antioxidant and prooxidant properties of carotenoids. Archives of Biochemistry and Biophysics, **385(1)**, 20−27.

[8] Adetayo, O. O. and Aluko, R. E. (2005) The anti-carcinogenic and anti-atherogenic effects of lycopene: A review. Trends Food Sci. Technol., **16(8)**, 344−350.

[9] Cano, A., Acosta, M. and Arnao, M. B. (2003) Hydrophilic and lipophilic antioxidant activity changes during on-vine ripening of tomatoes (Lycopersicon esculentum Mill). Post-harvest Biol. Technol., **28(1)**, 59−65.

[10] Akhtar, M. H. and Bryan, M. (2008) Extraction and quantification of major carotenoids in processed foods and supplements by liquid chromatography. Food Chemistry, **111(1)**, 255−261.

[11] Meléndez-Martínez, A. J., Vicario, I. M. and Heredia, F. J. (2007) Provitamin A, carotenoids and ascorbic acid contents of the different types of orange juices marketed in Spain. Food Chemistry, **101(1)**, 177−184.

[12] Gua, Z. X., Chen, D. M., Han, Y. B., Chen, Z. G. and Gu, F. R. (2008) Optimization of carotenoids extraction from Rhodobacter sphaeroides. LWT-Food Science and Technology, **41(6)**, 1082−1088.

[13] FAO (2006) Statistical year book. Food and Agriculture Organization of the United Nations, **2/1,2/2**, Rome.

[14] Haila, H. and Heinonen, M. (1994) Action of β-carotene on purified rapeseed oil during light storage. Food Science and Technology, **27(6)**, 573−577.

[15] Hornero-Méndez, D. and Mínguez-Mosquera, M. I. (2007) Bioaccessibility of carotenes from carrots: Effect of cooking and addition of oil. Innovative Food Science & Emerging Technologies, **8(3)**, 407−412.

[16] Rodriguez-Amaya, D. B., Kimura, M., Godoy, H. T., and Amaya-Farfan, J. (2008) Updated Brazilian database on food carotenoids: Factors affecting carotenoid composition. Journal of Food Composition and Analysis, **21(6)**, 445−463.

[17] Simkin, A. J., Moreau, H., Kuntz, M., Pagny, G., Chenwei, L., Tanksley, Se., and McCarthy, J. (2008) An investigation of carotenoid biosynthesis in Coffea canephora and Coffea Arabica. Journal of Plant Physiology, **165(10)**, 1087−1106.

[18] Sachindra, N. M. and Mahendrakar, N. S. (2005) Process optimization for extraction of carotenoids from shrimp waste with vegetable oils. Bioresource Technology, **96(10)**, 1195−1200.

[19] Sheetal, M. C. and Laxmi (2007) Enzyme aided extraction of lycopene from tomato tissues. Food Chemistry, **102(1)**, 77−81.

[20] Huang, W., Li, Z. S., Niu, H., Li, D. and Zhang, J. (2008) Optimization of operating parameters for supercritical carbon dioxide extraction of lycopene by response surface methodology. Journal of Food Engineering, **89(3)**, 298−302.

[21] Mateose, R. and Garcia-Mesa, J. A. (2006) Rapid and quantitative extraction method for the determination of chlorophylls and carotenoids in olive oil by high-performance liquid chromatography. Analytical and Bioanalytical chemistry, **385(7)**, 1247−1254.

[22] Rodriguez-Amaya, D. B. (2001) A guide to carotenoid analysis in foods. Washington, DC.: Ed. ILSI-International Life Sciences Institute.

[23] Schoefs, B. (2002) Chlorophyll and carotenoid analysis in food products. Properties of the pigments and methods of analysis. Trends in Food Science and Technolog., **13(11)**, 361−371.

 

**Natural Science, 2009, 1, 30-36** **NS**

# Study of daily solar Irradiance forecast based on chaos optimization neural networks

**Shuang-Hua Cao[1*], Jian-Bo Chen[1], Wen-Bing Weng[1], Jia-Cong Cao[2]**

[1]College of Urban Construction & Environment Engineering, University of Shanghai for Sci. & Tec., Box 484, 516 Jun Gong Rd., Shanghai 200093, China, Tel.: +86 21 55270275, Fax: +86 21 55270686; [2]College of Environmental Science & Engineering, Donghua University, Shanghai 201620, China.
E-mail: [*]canoo@usst.edu.cn

Received 10 May 2009; revised 20 May 2009; accepted 26 May 2009.

## ABSTRACT

**In this works, artificial neural network is combined with wavelet analysis for the forecast of solar irradiance. This method is characteristic of the preprocessing of sample data using wavelet transformation for the forecast, i.e., the data sequence of solar irradiance as the sample is first mapped into several time-frequency domains, and then a chaos optimization neural network is established for each domain. The forecasted solar irradiance is exactly the algebraic sum of all the forecasted components obtained by the respective networks, which correspond respectively the time-frequency domains. On the basis of combination of chaos optimization neural network and wavelet analysis, a model is developed for more accurate forecasts of solar irradiance. An example of the forecast of daily solar irradiance is presented in the paper, the historical daily records of solar irradiance in Shanghai constituting the data sample. The results of the example show that the accuracy of the method is more satisfactory than that of the methods reported before.**

**Keywords:** Daily Solar Irradiance Forecast; Wavelet Transformation; Chaos Optimization Neural Networks

## 1. INTRODUCTION

The environmental conditions are an important factor in the performance of any photovoltaic module, PVM and in other fields, such as, air conditioning, the heating. An accurate measurement of effective irradiance level, Ei is needed to improve the design of PV power systems and maximum power point tracking, MPPT algorithms. And solar irradiance in moderate climates is mostly characterized by short time fluctuations [1,2]. Obviously, it is necessary to carry out an investigation in the forecast of solar irradiance.

There have been many researchers engaged in the modeling of solar irradiance. The existing models established by classical approaches include, e.g., those called clear-day solar radiation, half-sine, Colares-Pereirs & Rabl, and ARIMA hourly solar irradiance [3,4,5]. In fact, it is rather difficult to forecast accurately the behavior of solar irradiance by the traditional models, because they need the bases of the precise definition of problem domains as well as the identification of mathematical functions, but it is very difficult to define and identify precisely when systems are non-linear and there are parameters varying with time due to many factors. The control program often lacks the capability to adapt to the parameter changes. This is just the reason why most existing models were found with relatively big errors and sometimes difficult to use widely. With special abilities in simulating and mapping complicate systems automatically, neural networks are used to learn the behavior of solar irradiance and are subsequently used to simulate and predict this behavior [6].

The heat effect of solar radiation is an all-in effect of the whole solar spectrum, whereas the heat spectrum of solar radiation is uneven and has some difference from solar energy spectrum. It is also different in the influence of the atmospheric conditions and other environmental factors on the sunlight in different frequencies. Naturally, the observed data of solar radiation on earth reflects the difference in these influences. It is proved that the accuracy of a forecasting model could be improved remarkably if preprocessing of sample data is carried out properly. In the paper this task is performed by wavelet transforming, i.e., first to decompose the sample data sequence of solar irradiance into several components of various time-frequency domains according to wavelet analysis, then to use the chaos optimization neural networks (CONNs) particular established to make forecasts for all domains based on these components, finally to make the algebraic sum of the forecasts. Thus a relatively accurate forecast of solar irradiance could be achieved in this way. This is the basis of modeling the

forecast of solar irradiance by means of the combination of artificial neural networks with wavelet analysis.

## 2. WAVELET ANALYSIS OF SOLAR IRRADIANCE

The sun radiates thermal energy to the earth through a wide spectrum from infrared to ultraviolet. The radiation flux onto the earth surface is affected by various factors such as air mass, clouds, and other environmental conditions of earth. The influence is different according to various frequencies of sunlight. Wavelet transformation is an analyzing method of time-frequency localization with fixed area window size and with changeable time-windows and frequency-windows [2,7,8,9]. The components of solar irradiance corresponding to various time-frequency domains can be obtained through mapping the solar irradiance into these domains by wavelet transformation, and then to transform back to the components of various frequency domains. Better understanding of solar irradiance may be obtained through the analyses of these components, and this is just a precondition for more accurate forecast of solar irradiance.

Suppose that a mother wavelet $\psi(t)$ was chosen, a series of wavelet $\psi_{j,k}(t)$ can be developed through dilating and translating the $\psi(t)$. In computer practices the $\psi_{j,k}(t)$ can be obtained as follows, discrete sequence of wavelet being used as a rule.

$$\begin{aligned}\psi_{j,k}(t) &= A^{-j/2}\psi\left(\frac{t-kA^jB}{A^j}\right)\\ &= A^{-j/2}\psi(A^{-j}t-kB)\end{aligned} \tag{1}$$

where $t$ denotes discrete time, and $A^j$ is the scale factor, and $kA^jB$ for translation. **Eq.1** becomes the series of binary wavelets when $A$=2 and $B$=1.

Suppose that $\varphi(t)$ is a scale-function corresponding to $\psi(t)$, then the series of binary scale-functions $\varphi_{j,k}(t)$ can be expressed as:

$$\varphi_{j,k}(t) = 2^{-j/2}\varphi(2^{-j/2}t-k) \tag{2}$$

If $\{f(t), t = 0, \pm1, \pm2, \ldots\}$denotes a data sequence of solar irradiance, and $\{\varphi_{0,k}\}$ is a fundamental orthogonal canonical set in a square-integrable space, and the factors $C_{j,k}$ and $D_{j,k}$ being defined as below

$$\begin{aligned}C_{j,k} &= \int_R f(t)\overline{\varphi}_{j,k}(t)dt\\ D_{j,k} &= \int_R f(t)\overline{\psi}_{j,k}(t)dt\end{aligned} \tag{3}$$

where "-" upon a symbol of a function indicates the complex conjugate of the function, it follows according to the theory of multi-resolution analysis that

$$\begin{aligned}f(t) &= \sum_k C_{0,k}\varphi_{0,k}(t)\\ &= \sum_k C_{1,k}\varphi_{1,k}(t)+\sum_k D_{1,k}\psi_{1,k}(t)\\ &= \sum_k C_{j,k}\varphi_{j,k}(t)+\sum_k D_{j,k}\psi_{j,k}(t)\\ &\quad +\sum_k D_{j-1,k}\psi_{j-1,k}(t)+\cdots+\sum_k D_{1,k}\psi_{1,k}(t)\end{aligned} \tag{4}$$

By using Mallat's pyramid algorithm, the factors in **Eq.4** can be calculated forward-or backward- recursively according to **Eq.5** or 6 respectively.

Mallat's decomposition:

$$\begin{aligned}C_{j+1,k} &= \sum_m \bar{h}_{m-2k}C_{j,k}\\ D_{j+1,k} &= \sum_m \bar{g}_{m-2k}D_{j,k}\end{aligned} \tag{5}$$

and Mallat's composition:

$$C_{j,k} = \sum_n h_{m-2n}C_{j+1,n}+\sum_n g_{m-2n}D_{j+1,n} \tag{6}$$

where operators $h_k = \int_R \varphi(t)\overline{\varphi}_{1,k}(t)dt$ and $g_k = \int_R \psi(t)\overline{\varphi}_{1,k}(t)dt$, $R$ being the real number field and $j$, $k$, $m$, $n$ =0, ±1, ±2, ….

The term $\sum_k C_{j,k}\varphi_{j,k}(t)$ in **Eq.4** is the low frequency components $a_j$ of the data sequence of solar irradiance, and the term $\sum_k D_{j,k}\psi_{j,k}(t)$ represents the high frequency components $d_j$ of the data sequence. The footnote $j$ indicates the $j$-th time-step ($j$=1,2,…, N).

Mallat's pyramid algorithm of wavelet is such a process that carries out the successive decomposition step by step, which looks like a pyramid, through repeatedly using Mallat's algorithm to decompose the low frequency components produced by the Mallat's composition in the previous step. A low frequency sequence $a_N$ and high frequency sequences $d_1$, $d_2$, …, $d_N$ can be obtained when N time-steps of pyramid decomposition of data sequence of solar irradiance have been completed (see **Fig. 1**). Thus the data sequence $f(t)$ can be wavelet-transformed after N time-steps (expressed in **Eq.7**).

$$f(t) = d_1 + d_2 + \cdots + d_N + a_N \tag{7}$$

## 3. MODEL OF CHAOS OPTIMIZATION NEURAL NETWORK FOR SOLAR IRRADIANCE

The behavior of solar irradiance is complex: either periodic or random, and the wavelet-transformed frequency components corresponding to various time-frequency

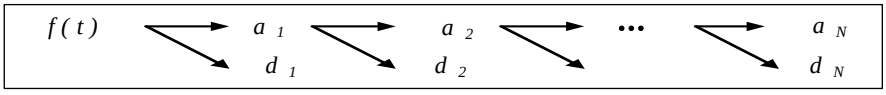


**Figure 1.** The pyramid decomposing process of the data sequence.

 

domains of solar irradiance have similar behavior. In consideration of these special characteristics, the chaos optimization neural network (CONN) is adopted in this work. The algorithm of chaos optimization neural network combines the advantages of gradient descent method and chaos optimization to improve the optimizing search efficiency. The main opinion is: First, to search the local optimum point $\mathbf{s}^*_{\mathbf{old}}$ of former numbers of $N_1$ and the local optimum point $\mathbf{s}^*$ of the latter numbers of $N_1$; secondly, to compare $\mathbf{s}^*$ with $\mathbf{s}^*_{\mathbf{old}}$, when $\left\|\mathbf{s}^*_{\mathbf{old}}-\mathbf{s}^*\right\|>\varepsilon$, then to make linear search find the better optimum point $\mathbf{s}^0$ from $\mathbf{s}^*$ along the direction of $\mathbf{P}=\mathbf{s}^*-\mathbf{s}^*_{old}$; finally to continue the procedure using $\mathbf{s}^0$ instead of $\mathbf{s}^*$ [10].

### 3.1. Model of Chaos Optimization Neural Networks

The structure of the CONN with one hidden layer can be expressed as **Figure 2**, when vector X={$x_1$, $x_2$, …, $x_{n1}$} supplied to input layer, the hidden layer produces vector M={$m_1$, $m_2$, …, $m_{n2}$}, and the output layer sends out vector Y={$y_1$, $y_2$, …, $y_{n3}$}, where n1, n2 and n3 are the neuron numbers of the input, hidden, and output layers of the network respectively.

The weight matrix between input layer and the hidden is {$\mathbf{W}_{ij}$}, and the weight matrix between hidden layer and the output is {$\mathbf{T}_{pi}$}. The biases of hidden layer is $\boldsymbol{\theta}_i$ (i= 1, 2, 3, …, $n_2$), and that of output layer is $\boldsymbol{\theta}_p$ (i=1, 2, 3,…, $n_3$). Suppose {$\mathbf{t}_p$} denotes the expected output vector, the functions of CONN algorithm can be shown as follows:

Output of neurons of hidden layer is:

$$\mathbf{M}_i = f(\sum_j \mathbf{W}_{ij}\mathbf{X}_j - \boldsymbol{\theta}_i) \tag{8}$$

where the activation function in **Eq.8** and in what follows takes the Sigmoid function, that is:

$$f(\mathbf{s}) = \frac{2}{1+e^{-\mathbf{s}}} - 1$$

Output of neurons of output layer is:

$$\mathbf{Y}_p = f(\sum_i \mathbf{T}_{pi}\mathbf{M}_i - \boldsymbol{\theta}_p) \tag{9}$$

The output error function of CONN will be calculated from equation (10):

$$\begin{aligned} \mathbf{E} &= \frac{1}{2}\sum_p ((\mathbf{t}_p - \mathbf{Y}_p)^{\lambda_1}(1-\frac{\mathbf{Y}_p}{\mathbf{t}_p})^{\lambda_2})^2 \\ \mathbf{Y}_p &= f(\sum_i \mathbf{T}_{pi}\mathbf{M}_i - \boldsymbol{\theta}_p) \\ \mathbf{M}_i &= f(\sum_j \mathbf{W}_{ij}\mathbf{X}_j - \boldsymbol{\theta}_i) \end{aligned} \tag{10}$$

where the $\lambda_1$, $\lambda_2$ are defined as balance control indexes, and $\lambda_1+\lambda_2=1$, $\lambda_1,\lambda_2 \geqslant 0$. In the early stage of training procedure, updating of weight value is up to the absolute error; and in the final stage, updating of weight and bias value is mainly up to relative error. To achieve this kind of transition, the balance control indexes can be amended according to the following equation (11):

$$\begin{cases} \lambda_1^{(0)}=1,\ \lambda_2^{(0)}=0 \\ \lambda_1^{(k+1)}=0.9\lambda_1^{(k)},\ \lambda_2^{(k+1)}=1-\lambda_1^{(k+1)} \end{cases} \tag{11}$$

where, k is number of iteration.

### 3.2. Chaos Variant Optimization

First chaotic variants of carrier matrix need be chosen, and the logistic model is commonly used for chaotic variants choice, that is:

$$\mathbf{s}^{(k+1)} = \eta\mathbf{s}^{(k)}(1-\mathbf{s}^{(k)}) \tag{12}$$

where, k is number of iteration, and $\eta$ is control parameter. When $\eta=4.0$, the variant ***s*** in **Eq.12** will keep in a state of chaos.

## 4. DATA PREPROCESSING FOR CHAOS OPTIMIZATION NEURAL NETWORK

It is necessary to normalize the data sequence of the frequency components of solar irradiance into the range of [-0.5,0.5] in advance due to the requirements of wavelet decomposition, so as to enhance the adaptability of the neural network. If {$l(t)$; $t$=0, ±1, ±2,…} denotes a data sequence and {$q(t)$; $t$=0, ±1, ±2,…} denotes a normalized data sequence, it follows that:

$$q(t) = \frac{l(t)-\min l(w)}{\max l(w)-\min l(w)} - 0.5 \tag{13}$$

The normalized data sequence can be restored through **Eq.14**.

$$\begin{aligned} l(t) &= \min l(w) + \\ &\quad [\max l(w)-\min l(w)][q(t)+0.5] \end{aligned} \tag{14}$$

where. $w \in \{t|t=0, \pm1, \pm2, \ldots\}$.

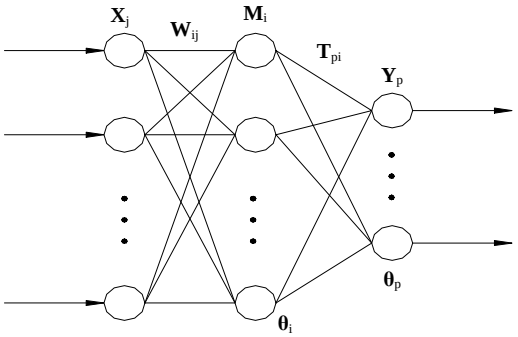


**Figure 2.** The structure of the CONN with one hidden layer.

## 5. IMPLEMENTATION OF THE ALGORITHM OF CONN FOR SOLAR IRRADIANCE

Suppose $\{q(t);\ t = 0, \pm1, \pm2, \ldots\}$ denotes a normalized and decomposed data sequence of solar irradiance. If $\tau$ denotes the day to be forecasted in a time-step of network training and $\{q(\tau\text{-}1),\ q(\tau\text{-}2),\ \ldots,\ q(\tau\text{-}p)\}$ ($p$ equals the neuron number of the input layer of neural networks) is selected from sequence $\{q(t);\ t = 0, \pm1, \pm2, \ldots\}$ as input vector $\boldsymbol{X}\{x_1, x_2, \ldots, x_p\}$ of the CONN, then the output $\boldsymbol{Y}\{y=q'(\tau)\}$ of the CONN is the forecast of daily irradiance of the expected day $\tau$. The structure of the CONN for forecasting solar irradiance is shown as **Fig. 3**.

Suppose that $\boldsymbol{E}$, $\boldsymbol{W}$, and $\boldsymbol{\theta}$ denote the error function, the weights of the network, and the biases respectively, $\boldsymbol{ZW}$, $\boldsymbol{Z\theta}$ denote the carrier matrix of $\boldsymbol{W}$, $\boldsymbol{\theta}$. According to **Eq.12**, the carrier matrix can readily be calculated as follows.

$$\begin{cases} \mathbf{ZW}^{(k)} = 4\mathbf{ZW}^{(k-1)}(1-\mathbf{ZW}^{(k-1)}) \\ \mathbf{Z\theta}^{(k)} = 4\mathbf{Z\theta}^{(k-1)}(1-\mathbf{Z\theta}^{(k-1)}) \end{cases} \tag{15}$$

where, k=1, 2, 3,…, $N_1$.

The weights and the biases will be calculated from **Eq.16**:

$$\begin{cases} \mathbf{W}^{(\kappa)} = 2\mathbf{ZW}^{(\kappa)} - 1 \\ \boldsymbol{\theta}^{(\kappa)} = 2\mathbf{Z\theta}^{(\kappa)} - 1 \end{cases} \tag{16}$$

Then the error function is obtained with **Eq.17**:

$$\begin{aligned} &E(\mathbf{W}^{'}) = \min\left\{E(\mathbf{W}^{*} + a\mathbf{P}) \mid \mathbf{W}^{*} + \lambda_3\mathbf{P} \in R\right\} \\ &\mathbf{W}^{*}_{old} = \mathbf{W}^{'}, \quad \mathbf{W}^{*} = \mathbf{W}^{'}, \quad E^{*} = E(\mathbf{W}^{'}) \end{aligned} \tag{17}$$

where $\lambda_3$ is searching step length, and $\lambda_3 \in [0,1]$.

## 6. AN EXAMPLE OF FORECASTING SOLAR IRRADIANCE

As an example, a forecast of daily solar irradiance using CONN with wavelet analysis was carried out based on the data sequence of the daily records of irradiance by Baosan Meteorological Station in Shanghai from 1995 to 2000, i.e., the records amounting to 365×6+2=2192 days' (note: the loop years of 1996 and 2000). **Fig. 5** shows the historical daily solar irradiance of the 2192 days. The computer programming is based on Matlab6.5. DB7, the No.7 of Daubechies wavelet functions, was chosen to be the mother wavelet.

Using Mallat's pyramid method with the mother wavelet of DB7, the low frequency sequence of $a_3$ and the high frequency sequences of $d_3$, $d_2$, and $d_1$ of the daily solar irradiance could be obtained (see **Fig. 6**) by the 3-scale wavelet decomposition. The algebraic sum of the low frequency sequence and the high frequency sequences equals the original data sequence. Then normalize $a_3$, and $d_3$, $d_2$, $d_1$. The normalized sequences $a_3$, and $d_3$, $d_2$, $d_1$ are to be used as 4 training data sets.

A 3-layer CONN is constructed in the following way. The input layer has 9 neurons for the input of 9 sample records corresponding to 9 successive days just before the day being forecasted in training. The number of neurons for the hidden layer is also determined to be 4 using the trial and error method. The output layer has only one neuron for outputting the forecast results, i.e. the data corresponding to the 10th day when in training.

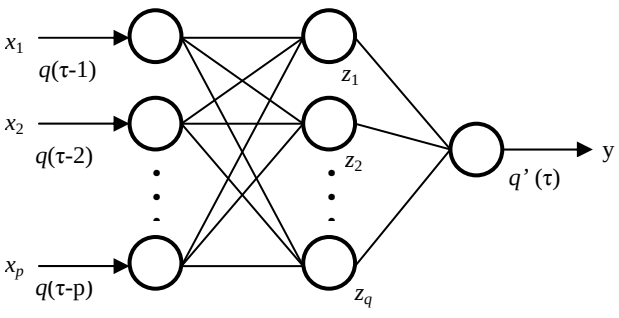


**Figure 3.** The structure of the CONN for forecasting solar irradiance.

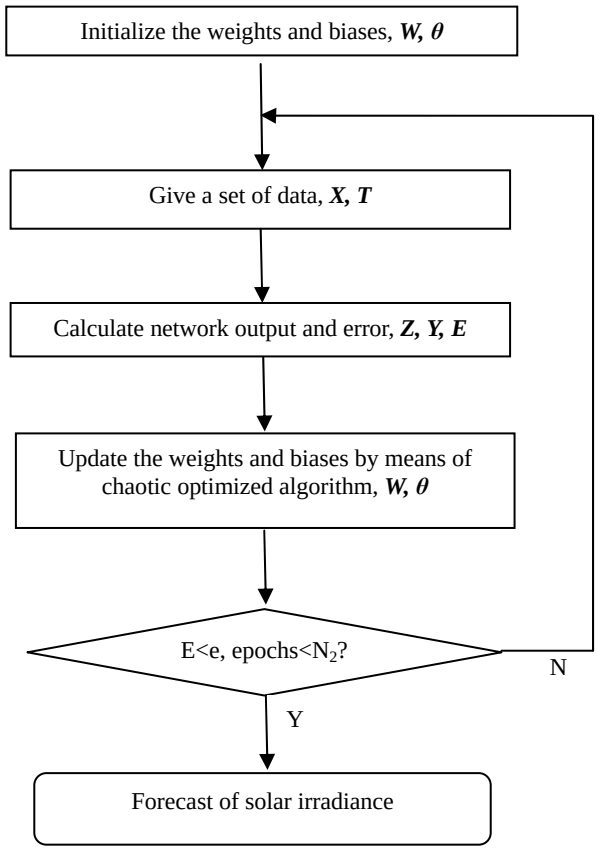


**Figure 4.** Flowchart of CONN for solar irradiance.

So the CONN could be trained in the following way using the sequence of the low frequency of $a_3$, which has 1826 records decomposed from the irradiance sequence of 1826 days during years of 1995 to 1999.

For the first iteration, the CONN takes the first successive 10 data as the first group from sequence $a_3$ that includes 1826 data, and then uses the first 9 data of the group as the input $\boldsymbol{X}_1 = \{x_1, x_2, \ldots, x_9\}$ of the network to get an output $y_1$. The error $\boldsymbol{E}_1$ of $y_1$ is calculated by comparing $y_1$ with the 10th datum of the group, and the $\boldsymbol{ZW}_1$ and $\boldsymbol{Z\theta}_1$ are calculated by **Eq.15** as well. Then the updating of the weights and biases of CONN could be performed using **Eq.16**. The training of the network continues when successively taking the data patterns in such a way that for the second iteration the group is composed by the 2nd to 11th data of the 1826 data, and for the next iteration the group is composed by the 3rd to 12th data, and so on. The procedures circulate from the beginning when all the 1826 data of sequence $a_3$ has been in processing, and do not stop until any of stop conditions is reached. **Table 1** shows the way to divide sequence $a_3$ into 1818 data groups.

**Table 1.** Grouping of sequence $a_3$ for training.

| Group No. | Input vector, $\boldsymbol{X}$ | Expected outputs, $\boldsymbol{T}$ |
|---|---|---|
| 1 | $a_3(1)$, $a_3(2)$, …, $a_3(9)$ | $a_3(10)$ |
| 2 | $a_3(2)$, $a_3(3)$, …, $a_3(10)$ | $a_3(11)$ |
| … | … | … |
| 1817 | $a_3(1817)$, $a_3(1819)$, …, $a_3(1825)$ | $a_3(1826)$ |

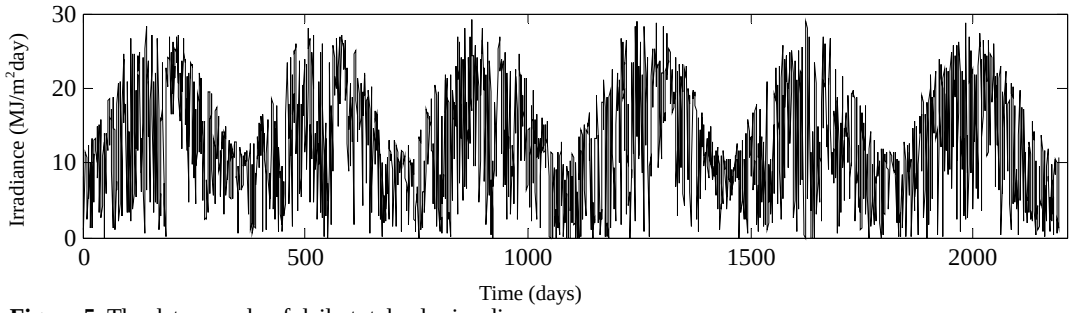


**Figure 5.** The data sample of daily total solar irradiance.

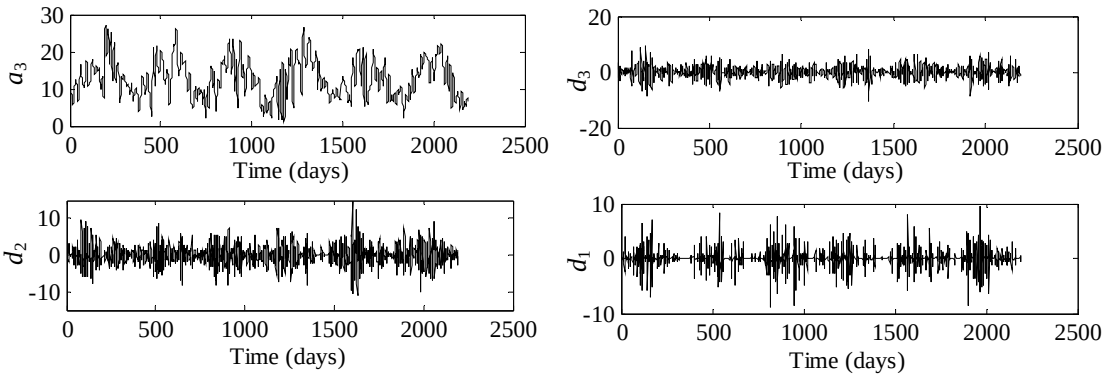


*the units of ordinates: MJ/m²day

**Figure 6.** The wavelet-decomposed sequences of data sample of solar irradiance.

**Table 2.** Errors of CONN training and forecasting.

| Data sequences | | Errors of training | | | Errors of forecasting | | |
|---|---|---|---|---|---|---|---|
| | | RMSE (MJ/m²day) | MAE (MJ/m²day) | MRE (%) | RMSE (MJ/m²day) | MAE (MJ/m²day) | MRE (%) |
| with wavelet analysis: | of low frequency sequence | 0.4134 | 0.3117 | 3.52 | 0.3109 | 0.2649 | 3.25 |
| | of total daily irradiance | 0.8156 | 0.6084 | 8.47 | 0.8373 | 0.6446 | 7.71 |
| without wavelet analysis: | of total daily irradiance | 3.3367 | 2.5649 | 40.71 | 4.1879 | 2.5649 | 41.47 |

 

The similar procedures to that described in above 3 paragraphs are carried out with other 3 CONNs, which are constructed in the same way as that for sequence $a_3$, for the high frequency sequences of $d_3$, $d_2$, and $d_1$ respectively, each of $d_3$, $d_2$, and $d_1$ having a training data set with 1826 records.

In the training, the initial values of $\lambda_1$, $\lambda_2$ were fixed on 1 and 0 respectively, The stop conditions were the limitation of training error, which was 0.01, and the maximum training times (preset to 8000), i.e., all the 1817 data patterns would undergo training-cycles at most for 8000 times or, in other words, an epoch had completed. After the epoch was completed totally, the CONNs could be used to forecast the 366 data of the daily solar irradiance of year 2000, which could be compared with the historically recorded data of 2000 in the data sample. For the sake of saving the space of the paper, only **Figs. 7.1-7.4** are presented for the network training and component forecasting based on the low frequency sequence of $a_3$, while saving those based on sequences of $d_3$, $d_2$, and $d_1$. The forecasting errors for sequence $a_3$, including the root-mean-square errors (RMSE), the mean absolute errors (MAE), and the mean relative errors (MRE), are also listed in **Table 2**.

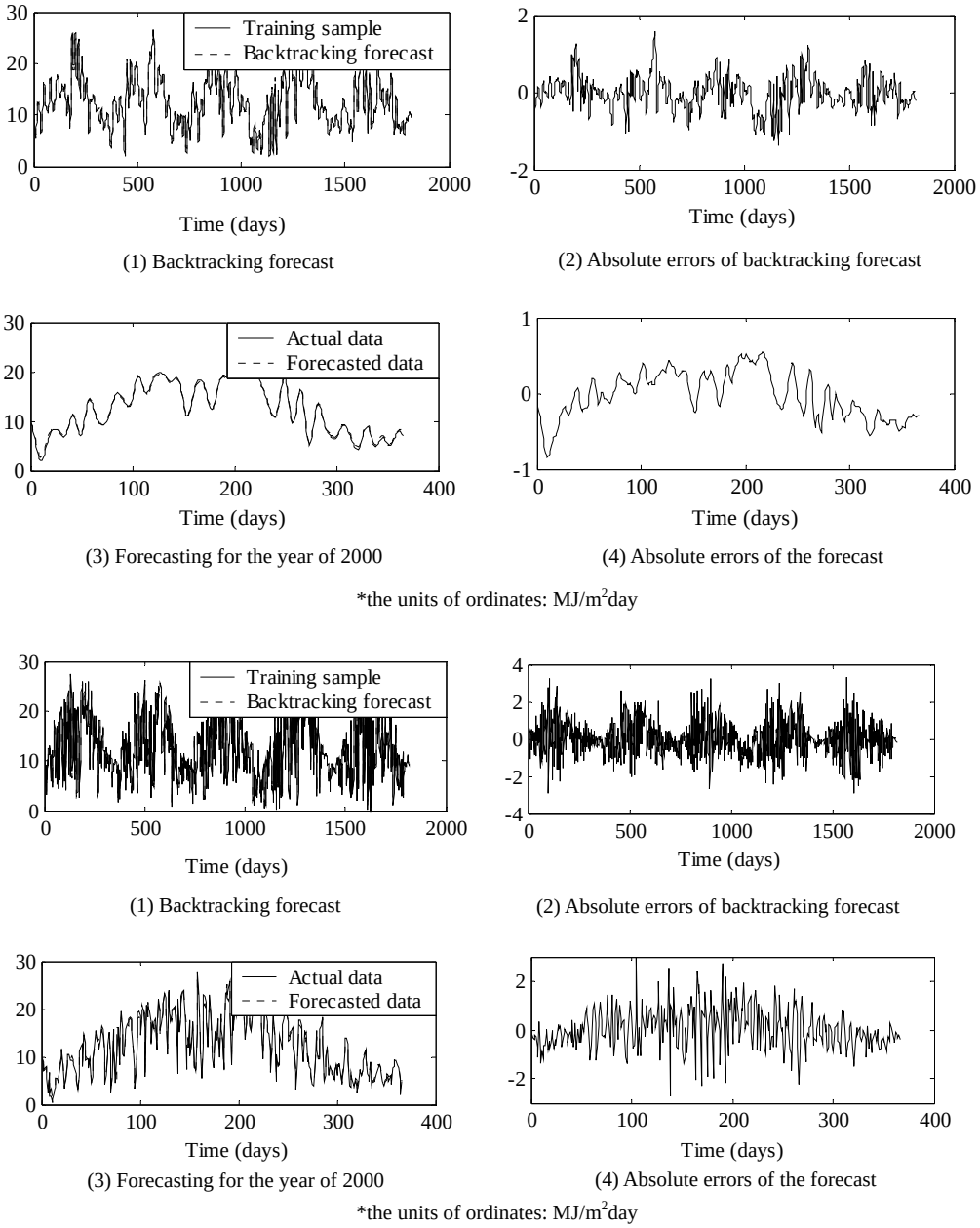


**Figure 8.** Training and forecasting of day-by-day total solar irradiance.

**Fig. 8** shows the results of the algebraic sum of the forecasted low frequency sequence of $a_3$ and the forecasted high frequency sequences of $d_3$, $d_2$, and $d_1$, i.e., the backtracking forecasted total daily irradiance in the period of 1995 to 1999 (**Fig. 8.1**) and the forecasted total day-by-day irradiance in year 2000 (**Fig. 8.3**). The errors are also listed in **Table 2**.

In order to have an example to compare with, a CONN with the same structure was also used to forecast the daily solar irradiance of the same period of time under the condition that the sample data were not handled by wavelet analysis. And the maximum training times was assigned to 10000 for this CONN. The other factors were the same as those assigned in the previous paragraphs. The errors of training and forecasting are also listed in **Table 2**.

## 7. DISCUSSIONS AND CONCLUSIONS

The forecast method that is presented and applied to forecasting solar irradiance in the paper combines chaos optimization neural network with wavelet transformation, and proves remarkable improvement through an example in the accuracy of the forecast for the daily solar irradiance of a year compared with that without combining wavelet transformation. The example of solar irradiance shows that the RMSEs of the training and the forecast with wavelet analysis are 0.8156 MJ/m$^2$ day and 0.8373 MJ/m$^2$·day respectively. The MRE of the forecast with wavelet analysis accounts for 7.71%, which is about one fourth of the forecast without wavelet analysis. It is obvious that the forecasted irradiance curve is well identical to the actual one (see **Fig. 8**).

Because the method presented does not depend upon the intrinsic properties of the sequence of sample data, the principle of this work could be applicable to some other fields such as load forecast, pattern recognition, etc.

There are various tasks which can be used to study further the combination of neural network and wavelet transformation, e.g., the more detailed analysis of the special behavior of the objects to be forecasted, the optimal combination of wavelet analysis and neural network, the selection of mother wavelet, the optimal updating of weights and biases, etc. The accuracy of this method may be further improved after progress has been made in these tasks.

## ACKNOWLEDGEMENTS

The work described in this paper was sponsored by leading academic discipline project of shanghai municipal education commission, China (Project No. J50502) and innovation action programme project of science and technology commission of shanghai municipality, China (Project No. 08DZ1203802).

## REFERENCES

[1] Woyte, A., Belmans, R. and Nijs, J. (2003) Analysing short-time irradiance fluctions by their characteristic time scales. Proc. of 3rd World Conf. on Photovoltaic Energy Conversion, 2290−2293.

[2] Ortiz, R. E. I. and Peng F. Z. (2006) Algorithms to estimate the temperature and effective irradiance level over a photovoltaic module using the fixed point theorem. Power Electronics Specialists Conference, PESC'06, 37th IEEE, 1–4.

[3] Li, J. and Song, A. G. (1998) Comparison of clear-day solar radiation model in Beijing to ASHRAE model. Journal of Capital Normal University, **19(1)**, pp. 35−38.

[4] Ren, M. J. and Wright, J. A. (2002) Adaptive diurnal prediction of ambient dry-bulb temperature and solar radiation. HVAC and Research, **8(4)**, 383−401.

[5] Zhang, S. N. and Tian, S. Y. (2007) Setup of the hourly solar irradiance model. Journal of Solar Energy, **18(3)**, 273−277, 1997.

[6] Kalogirou, S. A. (2001) Artificial neural networks in renewable energy systems applications: A review. Renewable and Sustainable Energy Reviews, **5(4)**, 373−401, 2001.

[7] Rioul, O. and Vetterli, M. (1991) Wavelets and signal processing. IEEE SP Magazine, **8(4)**, 14−38.

[8] Chui, C. K. (1992) An introduction to wavelets. Academic Press, New York.

[9] Debnath, L. (2002) Wavelet transforms and their applications. Springer-Verlag Inc., New York.

[10] Chen, L. and Aihara K. (1995) Chaotic simulated annealing by a neural network model with transient chaos. Neural Networks, **8(6)**, 915−930.

 

**Natural Science, 2009, 1, 37-40** **NS**

# Discussion on low-carbon economy and low-carbon building technology

**Xiao-Gen Shuai[1,2], Hui-Qiang Li[2]**

[1]CNNC Hunan Taohuajiang Nuclear Power CO., LTD, Yiyan 413000, P. R. China; [2]School of Civil Engineering and Mechanics, HUST, Wuhan 430074, P. R. China.
Email: shuaixiaogen@smail.hust.edu.cn

Received 11 May 2009; revised 20 May 2009; accepted 26 May 2009.

## ABSTRACT

**The paper introduced low-carbon economy and low-carbon technology, and proposed the detailed technical measures of low-carbon building technology. Moreover, it has quantitatively calculated the "implicit" $CO_2$ emission of C40 and C50 concrete columns, aluminium curtain wall, wall paintings and common floor decoration materials. The calculation results show that it is preferable to use high strength concrete, reduce the usage of aluminium materials and use wooden floor according to location. The paper can be a reference for quantitative measurement to the low-carbon technology and energy efficiency.**

**Keywords:** Low-Carbon Economy; Low-Carbon Technology; Building Technology; Quantitative Calculation

## 1. INTRODUCTION

The British energy white paper "Our Energy Future-Creating a Low Carbon Economy" firstly introduced the concept of "Low-carbon Economy" [1]. This concept means that the developed industrial country should use the production technology that reduces the emission of $CO_2$, so as to protecting the environment while maintaining the economic growth. The $CO_2$ and ozone etc. in the aerosphere can absorb the radiant heat from sun and preventing its escape from the earth, therefore empowering the aerosphere of the natural greenhouse effect. When the density of greenhouse gases such as $CO_2$ raises, the absorbed radiant heat will increase and the heat given out by the earth will be reduced, thus resulting in global warming. Global warming will melt the glacier, raise the sea level, reduce the continental area, silt up harbors and destroy the marsh land and river plain, as a result bringing great negative effects to the economic of coastland area. Moreover, global warming will shift the climate zone to high latitude, change the ecosystem in certain area and increase infectious diseases and the consumption of ozonosphere [2].

White paper: China's policies and actions on climate change [3] issued by the Chinese government has indicated that, the average temperature of the earth surface in China has increased by 1.1℃ during the last 100 years. For the last 30 years, the sea level has increased by 90mm on average. For example, the 《Assessment Report on Climate Change of Guangdong》 [4] issued by the weather bureau of Guangdong Province in 2007 forecast that, in the background of global warming, the emission of greenhouse gases such as $CO_2$ will be doubled in Guangdong Province, and the sea level will increase by 30cm (compared with the highest level in record), which is quite serious.

China is one of the first signing countries of 《Kyoto Protocol》, but it has not assumed its responsibility in reducing the emission of gas since it is still a developing country. However, China has a growing power in the economic world, and as a responsible major country China has to face the question of reducing the emission of greenhouse gases and develop a low-carbon economy during its economic growth.

The low-carbon technology has relationships with electricity sector, transportation sector, construction sector, chemistry industry and many other new technologies. Price L. *et al* [5] and Kim Y [6] have studied the energy demand and $CO_2$ emission of Chinese steel industry; and Yang J X [7] have conducted bill analysis over the life cycle of steel industry. Low-carbon building technology is a multi-disciplined subject. Based on the building design and selection of building materials, the paper adopts the life cycle assessment to quantitatively analyze the emission of $CO_2$ and studies the low-carbon building technology, in expecting to provide a brand-new angle for energy saving and green building.

## 2. ENERGY SAVING AND EMISSIONS REDUCTION

Energy saving in buildings relates to building planning, building design, retaining structure, heating system, air-conditioning system design, lighting system and many other sectors [8]. At present, many energy saving methods have been carried out in construction projects, including heat preventing technology in surrounding structure, usage of solar power and wind power, energy saving in temperature control, and enhancing energy saving management; they all have a positive impact on energy saving and emission reduction [9,10,11]. However, the author of this article feels that all these works are "explicit" energy saving and carbon reducing works; for example, the heat preventing technology in surrounding structure puts more attention to the energy saving during the running of buildings. But they have not considered the massive consumption of building materials and energy during the construction of the project, the massive emission of greenhouse gases such as $CO_2$ during the collection, artificial work and transportation process. Low-carbon emission measures should also be taken to them, and these measures can be called "implicit" carbon reducing measures. In this sense, low-carbon building technology should take into consideration of both the "explicit" and "implicit" low-carbon technology.

## 3. LOW-CARBON BUILDING TECHNOLOGY

From the point of low-carbon building technology, it should be taken into consideration of choosing materials and components with lower carbon emission during the designing and construction process.

### 3.1. Low-Carbon Technology in Structure Designing

The paper takes the ground floor structure of a five-story frame structure industrial workshop of a chemical factory as the example. It compares the C40 concrete with the C50 concrete through the PKPM structure designing software, both of which are under the same structure load and seismic designing requirement. And the change in sectional area are shown in **Figure 1**, when C40 has been upgraded to C50 with the same amount of reinforcements; and the length of each side in section has been reduced by 50mm in most of columns.

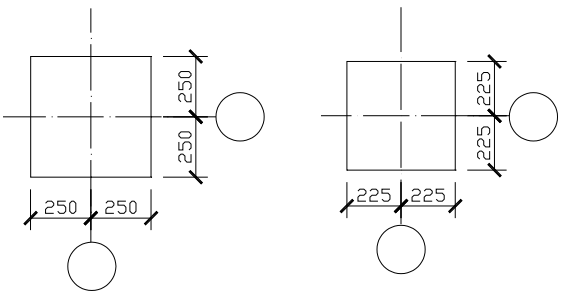


(a) C40 (b) C50

**Figure 1.** Section of concrete columns.

The mixed ratios of concrete used by this article have been listed in **Table 1**. The $CO_2$ emission of concrete production is 1041.6kg $CO_2$/t [12]. According to the investigation of building materials procurement in Wuhan, the transportation distance of concrete used by the concrete batching plant is 50km~200km; which is taken as 100km for the convenience of following calculation. The transportation distance for sand and gravels is 50km, and the distance for concrete from the concrete batching plant to the construction site is 50km; moreover, according to references [13], the energy consumption of sand and gravel is 13.89 kw·h/t, and that of concrete is 2 kw·h/$m^3$. All the materials will be transported by 5 t trucks, and the amount of $CO_2$ emission during the transportation and electricity production is referred to reference [14]. The $CO_2$ emission calculation of 1$m^3$ concrete in using the bill analysis (a type of life cycle assessment method) under the two strength levels have been listed as follows.

Through the calculation, when the columns in ground floor using the C40 concrete, the quantity consumed is 30.996$m^3$, and the $CO_2$ emission is 15994kg; when using the C50 concrete, the quantity consumed is 25.389$m^3$, and the $CO_2$ emission is 15 193kg. The consumption of concrete has been reduced by 5.607$m^3$, or 18.1%; and $CO_2$ consumption has been reduced by 801kg, or 5.0%. In increasing the strength of concrete, the consumption of concrete and $CO_2$ emission can be largely reduced. Therefore, high strength concrete should be preferable, with the satisfaction to structure safety and designing requirement.

**Table 1.** Mixed ratio of concrete.

| Concrete Strength Level | Cement grade | Mixed ratio/(kg/$m^3$) | | | |
|---|---|---|---|---|---|
| | | cement | sand | crushed rock | water |
| C40 | 525 | 460 | 720 | 1080 | 185 |
| C50 | 525 | 540 | 655 | 1070 | 185 |

**Table 2.** $CO_2$ emission of C40 and C50 concrete columns(kg/$m^3$).

| Concrete Strength Level | C40 | C50 |
|---|---|---|
| Cement production | 479.1 | 562.5 |
| Cement transportation | 1.1 | 1.3 |
| Aggregate acquisition | 28.5 | 27.3 |
| Aggregate transportation | 2.1 | 2.1 |
| Concrete mixing | 2.3 | 2.3 |
| Concrete transportation | 2.9 | 2.9 |
| Total | 516.0 | 598.4 |

 

### 3.2 Low-carbon Technology in Building Materials

The building components can be made from various building materials, while the "implicit" $CO_2$ emission differs during the production of different building materials. The paper adopts the BEES assessment software developed by National Institute of Standards and Technology to calculate the "implicit" $CO_2$ impact of different building materials. BEES (Building for Environmental and Economic Sustainability, BEES) is a comprehensive evaluation software over the construction environment and sustainability, and has been supported by the Association of American Environment Protection and U. S. Government [15]. It uses the Life Cycle Assessment (LCA) to quantitatively assess the environmental performance of building materials.

#### 3.2.1. Comparison Between Aluminium Curtain wall and wall Paintings

There are enormous consumption of fossil fuel and $CO_2$ emission in the production process of aluminium materials, and the energy consumption is 435GJ/t while carbon emission is 8700kg/t; but the figures in the production of steel materials are only 35GJ/t and 700kg/t, both of which are 1/12 of that of aluminium materials [16]. Therefore, the usage of aluminium materials should be reduced, and other green materials should be adopted. This article has conducted a calculation over the aluminium curtain wall of a university refectory project, and has analyzed the difference of $CO_2$ emission by switching to common wall paintings.

The "implicit" $CO_2$ emission of $1m^2$ aluminium curtain wall and common wall paintings have been calculated out by BEES software. For the convenience of calculation, it has been assumed that the transportation distance for both of them are 200km with a life span of 50 years, then the quantity of $CO_2$ emission are shown as follows.

As a result, the $CO_2$ emission of aluminium curtain wall is far larger than that of common wall paintings. The quantity of aluminium curtain wall in this refectory project is $2519m^2$, but if using the common wall paintings it will reduce 34476kg $CO_2$ with an 85% reduction rate.

**Table 3.** Comparison between aluminium curtain wall and wall paintings ($gCO_2/m^2$).

| life cycle stage | Raw materials | Manufacturing | Transportation | Total |
|---|---|---|---|---|
| aluminium curtain wall | 14131 | 1878 | 40 | 16050 |
| wall paintings | 1755 | 566 | 42 | 2364 |

**Table 4.** Comparison of floor decoration materials ($gCO_2/m^2$).

| life cycle stage | Raw materials | Manufacturing | Transportation | Total |
|---|---|---|---|---|
| Composite marble tile | 25953 | 334 | 1679 | 27966 |
| Terrazzo flooring | 26878 | 0 | 947 | 27836 |
| Wool carpet tile | 415673 | 2314 | 237 | 418213 |
| Natural cork tile | 6006 | 3262 | 301 | 9580 |

#### 3.2.2. Indoor Floor Decoration Materials

Floor decoration material has been a major part of the total consumption and cost of a decoration project, thus the choices of materials have a close relationship with the "implicit" $CO_2$ emission and indoor environment. This article has selected several common indoor floor decoration materials, and used the BEES software to calculate the "implicit" $CO_2$ emission of $1m^2$ indoor floor decoration materials for 50 years life span. For the convenience of calculation, it has been assumed that, the transportation distance of the material is 400km with a life span of 50 years, then the quantity of their $CO_2$ emission are as follows.

It is obvious to see the advantage of wooden floor in carbon reduction, while other materials have given out much $CO_2$ in their whole life cycle; the animal-made materials have the most serious situation. Therefore, wooden materials should be selected if the local forests can sustainable provide the resources.

## 4. CONCLUSIONS

The paper has discussed the Low-carbon economy and Low-carbon building technology, and has proposed detailed technical measures of Low-carbon building technology. In satisfying the structure load and seismic designing requirements, the "implicit" $CO_2$ emission can be reduced by approximately 5% if replace C40 concrete by C50 concrete; the quantity of $CO_2$ emission of the aluminium alloy curtain wall during the whole life cycle is 15% of that of the wall paintings with the same area; wooden floor has a much smaller quantity of "implicit" $CO_2$ emission than other indoor floor decoration materials. The above measures and calculation results are of value as a reference for energy saving, emission reduction and low-carbon building technology.

## ACKNOWLEDGEMENTS

This work is supported by the Special Research Foundation of Doctoral Subjects in University of China (No. 20050487017).

## REFERENCES

[1] Department of Trade and Industry (2003) Our energy future-creating a low carbon economy. The Stationery Office, London.

 

[2] Chris, H. (2002) Priorities for a low-carbon economy. New Economy, **9(1)**, 11−15.
[3] State council information office of the People's Republic of China (2008) White paper: China's policies and actions on climate change. http://www.chinanews.com.cn/gn/news/2008/10−29/1429538.shtml.
[4] Composing team for Assessment Report on Climate Change of Guangdong (2007) Assessment report on climate change of Guangdong (Selection). Guangdong Meteorology (in Chinese), **29(3)**, 1−7.
[5] Price, L., Sinton, J., Worrell, E., *et al*. (2002) Energy use and carbon dioxide emissions from steel production in China. Energy, **27**, 429−446.
[6] Kim, Y. and Worrell, E. (2002) International comparison of $CO_2$ emission trends in the iron and steel industry. Energy Policy, **30**, 827−838.
[7] Yang, J. X. and Liu, B. J. (2002) Life cycle inventory of steel products in China. Acta Scientiae Circumstantiae (in Chinese), **22(4)**, 519−522.
[8] Long, W. D., Bai, W. and Fan, R. (2008) Low-carbon economy and the development of building energy-saving. Construction Science and Technology (in Chinese), **24**, 15−20.
[9] Sunikka, M. (2006) Energy efficiency and low-carbon technologies in urban renewal. Building Research & Information, **34(6)**, 521−533.
[10] Arena, A. P. and Rosa, C. D. (2003) Life cycle assessment of energy and environmental implications of the implementation of conservation technologies in school building in Mendoza-Argentina. Building and Environmental, **38**, 359−368.
[11] Chris, S., Gregory, A. K. and Peter, R. (2003) Life cycle energy and environmental performance of a new university building: Modeling challenges and design implications. Energy and Buildings, **35**, 1049−1064.
[12] Gong, Z. Q. and Zhang, Z. H. (2004) A study on embodied environmental profile during the life cycle of cement. China Civil Engineering Journal (in Chinese), **37(5)**, 86−91.
[13] Li, S. T. (2007) Study on appraisal model of reducing construction of construction project (in Chinese). Ph. D. thesis, Huazhong University of science and technology, Wuhan, ON, China.
[14] Yang, J. X., Xu, C. and Wang, R. S. (2002) Methodology and application of life cycle assessment (in Chinese). China Meteorological Press, Beijing.
[15] Lippiatt, B. C. (2007) Building for environmental and economic sustainability technical manual and user guide. http://www.bfrl.nist.gov/oae/software/bees/bees.html.
[16] China Building Materials Academy (2003) Green building materials and making building materials green (in Chinese). Chemical Industry Press, Beijing.

 

**Natural Science, 2009, 1, 41-46** **NS**

# A Study of thermal decomposition in cellulose by molecular dynamics simulation

**Chao Liu[1], De-Zheng Jiang[1], Shun-An Wei[2], Jin-Bao Huang[1]**

[1]College of Power Engineering, Chongqing University, Chongqing 400044, China; [2]College of Chemistry and Chemical Engineering, Chongqing University, Chongqing 400044, China.
Email: liuchao@cqu.edu.cn

Received 19 May 2009; revised 5 June 2009; accepted 7 June 2009.

## ABSTRACT

**PM3 method was used in this paper to optimize cellulose molecular structure which is the main component of biomass and a series of structural parameter was attained. The single chain of cellulose (the degree of polymerization is 9) was simulated in different force fields by molecular dynamic method. Energy history, deposition temperature and the cracked groups of simulation process in different force fields was gotten, of which Amber force field is quite matched to the experiments data. By simulating the process of cellulose thermal decomposition with MD which is based on Amber force field and quantum mechanics, we get the sequence of bond break of cellulose molecule and the first cracked group. Also, the first production was analyzed. The heating process includes two stages: vibrate at low temperature and break at high temperature (273k-375k) and breaking stage when the temperature of the system arrived at 375K.**

**Keywords:** Molecular Dynamics Simulation; Cellulose; Thermal Decomposition; Bond Breaks

## 1. INTRODUCTION

The special meeting, green energy: the cooperation of government and enterprise, of Boao Asian Forum pointed out that the miraculous development of Asia will not continue if no appropriate measures were taken to make sure energy safety, decrease energy consuming, find new energy and to release environment stress. However, all the problems probably can be solved by biomass energy, which has become one of the most popular and important topics in the word.

Biomass consists of cellulose, hemicellulose, lignin and a small amount of ash content. Cellulose, which is D-glucose high molecular polymer formed by connection between $\beta$ (1-4)-glycosidic bond, is the main component of biomass, accounting for 40%−96% of the total amount of biomass. Many researches on relation between raw material and production of biomass energy were done by scholars form all over the world, using thermal decomposition, liquefaction, gasification [2,3,4, 5]. However, the work on the process is rare. In order to investigate the further principle of biomass energy's thermal deposition process, a reactive molecular dynamics model was developed to simulation the thermal deposition of cellulose in this paper.

Molecular structures were optimized before molecular dynamic simulation to lower the molecule energy to the possibly lowest degree. The lower the energy is, the steadier the structure is and the higher probability exists in the system is. Single point calculation was applied for optimizing energy; Optimized structure was searched by calculating a series of bond length and bond angle.

Single molecular was employed in this MD simulation, which differs form other poly-molecular systems. The lowest point of partial total potential energy was gotten when searching the lowest total potential energy, but the global optimization was needed. MD method must be used when optimal three dimensional structures were set. Molecules are heated up and the structure extends and relaxes adequately at high temperature. Then we cool down the molecules and calculate the optimum structure. Optimal three dimensional structures can be obtained. The conformations were much different between single molecule and multiple molecules which are more accordant with practical situation. Single molecule was researched in this paper considering huge system, complex structure and the operation ability of computes.

The semi-empirical method MNDO-PM3 based on MNDO model was used in this paper and Polak-Ribiere conjugate gradient was applied in optimization with RMS setted as 0.042kJ/mol. The results of cellulose molecular optimization were listed in **Table 1**.

## 2. SIMULATION TECHNIQUE

### 2.1. Simulation Model

The molecular formula of cellulose is $(C6H10O5)_n$, where n is polymerization degree. Haworth structure is used to express the cellulose molecule in the simulation [6]. The structure model is given in **Fig. 1**.

The simulated object is single chain of cellulose with polymerization degree is 9. The original size is 6.9727 ($\mathring{A}$)×6.2610($\mathring{A}$)×41.3464($\mathring{A}$) after optimizing. The size of the simulation cell is 15($\mathring{A}$)×15($\mathring{A}$)×50($\mathring{A}$). Periodic boundary condition was applied. During the simulation, the temperature was heated up from the 293K at the begging to 1273K which is simulation temperature. The heating time is 100ps; the simulation time is 10ps; the step size is 0.001ps. The parameters of energy and temperature were collected every time step.

**Table 1.** The parameters of cellulose molecule before and after optimizing.

| Parameters / Groups | Before Optimizing | After Optimizing | Parameters / Groups | Before Optimizing | After Optimizing |
|---|---|---|---|---|---|
| $C_1H_1$ | 1.09A | 1.1073A | $O_2H$ | 0.96A | 0.9617A |
| $C_1H_2$ | 1.09A | 1.10458A | $C_3C_4C_5$ | 108.247° | 110.169° |
| $H_1C_1H_2$ | 109.47° | 108.014° | $C_4O_2H$ | 109.471° | 108.112° |
| $C_1O_1$ | 1.43A | 1.40063A | $HC_4O_2H$ | -159.4365° | -159.246° |
| $O_1H_1$ | 0.96 A | 0.96587A | $C_3C_4C_5O_2$ | -119.811° | -127.222° |
| $C_1C_2$ | 1.54A | 1.55006A | $C_3C_4HC_5$ | 119.8° | 120.336° |
| $HO_1C_1$ | 109.471° | 107.203° | $C_5H$ | 1.09A | 1.11574A |
| $HC_1HO_1$ | -120° | -116.391° | $C_5O_3$ | 1.43A | 1.40229A |
| $C_2H$ | 1.09A | 1.11871A | $O_3H$ | 0.96A | 0.95074A |
| $C_2O_4$ | 1.4326A | 1.42258A | $C_5C_6$ | 1.54012A | 1.55571A |
| $C_2C_3$ | 1.54A | 1.54324A | $C_4C_5C_6$ | 108.867° | 112.894° |
| $C_3C_2H$ | 109.325° | 109.75° | $C_5O_3H$ | 109.471° | 107.744° |
| $C_3C_2O_4$ | 110.057° | 115.958° | $C_4C_6C_5H$ | -120.01° | -119.849° |
| $HC_3C_2O_4$ | 120.044° | 111.173° | $C_4C_6C_5O_3$ | 119.99° | 128.836° |
| $HC_3C_2C_1$ | 119.857° | 121.745° | $C_6H$ | 1.09A | 1.12113A |
| $C_3H$ | 1.09A | 1.1336A | $C_6O_5$ | 1.43A | 1.41851A |
| $C_3C_4$ | 1.53748A | 1.5499A | $C_6O_4$ | 1.43285A | 1.39737A |
| $HC_3C_2$ | 109.62° | 109.505° | $C_5C_6O_4$ | 110.052° | 116.06° |
| $C_2C_3C_4$ | 108.875° | 113.707° | $C_5C_6O_5$ | 109.339° | 113.56° |
| $HC_3C_4$ | 109.62° | 109.879° | $C_5C_6O_5H$ | 119.728° | 127.655° |
| $C_4HC_2C_3$ | 38.1592° | 34.3572 | $C_5C_6O_4O_5$ | 120.104° | 123.063° |
| $C_4O_2$ | 1.43A | 1.40198A | $C_5C_6HO_5$ | 119.743° | 127.236° |
| $C_4H$ | 1.09A | 1.12203A | $C_6O_4C_2$ | 119.743° | 120.239° |
| $C_4C_5$ | 1.53753A | 1.54967A | | | |

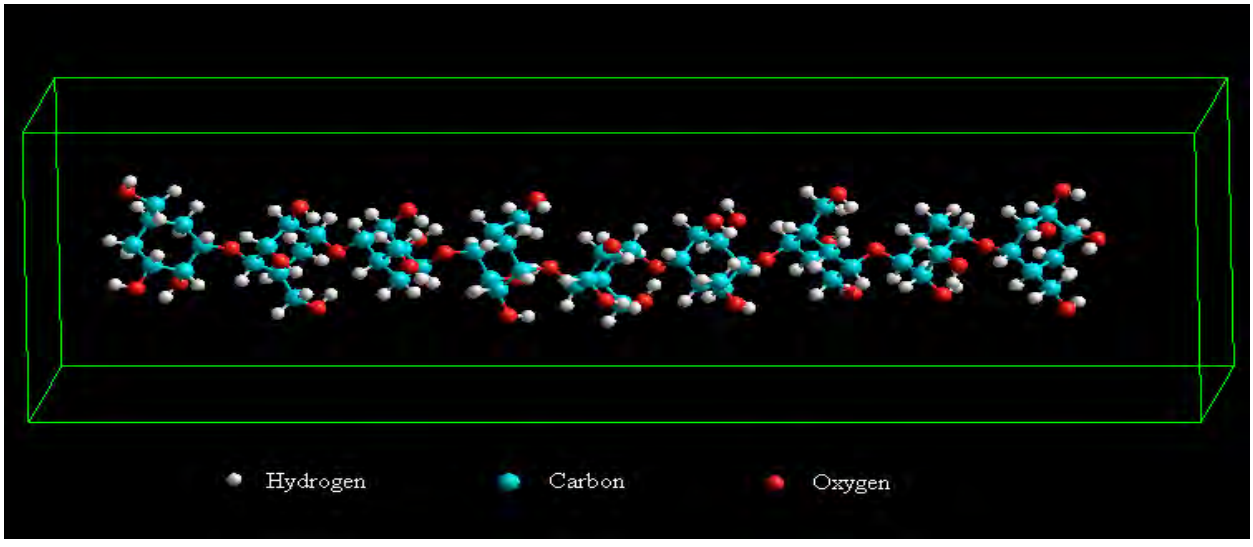


**Figure 1.** The model of cellulose molecule (n=9).

 

### 2.2. Assumptions in Simulation

1) The broken groups have no influence on subsequent bond break.

2) The broken groups didn't get together and form new molecules.

3) The broken groups didn't decompose secondarily.

## 3. FOFCE FIELD

Force field, with relation to reliability of the result, is the base of molecular dynamic simulation. The force fields become more and more complex as computing systems swell. It has different forms with its advantages and limits in each form. Some force fields can be chosen when the organic molecule was simulated, such as $MM^+$, AMBER, CHARMM, OPLS [7,8,9,10].

### 3.1. Force Fields for Simulation

The total potential energy expression of the macromolecule is partitioned into several energy terms as given in **Eq.1**. These contributions include non-bonding energies ($U_{nb}$), bond stretching energies ($U_b$), angle bending energies, ($U_\theta$), torsion angle energies $U_\phi$, out-of-plant bending energies ($U_x$), columbic interaction energies ($U_{el}$).

$$U = U_{nb} + U_b + U_\theta + U_\phi + U_\chi + U_{el} \tag{1}$$

AMBER (Assisted Model Building and Energy Refinement) force field which was developed by Peter A Kollman and coworkers in University of California San Francisco was widely used for proteins and DNA. Force field functions and parameter sets are derived from both experimental work and high-level quantum mechanical calculations. The first three terms in **Eq.2** denote the internal coordinates of bond stretching, angle bending and torsions. The non-bonded terms account for the Van DerWaals and electrostatic interactions and the last term represent the 12-6 Lennard-Jones hydrogen bond treatment.

$$U = \sum_b K_b (b - b_0)^2 + \sum_\theta K_\theta (\theta - \theta_0)^2 + \sum_\phi \frac{1}{2} V_0 [1 + \cos(n\phi - \phi_0)]$$
$$+ \sum \varepsilon [(r^*/r)^{12} - 2(r^*/r)^6] + \sum \frac{q_i q_j}{\varepsilon_{ij} r_{ij}} + \sum (C_{ij}/r_{ij}^{12} - D_{ij}/r_{ij}^{10}) \tag{2}$$

CHARMM (Chemistry at Harvard Macromolecular Mechanics) force field was developed by Harvard, the parameter of which come form not only the result of experiment and computing, but also calculation result of quantum. It was used for many molecular systems, including organic micro molecule, solution, polymer, biochemical molecule. The form of the potential energy function we will use is given by the following equation [3]:

$$U = \sum k_b (r - r_0)^2 + \sum k_\theta (\theta - \theta_0)^2 + \sum [|k_\varphi| - k_\varphi \cos(n\phi)] +$$
$$\sum k_\chi (\chi - \chi_0) + \sum_{i,j} \frac{q_i q_j}{4\pi\xi_0 r_{ij}} + \sum_{i,j} \left(\frac{A_{ij}}{r_{ij}^{12}} - \frac{B_{ij}}{r_{ij}^6}\right) sw(r_{ij}^2, r_{on}^2, r_{off}^2) \tag{3}$$

where $sw(r_{ij}^2, r_{on}^2, r_{off}^2)$ is switching function.

$MM^+$ force field was developed by Allinger. El, some common atoms are divided different forms, which have different parameters. It was applied in organic compounds, free radical, ions. The normal form is given:

$$U = U_{nb} + U_b + U_\theta + U_\phi + U_\chi + U_{el} + U_{cross} \tag{4}$$

where $U_{nb}(r) = a\varepsilon \cdot e^{-c\sigma/r} - b\varepsilon\left(\frac{\sigma}{r}\right)^6$

$$U_\phi(\phi) = \sum_{n=1}^{3} \frac{V_n}{2}(1 + \cos n\phi) \quad U_x(x) = k(1 - \cos 2x)$$

$$U_\theta(r) = \frac{k_\theta}{2}(\theta - \theta_0)^2 [1 - k'_\theta(\theta - \theta_0) - k''_\theta(\theta - \theta_0)^2 - k'''_\theta(\theta - \theta_0)^3]$$

$$U_b(r) = \frac{k_b}{2}(r - r_0)^2 [1 - k'_b(r - r_0) - k''_b(r - r_0)^2 - k'''_b(r - r_0)^3]$$

$U_{cross}$ is cross action term which is given by following EQ while the bond lengths are $r_1$ and $r_2$ for the same molecule.

$$U(r_1, r_2) = \frac{k_{12}}{2}(r_1 - r_{1,0})(r_2 - r_{2,0})$$

OPLS force field formed by OPLS-UA model and OPLS-AA model was used for simulating organic molecules and multi-peptide. The parameters of bond extension and bend were attained form AMBER force field. OPLS force field is mainly used for computing the conformation energy of gaseous organic molecule, hydration free energy of organic liquid, and other thermodynamics features.

$$U = \sum_b k_r (r - r_{eq})^2 + \sum_\theta k_\theta (\theta - \theta_{eq})^2 + V_0 +$$
$$\frac{V_1}{2}[1 + \cos(\phi + f_1)] + \frac{V_2}{2}[1 - \cos(2\phi + f_2)]$$
$$+ \frac{V_3}{2}[1 + \cos(3\phi + f_3)] + \sum_i^a \sum_j^b (q_i q_j e^2/r_{ij} + A_{ij}/r_{ij}^{12} - C_{ij}/r_{ij}^6) \tag{5}$$

### 3.2. The Energy History

During the heating process (100ps>t>0ps), the total energy increases as temperature rises. But in the simulation process (t>100ps), the temperature is constant and the total energy is steady. Form **Fig. 2**, as can be seen, the total energy lowered to minimum in a short time at the beginning of simulation. The energy was adjusted

 

after the system was optimized and before simulating, the range of which was $E_o > E_c > E_m > E_a$. **Table 2**. shows the energy adjustment range of OPLS is largest and the total energy is $E_{ch} > E_{am} > E_{mm} > E_{op}$.

### 3.3. Comparison of Different Force Fields

The straight chain starts to bend from both sides to the middle as the energy of each atom in the chain of cellulose rises; atoms move and vibrate more and more strongly. The groups in the cellulose begin to break when the total energy of system come to the special value. The breaking temperature is TO > TC > TA > TM as show in **Table 3**. Cellulose breaks more and more strongly as the temperature rises while only a few groups break at the beginning. The temperature of main decomposition process is shown in **Table 2**, from which the conclusion can be drawn: AMBER force field quite agrees with the experiment value [11].

## 4. SIMULATION RESULTS BASE ON AMBER FORCE FIELD

### 4.1. The Energy History in Heating Process

The system was heated at the initial temperature of 273K. **Fig. 3** shows the whole temperature history during the heating-up process. The temperature gradually rises during heating process with bigger fluctuation at higher temperature. The total energy history is shown in shown in **Fig. 4**, form which the rise of total energy as time going can be seen.

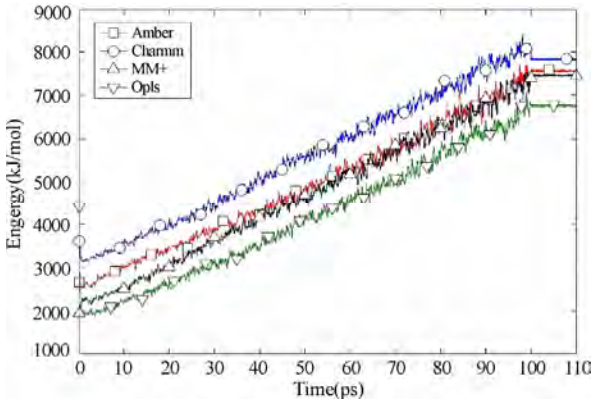


**Figure 2.** The energy histories of simulation process.

### 4.2. Breaking of Molecular Chain

Not considering bond bonding, the heating process includes two stages: vibrate at low temperature and break at high temperature. During low temperature (273k-375k), the length of bond grows, bond angles bend, torsion angles increase. Stretching energies ($U_b$), angle bending energies ($U_\theta$), torsion angle energies($U_\Phi$) and out-of-plant bending energies ($U_\chi$) increase, but the bond was not broken due to non-bonding energies ($U_{nb}$) and columbic interaction energies ($U_{el}$). As seen in **Fig. 5**, atoms vibrate more and more strongly and

**Table 2.** Different Force Fields Parameters.

| | Amber | Charmm | $MM^+$ | Opls | Experiment |
|---|---|---|---|---|---|
| Initial Energy (kJ/mol) | 2644.3 | 3606.6 | 1924.6 | 4418.3 | |
| Adjusted Energy (kJ/mol) | 2502 | 3117.1 | 2288.6 | 1912.1 | |
| Energy difference (kJ/mol) | -142.3 | -489.5 | 364 | -2506.2 | |
| Balanced Energy (kJ/mol) | 7564.7 | 7836.6 | 7455.9 | 6757.2 | |
| Temperature of starting decomposition (K) | 380 | 390 | 310 | 417 | 400 |
| Main Temperature Ranges of Decomposition (K) | 420~750 | 450~860 | 310~710 | 600~950 | 480~700 |

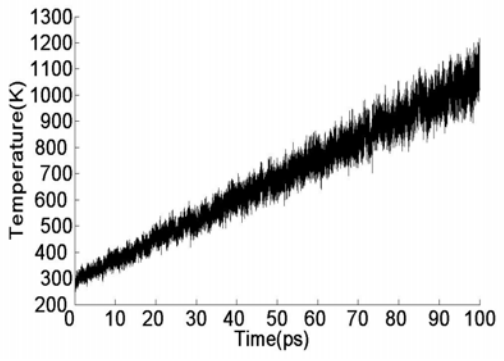


**Figure 3.** The temperature history of system.

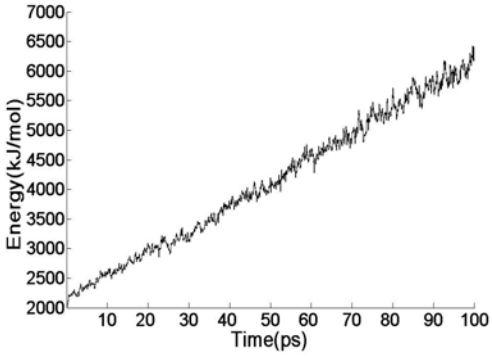


**Figure 4.** The energy history of system.

 

the straight chain starts to bend from both sides to the middle. When the temperature of the system arrived at 375K, it comes to breaking stage. The groups move stronger with the increasing of temperature, some of which overcome the electronic force and van der waals force and leave from the long chain. Then, chemical bonds break and cellulose starts to decompose (**Fig. 6**). When the length of chemical bond is larger than 1.2 times of its original length, we think that it is broken or disappears.

Many groups are formed when cellulose begins to break and many of short chain groups can be obtained in low temperature process, such as: (-OH), (-CO-), (-CHOH-CHOH-), (-CHOH-$CH_2$-$CH_2$-), (-$CH_2$OH), (-$CH_3$), (-$CH_2$-$CH_2$-), (-$CH_2$-$CH_2$-CHOH-), (-CH=CH-CHOH-), (-CH=CH-), (-CHOH-CHOH-$CH_3$), (-$CH_2$-$CH_2$-$CH_2$- $CH_2$-), (-CHOH-$CH_2$-CH(C)-CHOH-), (-CHOH-$CH_2$-$CH_2$-). A number of unsteady (OH) groups which are prone to release free groups [O] exist in the system after breaking.

$$(-OH)+(-OH)\rightarrow H_2O+[O] \quad (6)$$

A lot of free groups [O] accelerate the oxidation reaction. Bottom (-OH) is oxidated to corresponding aldehyde and acids. For example:

$$CH_3-CH_2-OH \xrightarrow{[O]} CH_3-CH=O+H_2O \quad (7)$$

$$CH_3-CH=O \xrightarrow{[O]} CH_3-COOH \quad (8)$$

(-OH) in the middle also can be oxidated to ketone or be alkene off-(-OH),

$$CH_3-C(OH)H-CH_3 \xrightarrow{[O]} CH_3-C(O)-CH_3+H_2O \quad (9)$$

$$CH_3-CH_2-OH \rightarrow CH_2=CH_2+H_2O \quad (10)$$

and:

$$CO \xrightarrow{[O]} CO_2 \quad (11)$$

$$CH_3+CH_3 \rightarrow CH_3-CH_3 \quad (12)$$

$$CH_3+OH \rightarrow CH_3OH \quad (13)$$

$$CH_4 \xrightarrow{[O]} CH_2O+H_2 \quad (14)$$

The re-combination of these broken groups form the first production such as: $CO_2$, $H_2O$(L), $CH_4$, alkanes such as:$CH_3$-$CH_3$, olefin such as $CH_2$=$CH_2$, aldehydes such as $CH_2O$. With the further increasing of temperature, organic biological oil with more than 6 carbons formed with highest production rate at around 800K-850K, which is quite matched with the experiments [11].

### 4.3. The Order of Molecule Breaking

The order of cellulose bonds breaking are obtained when the broken groups are shielded after the cellulose breaking. **Fig. 7** shows the planar structure of carbon and oxygen, and the hydrogen is not shown because the breaking of (O-H) and (C-H) is not involved. The numbers show the orders and the letters show the units number of cellulose.

In one unite of cellulose, the hydroxyl groups (-OH) in the ring shed first, then the hydroxyl (-OH) in branched chain and the ring. Sometimes the whole ring breaks directly, unit I, for example. The (C-O) which has the lowest energy in the chain of cellulose breaks first because decomposition always occurs from the lowest energy.

As for the whole chain of cellulose molecule, the molecule chain decomposes from both sides to the middle gradually. The hydroxyl (-OH) of inside unit will break earlier than the ring of two-terminals. Separate adjustment is reasonable because the order given in this paper is not steady for the randomness of chemical reaction. In spite of thus bugs, the general tendency is correct.

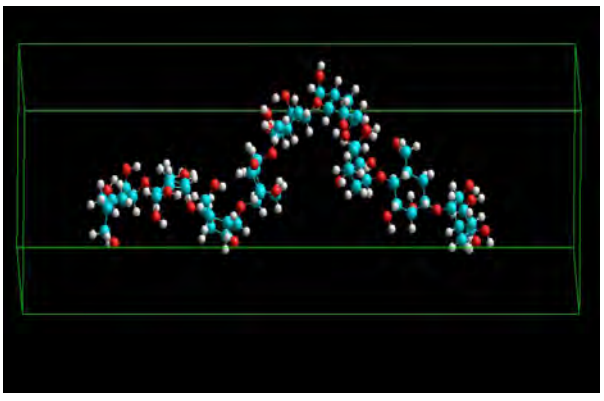

**Figure 5.** The process of heating.

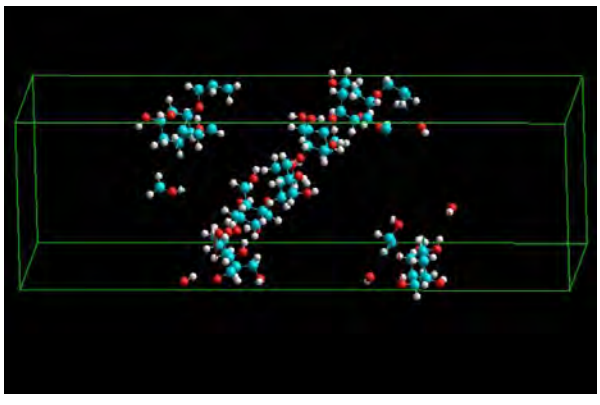

**Figure 6.** The process of decomposition.

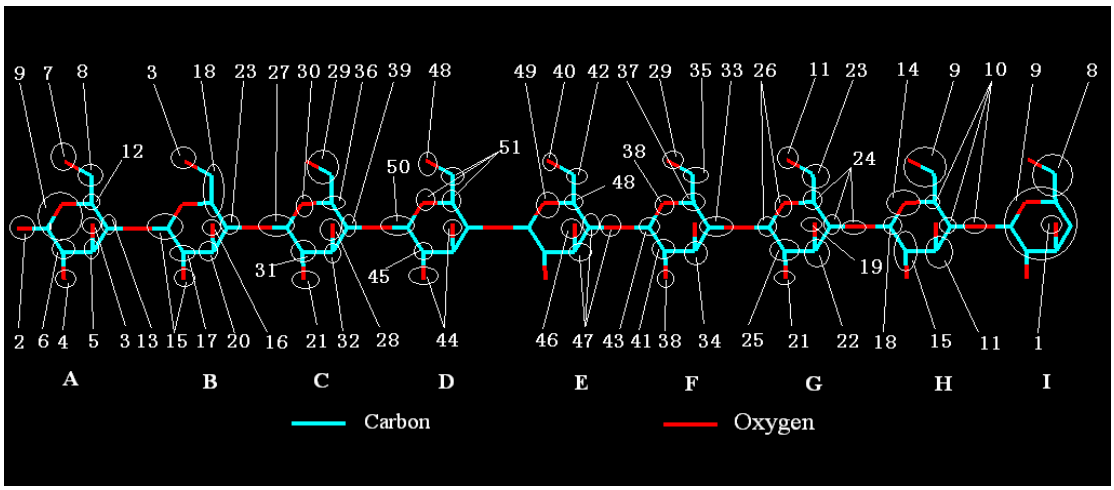


**Figure 7.** The breaking order of cellulose single chain.

## 5. CONCLUSIONS

1) Series of parameters of cellulose structure were obtained by optimizing the cellulose chain.

2) AMBER force field is more adaptive for simulating cellulose with lower polymerization degree than others.

3) Details of cellulose thermal decomposition and the ranges of decomposition temperature are gotten from the simulation. The order of cellulose unit breaking is obtained. Therefore, the detailed process of cellulose thermal decomposition is shown.

4) The heating process includes two stages: vibrate at low temperature and break at high temperature (273k-375k) and breaking stage when the temperature of the system arrived at 375K.

5) The re-combination of these broken groups which were gotten from thermal decomposition forms the first production which was the most important product.

The conclusions concluded from the simulation of cellulose thermal decomposition by molecular dynamic model matches the experiment quite well, convincing molecular dynamics could be a very significant tool for science research. The results of the simulation are very significative for the following researches.

## ACKNOWLEDGEMENTS

The Project is sponsored by the National Natural Science Foundation of China (No. 50776101)

## REFERENCES

[1] Cook, J. and Beyea, J. (2000) Bioenergy in the United States: Progress and possibilities. Biomass and Bioenergy, **18(6)**, 441−441.

[2] McKendry, P. (2002) Energy production from biomass: gasification technologies. Bioresource Technology, **83**, 55−63.

[3] McKendry, P. (2002) Energy production from biomass: Conversion technologies. **83**, 47−54.

[4] Bridgwater, A. V. (1999) Principles and practice of biomass fast pyrolysis processes for liquids. Journal of Analytical and Applied Pyorlysis, **51**, 3−22.

[5] Slesser, M. and Chris, L. (1982) Biological energy resources. London: E&F. N. Spom Ltd.

[6] Purves, C. B. (1954) Cellulose and cellulose derivatives. Part 1, Interscience, New York, 29−98.

[7] Weiner, S. J. and Kollman, P. A. (1984) D A Case. J. Am. Chem. Soc, **106**, 765−784.

[8] Brooks, B. R., Bruccoleri, R. E., Olafson, B. D. *et al.* (1983) J. Comput. Chem, **4**, 187−217.

[9] Allinger, N. L. and Yan, L. (1993) J. Am. Chem. Soc., 115−119.

[10] Qui~nonero, D., Tomas, S. and Frontera, A. (2001) OPLS all-atom force field for squaramides and squaricacid. Chemical Physics Letters, **9**, 331−338.

[11] Liao, Y. F. (2003) Mechanism study of biomass pyrolysis. [Ph. D. Thesis]. Hang Zhou, Zhejiang University, China.

[12] Tan, H. (2005) Mechanism study of biomass pyrolysis. [Ph. D. Thesis]. Hang Zhou, Zhejiang University, China.

 

**Natural Science, 2009, 1, 47-54** **NS**

# Adaptation fermentation of *Pichia stipitis* and combination detoxification on steam exploded lignocellulosic prehydrolyzate

**Jun-Jun Zhu[1], Qiang Yong[1], Yong Xu[1], Shang-Xing Chen[2], Shi-Yuan Yu[1*]**

[1]Ministry of Education, Key Laboratory of Forest Genetics & Biotechnology, Nanjing Forestry University, Nanjing 210037, China; [2]College of Forestry, Jiangxi Agricultural University, Nanchang 330045, China. [*]Corresponding author: Tel: +86 25 85427255; Fax: +86 25 85418873.
E-mail: [*]shiyuanyu.nfu@gmail.com

Received 25 May 2009; revised 5 June 2009; accepted 8 June 2009.

## ABSTRACT

**Yeast *Pichia stipitis* CBS 5776 was developed through adaptation fermentation step by step in steam exploded corn stover prehydrolyzate because high concentration of weak acids and other inhibitors present in the prehydrolyzate could degrade the fermentability. However, the adaptability of *Pichia stipitis* CBS 5776 in the prehydrolyzate was so limited that steam stripping and overliming were applied to remove these inhibitors from it. Corn stover was steam exploded; the filtrate of steam exploded corn stover was hydrolyzed with dilute sulfuric acid, and then the acid hydrolyzate was detoxified and fermented by *Pichia stipitis* CBS 5776. Steam stripping could remove volatile compounds from the acid hydrolyzate and the filtrate. At a steam stripping time of 120min, 81% acetic acid and 59% formic acid were removed from the acid hydrolyzate, 77% acetic acid and 45% formic acid were removed from the filtrate, while furfural was stripped off completely from the acid hydrolyzate and the filtrate. Overliming could reduce the contents of furfural and phenolics present in the acid hydrolyzate, however, sugars, especially pentoses, were also removed partially. It was necessary to detoxify the acid hydrolyzate in order to ferment the sugars to ethanol. Acid hydrolyzate detoxified with a combination of steam stripping for 120 min and overliming at pH11 and 60℃ for 90 min, its fermentability was significantly improved. Xylose was consumed nearly completely in 24h with an ethanol yield of 15.92g/l, 80.34% of theoretical.**

**Keywords:** Steam Explosion; Steam Stripping; Overliming; Inhibitor; Acid Hydrolyzate

## 1. INTRODUCTION

For several decades, ethanol has been promoted as a promising alternative fuel for transportation. The use of fossil fuels has contributed to the buildup of carbon dioxide in the atmosphere; however ethanol is a clean-burning fuel that makes no net contribution to global warming because the carbon dioxide produced by the combustion of ethanol is consumed by plant growth which continues the carbon cycle balance in the nature. Ethanol can be produced from any material containing simple or complex sugars, such as sugar cane and various starchy materials (corn, wheat, and potatoes). However, the most promising raw material is represented by lignocellulose because of its renewable nature, abundance and low cost [1].

Lignocelluloses are mainly comprised of cellulose, hemicellulose, and lignin. The substrate must be pretreated so that it is more amenable to conversion. A number of pretreatments such as dilute acid hydrolysis [2], alkali treatment [3], sodium sulphite treatment [4], steam explosion [5], ammonia fiber explosion [6], lime treatment [7], wet oxidation [8], liquid hot water pretreatment [9], organic solvent treatment [10], and biologial pretreatment [11], and so on, have been used frequently to improve the saccharification of the carbohydrates. Of these methods, steam explosion has been recognized as one of the most cost- effective and potential pretreatment methods [12,13]. During the pretreatment process with high temperature, a part of cellulose, hemicellulose and lignin is degraded to produce compounds which inhibit enzymatic hydrolysis and ethanol fermentation. The main degraded products from steam exploded corn stover have been identified by HPLC and GC-MS analysis [14].

The inhibiting compounds are divided into three main groups based on origin: weak acids, furan derivatives, and phenolic compounds. Weak acids (formic, acetic, and levulinic acid), furan derivatives (furfural, 5-hy-

droxymethylfurfural) from sugar degradation, phenol compounds from lignin degradation are considered to be potential fermentation inhibitors from pretreated lignocellulose [15]. In order to improve the fermentability of yeast, it can be done from the following two aspects, one is to make the yeast to adapt to the prehydrolyzate step by step, and another is to adopt methods to remove the inhibitors from the prehydrolyzate. Nigam investigated a mutant *Pichia stipitis* NRRL Y-7124 to adapt in acid hydrolyzate. When it was tested for its ability to ferment acid hydrolyzate, it showed shorter fermentation time, better tolerance to acid and could ferment at lower pH. The ethanol yield and productivity were increased 1.3 and 2.1 fold, respectively [16]. However, more researchers investigated detoxification methods to detoxify the hydrolyzate to improve fermentation efficiency. Detoxification methods include neutralization [17], overliming [18], steam stripping [19], ion-exchange [20], treatment with activated carbon [20], wood charcoal [21], and laccase and peroxidase [22]. In many instances, the most economical and widely used method of detoxification involves treatment of hydrolyzates with solid calcium hydroxide [23]. This process of "overliming" is reported as an effective method of reducing toxicity of various hydrolyzates [24]. However, different yeasts endure the ability of inhibitors differently. Previous investigation in this laboratory indicated that only "overliming" was not an effective method to detoxify hydrolyzate fermented by Yeast *Pichia stipitis* CBS 5776 (data not shown), probably because overliming could not remove acetic and formic acid which inhibited the fermentability.

In this work, *Pichia stipitis* CBS 5776 was adapted in the filtrate with addition of xylose 30g/l step by step, and at the same time, steam stripping was firstly used to remove the volatile compounds such as formic and acetic acid in the acid hydrolyzate or filtrate, then overliming was performed to remove more other inhibitors. Xylose was added up to 45g/l to three kinds of hydrolyzates, undetoxified hydrolyzate, the hydrolzyate treated with steam stripping, and the hydrolyzate treated with a combination of steam stripping and overliming. The fermentabilities of the three kinds of hydrolyzates with yeast *Pichia stipitis* CBS 5776 were investigated.

## 2. MATERIALS AND METHODS

### 2.1. Preparation of Acid Hydrolyzate

Corn stover was obtained from Zhaodong city, Heilongjiang Province, China. The main composition of the raw material was (w/w% of the dry weight): glucan, 40.10; xylan, 22.30; and lignin, 18.80. The corn stover was crushed to a granularity of 3 to 5cm, and then steam treated at 1.8MPa for 5min before explosion. After steam explosion, 100g (dry weight) exploded corn stover was washed and filtered three times with 1L distilled water. The filtrate was then hydrolyzed with dilute sulfuric acid 30g/l at 121℃ for 45min.

### 2.2. Detoxification of the Acid Hydrolyzate and the Filtrate

The acid hydrolyzate or the filtrate was heated to boiling and kept at 100℃. Steam was then put into the bottom of the vessel with a distributor to perform stripping. Steam stripping was operated for 15, 30, 45, 60, 90, and 120 min, respectively.

Overliming was carried out by initially adjusting the pH of the acid hydrolyzate to pH9, 10 and 11, respectively, using solid calcium hydroxide. The samples were then heated to 40 or 60℃ in a water bath for 90min followed by centrifuging at 5000 rpm for 10min. The upper liquid was collected and stored at 4℃.

A combination of steam stripping and overliming was also performed for detoxification of the acid hydrolyzate. The hydrolyzate was firstly detoxified by steam stripping as described above; the sample's volume was adjusted to its original volume by the addition of water. The sample was then detoxified by overliming procedure.

### 2.3. Yeast Strain and Media

The yeast *Pichia stipitis* CBS 5776 was conserved in Nanjing Forestry University. It was maintained at 4℃ in a medium containing (g/l): xylose, 20; yeast extract, 5; peptone, 3; and agar, 20.

Inoculation medium contained 30g/l xylose, 5g/l peptone and 3g/l yeast extract at natural pH. Multiplication medium was similar to the inoculation medium. The xylose fermentation medium was described previously by Yu [25].

Inoculum was prepared in 250ml shaking flask with 100ml medium, and incubated on a rotary shaker at 170 rpm and 30℃ for several batches (24 hours per batch). When the optical density (OD) of yeast cells reached 10, the cells were harvested by centrifugation, and the pellet was inoculated into the fermentation media.

### 2.4. Adaptable Fermentation

Adaptation medium was prepared by adding 30g/l xylose and the other compositions were described by Yu [25] in 10%, 20%, 30%, 40% and 50% (v/v) filtrate of steam exploded corn stover.

The cells from inoculum preparation were firstly inoculated into 100 ml of the adaptation fermentation medium of 10% filtrate in 250ml shaking flask at 30℃ on a rotary shaker at 150 rpm for 22h, then repeated fermentation of 10 % filtrate for two times, finally the cells was inoculated into 20%, 30%, 40% and 50% filtrate and fermented for three times, respectively.

 

### 2.5. Fermentation of the Detoxified and Undetoxified Acid Hydrolyzates

Three acid hydrolyzate preparations, namely the hydrolyzate without detoxification, the hydrolyzate treated with steam stripping only, and the hydrolyzate treated with a combination of steam stripping and overliming, were used for fermentation.

The pH of the hydrolyzate preparations was adjusted to 5.5 by the addition of $Ca(OH)_2$ or $H_2SO_4$. The hydrolyzate preparations were then centrifuged at 5000 rpm for 10min; the upper liquids were collected and stored at 4℃. Xylose 45g/l was added to the three hydrolyzate preparations as the sugar sources. Fermentation was carried out in 250ml shaking flask with 100ml medium, and incubated on a rotary shaker at 150 rpm and 30℃.

### 2.6. Analysis

Sugars (cellobiose, glucose, xylose, and arabinose), fermentation products (ethanol, xylitol, glycerol) and inhibitors (formic acid, acetic acid, levulinic acid, 5-hydroxymethylfurfural, and furfural) were determined by high performance liquid chromatography (HPLC) using an Agilent 1100 system and refractive index detector. Separations were performed on a Bio-rad Aminex HPX-87H column (300×7.8mm i.d.) at 55℃ using 0.005 mol/l sulfuric acid as the mobile phase (0.6ml/min). All the compounds were determined by ESTD methods.

The optical density (OD) of the yeast was measured spectrophotometrically at 600nm.

Spectrophotometric analysis of the hydrolyzate was performed using an Amersham Biosciences Ultrosepc 2100 *pro* UV/visible spectrophotometer. The hydrolyzates were diluted 100 times for measurements at 280nm.

## 3. RESULTS AND DISCUSSION

### 3.1. Compositions of the Filtrate and the Acid Hydrolyzate from Steam Exploded Corn Stover

Cellulose, hemicellulose, lignin and extractives in the corn stover were partially degraded and decomposed during steam explosion pretreatment [26]. The soluble degraded products included sugars (glucose, xylose, and arabinose) and inhibitory compounds (formic acid, acetic acid, levulinic acid, 5-hydroxymethylfurfural, furfural, and so on). Soluble oligosaccharides were also found in the filtrate because they could not be entirely degraded to monosaccharides during steam explosion, and they could not be fermented to ethanol by yeasts; therefore 30g/l sulfuric acid was applied to hydrolyzate the oligosaccharides to monosaccharides such as glucose and xylose at 121℃ for 45min. The contents of the filtrate and the acid hydrolyzate from steam exploded corn stover were analyzed with HPLC and were shown in **Table 1**.

From **Table 1**, it could be seen that the concentration of xylose increased more than that of glucose, this indicated that xylooligosaccharides was more easily hydrolyzed to monosaccharides than cellooligosaccharides. After acid hydrolysis of the filtrate, formic acid, acetic acid and 5-hydroxymethylfurfural were decreased partially; however, levulinic acid and furfural were increased. The changes of inhibitors in the filtrate showed that a series of degradation reactions were occurred during the process of the acid hydrolysis.

### 3.2. Adaptation Fermentation

Since the sugar contents in the filtrate was too low, 30 g/l xylose was added to the adaptation media containing 10%, 20%, 30%, 40%, and 50% filtrate. Adaptation of the yeast *Pichia stipitis* CBS 5776 was achieved in the adaptation medium. Firstly, *Pichia stipitis* CBS 5776 was fermented on the adaptation medium of 10 % filtrate for three times, after each fermentation, the centrifuging yeast was inoculated in the fresh adaptation medium; secondly, the yeast was inoculated in the adaptation medium of 20% filtrate for three times. The adaptation sequence was continued gradually until the adaptation medium of 50% filtrate. **Fig. 1** presented that the changes of the concentrations of residue xylose, fermentation product ethanol, the main fermentation by-product xylitol adapted fermentation in 10%, 20%, 30%, 40%, and 50% filtrate for three times by *Pichia stipitis* CBS 5776.

As shown in **Fig. 1**, the concentration of residue xylose was increased from 0 in the 10% and 20% filtrate to 19.54g/l (means of triplicate) in the 50% filtrate with the increasing concentration of the filtrate. The fermentation product ethanol was firstly a little increased, and then decreased linearly; the maximum concentration of ethanol was 11.59g/l (means of triplicate) in the 20% filtrate. The fermentation by-product xylitol was decreased firstly and then increased a little; the maximum concentration of xylitol was 0.95g/l (means of triplicate) in the 10% filtrate.

**Table 1.** Contents of the filtrate and acid hydrolyzate from steam exploded corn stover.

| Compounds | Concentration (g/l) | |
|---|---|---|
| | The filtrate | The acid hydrolyzate[a)] |
| Cellobiose | 0.33 | 0.12 |
| Glucose | 0.30 | 1.27 |
| Xylose | 0.79 | 2.13 |
| Arabinose | 0.27 | 0.29 |
| Formic acid | 2.07 | 1.82 |
| Acetic acid | 2.03 | 1.93 |
| Levulinic acid | 0.12 | 0.19 |
| 5-hydroxymethylfurfural | 0.15 | 0.09 |
| Furfural | 0.10 | 0.18 |

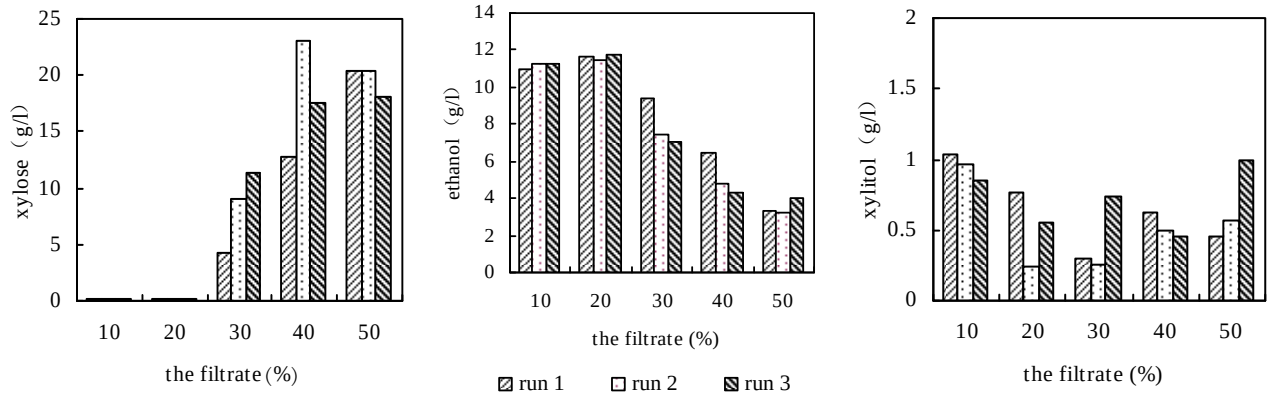


**Figure 1.** Changes of the concentrations of residue xlose, ethanol and xylitol adapted fermentation in 10 %, 20 %, 30 %, 40 %, and 50 % filtrate for three times by *Pichia stipitis* CBS 5776 with the addition of xylose 30g/1.

From the results of the three times of adaptation fermentation in 10% to 50% filtrate by *Pichia stipitis* CBS 5776, it could be concluded that the fermentability was decreased gradually with the increasing concentration of the filtrate, especially in 50% filtrate only 3.55g/l (means of triplicate) ethanol was produced. So *Pichia stipitis* CBS 5776 endured the concentration of inhibitors had some limitation, only adaptation yeast in the filtrate could not improved the fermentability significantly. Therefore, it was necessary to adopt detoxification methods to detoxify or remove inhibitors in the filtrate in order to further improvement of fermentation.

### 3.3. Steam Stripping of the Acid Hydrolyzate and the Filtrate

Steam stripping was considered as one of the physical detoxification methods. It only removed the volatile compounds in the hydrolyzate. The filtrate from steam exploded corn stover was hydrolyzed at a sulfuric acid concentration of 30g/l at 121℃ for 45 min as described above. The resulted acid hydrolyzate was then steam stripped for 15, 30, 45, 60, 90, and 120 min, respectively. At the same time, steam stripping of the filtrate was also investigated. The effects of stripping time on the compositions of detoxified acid hydrolyzate and the filtrate were summarized in **Tables 2 and 3**.

From **Tables 2 and 3**, it could be seen that the concentrations of sugars, such as cellobiose, glucose, xylose and arabinose, remained essentially the same as expected. The non-volatile inhibitors, levulinic acid and 5-hydroxymethylfurfural, were not removed as well. On the other hand, the volatile inhibitors, formic acid, acetic acid and furfural, were removed significantly.

The removal of acetic acid was much higher than that of formic acid. And the removal of formic acid in the acid hydrolyzate (1.07g/l) was much more than that in the filtrate (0.73g/l). The possible reason is that the pKa value of acetic acid (4.75) is higher than that of formic acid (3.75). In the acidic condition (pH1-2), acetic acid is prone to form molecules, which can be removed easily. While in the filtrate, its pH was 4.00, the formic acid was existed in ion formation, so it was not easy to remove. With the stripping time going on, the removal of acetic acid and formic acid slowed down gradually because the

**Table 2.** Effect of stripping time on the composition of detoxified the acid hydrolyzate.

| Compound (g/l) | 0 | 15 min | 30 min | 45 min | 60 min | 90 min | 120 min |
|---|---|---|---|---|---|---|---|
| Cellobiose | 0.12 | 0.11 | 0.12 | 0.12 | 0.12 | 0.12 | 0.12 |
| Glucose | 1.27 | 1.27 | 1.28 | 1.31 | 1.32 | 1.33 | 1.24 |
| Xylose | 2.13 | 2.10 | 2.11 | 2.15 | 2.17 | 2.20 | 2.02 |
| Arabinose | 0.29 | 0.28 | 0.28 | 0.29 | 0.29 | 0.29 | 0.28 |
| Formic acid | 1.82 | 1.49 | 1.34 | 1.06 | 0.97 | 0.81 | 0.75 |
| Acetic acid | 1.93 | 1.41 | 1.09 | 0.70 | 0.58 | 0.42 | 0.37 |
| Levulinic acid | 0.19 | 0.17 | 0.19 | 0.20 | 0.19 | 0.21 | 0.21 |
| 5-hydroxymethylfurfural | 0.09 | 0.08 | 0.08 | 0.08 | 0.08 | 0.08 | 0.06 |
| Furfural | 0.18 | 0.00 | 0.00 | 0.00 | 0.00 | 0.00 | 0.00 |

 

**Table 3.** Effect of stripping time on the composition of detoxified the filtrate of steam exploded corn stover.

| Compound (g/l) | 0 | 15 min | 30 min | 45 min | 60 min | 90 min | 120 min |
|---|---|---|---|---|---|---|---|
| Cellobiose | 0.33 | 0.32 | 0.31 | 0.31 | 0.30 | 0.28 | 0.29 |
| Glucose | 0.30 | 0.29 | 0.29 | 0.29 | 0.28 | 0.27 | 0.28 |
| Xylose | 0.79 | 0.80 | 0.80 | 0.80 | 0.76 | 0.74 | 0.76 |
| Arabinose | 0.27 | 0.27 | 0.26 | 0.26 | 0.26 | 0.24 | 0.25 |
| Formic acid | 2.07 | 1.94 | 1.82 | 1.77 | 1.50 | 1.40 | 1.34 |
| Acetic acid | 2.03 | 1.65 | 1.26 | 1.04 | 0.78 | 0.77 | 0.46 |
| Levulinic acid | 0.12 | 0.11 | 0.11 | 0.11 | 0.11 | 0.10 | 0.11 |
| 5-hydroxymethylfurfural | 0.15 | 0.14 | 0.14 | 0.14 | 0.11 | 0.12 | 0.13 |
| Furfural | 0.10 | 0.00 | 0.00 | 0.00 | 0.00 | 0.00 | 0.00 |

molecule forms of acetic acid and formic acid were reduced with the pH increasing [27].

According to the results of **Tables 2 and 3**, it was necessary to hydrolyze the filtrate with dilute sulfuric acid, because it was not only hydrolyzed the oligosaccharides to monosaccharides, but also it could be removed more inhibitors in the hydrolyzate. So in this study, the filtrate was firstly hydrolyzed with 30g/l sulfuric acid at 121℃ for 45min, and then a steam stripping time of 120min was selected in order to remove more inhibitors. At this condition, 81% acetic acid and 59% formic acid were removed, while furfural was stripped off completely.

### 3.4. Overliming of the Acid Hydrolyzate

The effect of detoxification of the acid hydrolyzate by overliming on sugars (cellobiose, glucose, xylose, and arabinose), weak acids (formic, acetic, and levulinic acid), 5-hydroxymethylfurfural and furfural was examined. The pH was adjusted to 9, 10, and 11, respectively, and the temperature was set at 40 and 60 ℃ for each pH treatment. The overliming time was 90 min [28]. The results of detoxification were summarized in **Table 4**.

As shown in **Table 4**, the concentration of cellobiose, arabinose, formic acid, acetic acid, levulinic acid and 5-hydroxymethylfurfural were unchanged or changed slightly when treated with $Ca(OH)_2$ to pH 9-11 at 40 and 60℃. The concentration of xylose and glucose was decreased at pH11, especially when higher temperature (60 ℃) was applied. Xylose was more destroyed than glucose; this agreed with Martinez's results [18] in which pentose sugars were less stable than hexose sugars when pH was increased from 9 to 11. The concentration of furfural was reduced by treatment with $Ca(OH)_2$. At pH11, 41% and 50% furfural were removed at 40 and 60℃, respectively.

The spectrophotometric analyses of different treatments were also listed in **Table 4**. Absorbance at 280nm represents furfural, 5-hydroxymethylfurfural and phenyl ring absorption band in lignin [22]. Compared with the absorbance value at 280nm, 1.93, of the untreated acid hydrolyzate, the absorbance values of overliming treatment were decreased with the pH increasing. This indicated that a part of furfural and phenolics had been removed.

### 3.5. Detoxification of the Acid Hydrolyzate with a Combination of Steam Stripping and Overliming

According to the results of steam stripping and overliming, the acid hydrolyzate was then detoxified with a two step method. The acid hydrolyzate was firstly detoxified by steam stripping for 120min, water was added to maintain the original value, and then the acid hydrolyzate was secondly detoxified by overliming at pH11 and 60℃ for 90 min. The composition of the acid hydrolyzate after two step detoxification was listed in **Table 5**.

**Table 4.** The effect of pH and temperature on the overliming detoxification of the acid hydrolyzate.

| Compound | 40℃ | | | 60℃ | | |
|---|---|---|---|---|---|---|
| | pH9 | pH10 | pH11 | pH9 | pH10 | pH11 |
| Cellobiose (g/l) | 0.13 | 0.14 | 0.12 | 0.12 | 0.13 | 0.11 |
| Glucose (g/l) | 1.39 | 1.39 | 1.26 | 1.35 | 1.33 | 1.01 |
| Xylose (g/l) | 2.23 | 2.23 | 2.04 | 2.16 | 2.13 | 1.63 |
| Arabinose (g/l) | 0.27 | 0.27 | 0.27 | 0.27 | 0.27 | 0.26 |
| Formic acid (g/l) | 1.97 | 1.99 | 2.04 | 1.98 | 1.99 | 2.04 |
| Acetic acid (g/l) | 2.23 | 2.24 | 2.26 | 2.25 | 2.25 | 2.28 |
| Levulinic acid (g/l) | 0.22 | 0.22 | 0.22 | 0.24 | 0.24 | 0.24 |
| 5-hydroxymethylfurfural (g/l) | 0.07 | 0.05 | 0.07 | 0.09 | 0.08 | 0.08 |
| Furfural (g/l) | 0.17 | 0.16 | 0.10 | 0.16 | 0.14 | 0.08 |
| Absorbance at 280 nm | 1.57 | 1.56 | 1.35 | 1.63 | 1.48 | 1.36 |

**Table 5.** The composition of acid hydrolyzate detoxified with a combination of steam stripping and overliming.

| Compound | Before detoxification | After steam stripping[a)] | After overliming[b)] |
|---|---|---|---|
| Cellobiose (g/l) | 0.12 | 0.07 | 0.07 |
| Glucose (g/l) | 1.27 | 1.17 | 0.91 |
| Xylose (g/l) | 2.13 | 1.92 | 1.23 |
| Arabinose (g/l) | 0.29 | 0.19 | 0.17 |
| Formic acid (g/l) | 1.82 | 0.59 | 0.65 |
| Acetic acid (g/l) | 1.93 | 0.35 | 0.38 |
| Levulinic acid (g/l) | 0.19 | 0.16 | 0.15 |
| 5-hydroxymethylfurfural (g/l) | 0.09 | 0.05 | 0.05 |
| Furfural (g/l) | 0.18 | 0.01 | 0.01 |
| Absorbance at 280 nm | 1.93 | 1.11 | 0.93 |

a) The time of stripping is 120 min; b) The condition of overliming is at pH11 and 60 ℃ for 90 min.

From **Table 5**, it could be seen that the concentrations of formic, acetic acid and furfural were similar to that of steam stripping alone, indicating that overliming had very limited effect on the removal of these compounds [18]. The value of absorbance at 280nm was less than that of overliming alone because steam stripping could remove some furfural and phenolics. Sugar concentrations after two step detoxification were lower than both one step treatments even though the original concentration of each sugar was at very low level.

## 3.6. Fermentation of the Detoxified and Undetoxified Acid Hydrolyzates

The fermentability of three kinds of acid hydrolyzate, the undetoxified hydrolyzate, the hydrolyzate treated with steam stripping, and the hydrolyzate treated with a combination of steam stripping and overliming, had been investigated. Since the sugar contents in these hydrolyzates were too low, 45g/l xylose was added. The yeast *Pichia stipitis* CBS 5776 was used as the biocatalyst. **Figs. 2, 3, and 4** illustrated the fermentation courses including the change profiles of glucose, xylose, the product ethanol, the by-product xylitol, and the optical density (OD) of yeast cells.

As shown in **Fig. 2**, in the fermentation of undetoxified hydrolyzate, the utilization of sugars were very difficult. In 36h, only 0.68g/l glucose was consumed; after 48h, the remained 0.30g/l glucose kept untouched. Xylose was utilized very slowly before 48h, indicating a long period of adaptation was required. When the yeast adapted to the medium, a rapid consumption of xylose was observed, and only 0.60g/l xylose was left at 85h.

Ethanol, the main fermentation product, was produced in accordance with the consumption of sugars. The concentration of ethanol reached its highest value of 13.25 g/l at 85 h when xylose was utilized nearly completely (**Fig. 2**). After that ethanol concentration decreased, probably because the yeast used ethanol as the carbon source when the sugars used out. The trend of the formation of xylitol, the main by-product, was similar to that of ethanol. At 72h xylitol concentration reached its peak of 0.67g/l. The OD was increased constantly from 7.35 to 13.10.

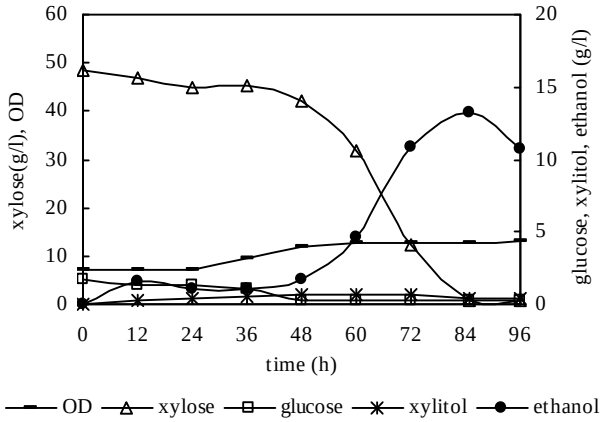


**Figure 2.** Changes in the parameters during the fermentation of undetoxified acid hydrolyzate with the addition of xylose 45g/l.

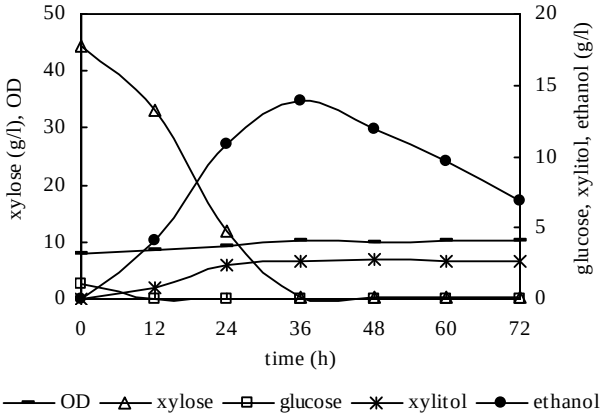


**Figure 3.** Changes in the parameters during the fermentation of acid hydrolyzate detoxified with steam stripping and the addition of xylose 45g/l.

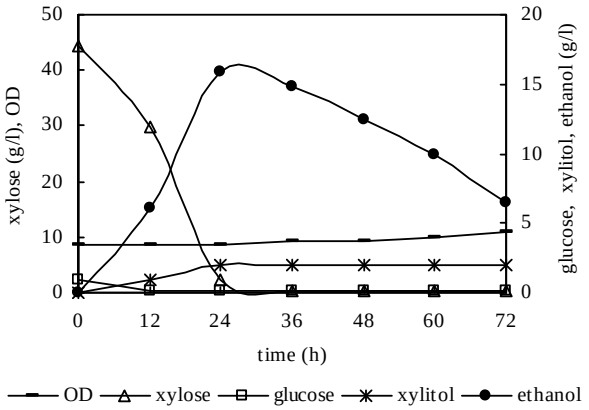


**Figure 4.** Changes in the parameters during the fermentation of acid hydrolyzate detoxified with a combination of steam stripping and overliming, and the addition of xylose 45g/l.

The fermentation of the hydrolyzate treated with steam stripping was more easily than that of undetoxified hydrolyzate as shown in **Fig. 3**. Glucose was exhausted in 12h. Xylose was consumed rapidly as well; in 36h only 0.38g/l xylose was left. Ethanol reached its highest value of 13.91g/l at 36h, compared to 85h in **Fig. 2**. Xylitol production increased rapidly in 24h, while the OD was increased constantly from 8.50 to 10.43. Compared with **Fig. 2**, the fermentablity of the hydrolyzate treated with steam stripping was improved significantly.

In the fermentation of the hydrolyzate treated with a combination of steam stripping and overliming, the sugar utilization and ethanol production were further improved compared with **Fig. 3.** As shown in **Fig. 4**, glucose was exhausted in 12h, while xylose was consumed substantially in 24h with a remaining concentration of 2.28g/l. The peak of ethanol concentration, 15.92 g/l, which was 80.34% of theoretical, appeared at 24h, a reasonable fermentation time for practical applications.

From the data above (**Figs. 2, 3, and 4**), it could be concluded that it is necessary to detoxify the acid hydrolyzate in order to ferment the sugars to ethanol. Steam stripping is an efficient method to detoxify the hydrolyzate. If combined with overliming, steam stripping could significantly improve the fermentability of the hydrolyzate in terms of sugar utilization and ethanol production.

## 4. CONCLUSIONS

The ability of yeast *Pichia stipitis* CBS 5776 adapted gradually on the fermentation medium containing the filtrate of steam exploded was so limited that detoxification methods must be adopted to remove these inhibitors existed in the filtrate. A combination of steam stripping and overliming was an effective method to remove the inhibitors in the steam exploded corn stover prehydrolyzate, and could improve the fermentability of *Pichia stipitis* CBS 5776. Steam stripping could remove volatile compounds and at a stripping time of 120min, 81% acetic acid and 59% formic acid were removed while furfural was stripped off completely from the acid hydrolyzate. Overliming could reduce the contents of furfural and phenolics presented in the acid hydrolyzate, however, sugars, especially pentoses, were also removed partially. When the acid hydrolyzate detoxified with a combination of steam stripping for 120min and overliming at pH11 and 60℃ for 90min, its fermentability was significantly improved. Xylose was consumed nearly completely in 24h with an ethanol yield of 15.92g/l, 80.34% of theoretical.

## ACKNOWLEDGMENTS

The authors acknowledge the financial supports from National Natural Science Foundation of China (Grant No.30871992), National High Technology Research and Development Program of China (Grant No. 2008AA 05Z401), and Natural Science Foundation of Jiangsu Higher Education of China (Grant No. 06KJA22015).

## REFERENCES

[1] Saha, B. C., Iten, L. B., Cotta, M. A. and Wu, Y. V. (2005) Dilute acid pretreatment, enzymatic saccharification and fermentation of wheat straw to ethanol. Proc. Biochem. **40**, 3693−3700.

[2] Lloyd, T. A. and Wyman, C. E. (2005) Combined sugar yields for dilute sulfuric acid pretreatment of corn stover followed by enzymatic hydrolysis. Bioresour. Technol., **96**, 1967−1977.

[3] Carrillo, F., Lis, M. J., Colom, X., Valldeperas, M. and Valldeperas, J. (2005) Effect of alkali pretreatment on cellulose hydrolysis of wheat straw: Kinetic study. Proc. Biochem., **40**, 3360−3364.

[4] Kapoor, M., Nair, L. M. and Kuhad, R. C. (2008) Cost-effective xylanase production from free and immobilized *Bacillus pumilus* strain MK001 and its application in saccharification of *Prosopis juliflora*. Biochem. Eng. J., **38**, 88−97.

[5] Viola, E., Cardinale, M., Santarcangelo, R., Villone, A. and Zimbardi, F. (2008) Ethanol from eel grass via steam explosion and enzymatic hydrolysis. Biomass Bioenerg., **32**, 613−618.

[6] Teymouri, F., Laureano-Perez, L., Alizadeh, H. and Dale, B. E. (2005) Optimization of the ammonia fiber explosion (AFEX) treatment parameters for enzymatic hydrolysis of corn stover. Bioresour. Technol., **96**, 2014− 2018.

[7] Saha, B. C. and Cotta, M. A. (2008) Lime pretreatment, enzymatic saccharification and fermentation of rice hulls to ethanol. Biomass Bioenerg., **32**, 971−977.

[8] Klinke, H. B., Thomsen, A. B. and Ahring, B. K. (2001) Potential inhibitors from wet oxidation of wheat straw and their effect on growth and ethanol production by *Thermoanaerobacter mathranii*. Appl. Microbiol. Biotechnol., **57**, 631−638.

[9] Mosier, N., Hendrickson, R., Ho, N., Sedlak, M. and Ladisch, M. R. (2005) Optimization of pH controlled liq-

uid hot water pretreatment of corn stover. Bioresour. Technol., **96**, 1986−1993.

[10] Xu, F., Sun, J. X., Liu, C. F. and Sun, R. C. (2006) Comparative study of alkali-and acidic organic solvent-soluble hemicellulosic polysaccharides from sugarcane bagasse. Carbohyd. Res., **341**, 253−261.

[11] Singh, P., Suman, A., Tiwari, P., Arya, N., Gaur, A. and Shrivastava, A. K. (2008) Biological pretreatment of sugarcane trask for its conversion to fermentable sugars. World J. Microbiol. Biotechnol., **24**, 667−673.

[12] McMillan, J. D. (1994) Pretreatment of lignocellulosic biomass. In: Himmel, M. E., Baker, J. O., Overend, R. P. (Eds), Enzymatic conversion of biomass for fuels production. American Chemical Society, Washington, DC, 292−324.

[13] Ohgren, K., Galbe, M. and Zacchi, G. (2005) Optimization of steam pretreatment of $SO_2$-impregnated corn stover for fuel ethanol production. Appl. Biochem. Biotechnol., **124**, 1055−1067.

[14] Zhu, J., Yong, Q., Chen, S., Xu, Y., Zhang, X. and Yu, S. (2008) Identification of degraded products during corn stover steam-explosion pretreatment. Chemistry and Industry of Forest Products, **29(2)**, 22−26.

[15] Roberto, I. C., Lacis, L. S., Barbosa, M. F. S. and de Mancilha, I. M. (1991) Utilization of sugar cane bagasse hemicellulosic hydrolysate by *Pichia stipitis* for the production of ethanol. Proc. Biochem., **26**, 15−21.

[16] Nigam, J. N. (2001) Development of xylose-fermenting yeast *Pichia stipitis* for ethanol production through adaptation on hardwood hemicellulose acid prehydrolysate. J. Appl. Microbiol., **90**, 208−215.

[17] Yu, Z. and Zhang, H. (2003) Pretreatments of cellulose pyrolysate for ethanol production by *Saccharomyces cerevisiae*, *Pichia sp.* YZ-1 and *Zymomonas mobilis*. Biomass Bioenerg., **24**, 257−262.

[18] Martinez, A., Rodriguez, M. E., York, S. W., Preston, J. F. and Ingram, L. O. (2000) Effects of $Ca(OH)_2$ treatments ("overliming") on the composition and toxicity of bagasse hemicellulose hydrolysates. Biotechnol. Bioeng., **69(5)**, 526−536.

[19] Yu, S., Wayman, M. and Parekh, S. K. (1987) Fermentation to ethanol of pentose-containing spent sulphite liquor. Biotechnol. Bioeng., **29**, 1144−1150.

[20] Chandel, A. K., Kapoor, R. K., Singh, A. and Kuhad, R. C. (2007) Detoxification of sugarcane bagasse hydrolysate improves ethanol production by *Candida shehatae* NCIM 3501. Bioresour. Technol., **98**, 1947−1950.

[21] Miyafuji, H., Danner, H., Neureiter, M., Thomasser, C., Bvochora, J., Szolar, O. and Braun, R. (2003) Detoxification of wood hydrolysates with wood charcoal for increasing the fermentability of hydrolysates. Enzyme Microb. Technol., **32**, 396−400.

[22] Jönsson, L. J., Palmqvist, E., Nilvebrant, N. O. and Hahn-Hägerdal, B. (1998) Detoxification of wood hydrolysates with laccase and peroxidase from white-rot fungus *Trametes versicolor*. Appl. Microbiol. Biotechnol., **49**, 691−697.

[23] Olsson, L. and Hahn-Hägerdal, B. (1996) Fermentation of lignocellulosic hydrolysates for ethanol production. Enzyme Microb. Technol., **18**, 312−331.

[24] Larsson, S., Reimann, A., Nilvebrant, N. O. and Jönsson, L. J. (1999) Comparison of different methods for the detoxification of lignocellulose hydrolyzates of spruce. Appl. Biochem. Biotechnol., 77−79, 91−103.

[25] Yu, S., Jeppsson, H. and Hahn-Hägerdal, B. (1995) Xylulose fermentation by *Saccharomyces cerevisiae* and xylose-fermenting yeast strains. Appl. Microbiol. Biotechnol., **44**, 314−320.

[26] Saddler, J. N., Ramos, L. P. and Breuil, C. (1993) Steam pretreatment of lignocellulosic residues. In: Bioconversion of forest and agricultural plant residues (Saddler, J. N., Ed.). CAB International Wallingford. UK, 73−91.

[27] Palmqvist, E. and Hahn-Hägerdal, B. (2000) Fermentation of lignocellulosic hydrolysates. II: inhibitors and mechanisms of inhibition. Bioresour. Technol., **74**, 25−33.

[28] Purwadi, R., Niklasson, C. and Taherzadeh, M. J. (2004) Kinetic study of detoxification of dilute-acid hydrolyzates by $Ca(OH)_2$. J. Biotechnol., **114**, 187−198.

 

**Natural Science, 2009, 1, 55-62** **NS**

# Synthesis of biodiesel from *Jatropha curcas* L. seed oil using artificial zeolites loaded with $CH_3COOK$ as a heterogeneous catalyst

**Wei Xue[1], You-Chun Zhou[1], Bao-An Song[1], Xia Shi[1], Jun Wang[1], Shi-Tao Yin[1], De-Yu Hu[1], Lin-Hong Jin[1], Song Yang[1,*]**

[1]Key Laboratory of Green Pesticide and Bioengineering, Ministry of Education of China, Center for Research and Development of Fine Chemicals, Guizhou University, Guiyang 550025, P. R. China; To whom correspondence should be addressed: Tel.: +86-851-362-0521, Fax: +86-851-362-2211.
Email: *jhzx.msm@gmail.com, *yangsdqj@gmail.com

Received 18 May 2009; revised 30 May 2009; accepted 10 June 2009.

## ABSTRACT

**An environmentally benign process was developed for the transesterification of *Jatropha curcas* L. seed oil with methanol using artificial zeolites loaded with potassium acetate as a heterogeneous catalyst. After calcination for 5 h at 823 K, the catalyst loaded with 47 wt.% $CH_3COOK$ exhibited the highest efficiency and best catalytic activity. The easily prepared catalysts were characterized by means of X-ray diffraction and IR spectroscopy, as well as Hammett indicator titration. The results revealed a strong dependence of catalytic activity on basicity. The optimum reaction conditions for transesterification of J*. *curcas* oil were also investigated. The methyl ester content in the biodiesel product exceeded 91% after 4h reaction at reflux temperature in the presence of 2% solid catalyst and no water washing process is needed during workup.**

**Keywords:** Biodiesel; Heterogeneous Catalyst; Artificial Zeolites; *Jatropha Curcas* L. seed Oil

## 1. INTRODUCTION

Biodiesel is a biodegradable and non-toxic renewable alternative to diesel fuel that is composed of mono-alkyl esters of long-chain fatty acids derived from vegetable oils or animal fats. Biodiesel is increasing in importance because of its benign impact on the environment. [1,2] Biodiesel is produced mainly through the transesterification of vegetable oils using short-chain alcohols, typically methanol or ethanol [3], because these are cheap and readily available from syngas, in which methanol is usually preferred. [4,5] Transesterification of vegetable oils with methanol, also called methanolysis, is typically carried out in the presence of homogeneous base or acid catalysts. Homogeneous base catalysts, including potassium hydroxide, sodium hydroxide and potassium and sodium alkoxides, such as $NaOCH_3$ [1], have higher catalytic activity than acid catalysts. Furthermore, since acid catalysts are more corrosive than base catalysts, base catalysis is usually preferred in commercial processes. [6] In the conventional homogeneous reaction, removal of the base after reaction is a major problem, since aqueous quenching results in the formation of stable emulsions and saponification, making the separation of methyl esters difficult and producing waste water. [7] However, the use of solid base catalysts can not only overcome those disadvantages, but also confer some advantages, such as the elimination of a quenching step (and associated contaminated water waste) during the work-up process and the scope to operate in continuous mode. [8,9] Therefore, environmentally friendly heterogeneous catalysts are promising for biodiesel production because of environmental constraints and potential simplification of existing processes.

Recently, heterogeneous catalysts used to catalyze the transesterification of vegetable oils to prepare fatty acid methyl esters (FAME) have attracted considerable attention. Wilson *et al*. [5] prepared a series of Li-promoted CaO catalysts with Li loading in the range 0.26−4.0 wt.% to catalyze the transesterification of glyceryl tributyrate and methanol. They found that the optimum loading correlated with the formation of an electron-deficient surface $Li^+$ species and associated-OH species at defect sites on the support. Lee *et al*. [10] reported a process for the production of biodiesel from vegetable oils using an $Na/NaOH/\gamma\text{-}Al_2O_3$ heterogeneous catalyst. Under optimized reaction conditions, this $Na/NaOH/\gamma\text{-}Al_2O_3$ heterogeneous base catalyst showed almost the same activity as a conventional homogeneous NaOH catalyst. However, the base catalyst had to be

prepared in special apparatus equipped with a nitrogen flow line and cold circulating water flow. These disadvantages restrict potential industrial applications. Xie *et al*. [11] developed a type of $Al_2O_3$-loaded $KNO_3$ solid base catalyst for the transesterification of soybean oil. The catalytic activity was ascribed to the presence of $K_2O$ and K-O-Al groups derived from $KNO_3$ or other potassium compounds during high-temperature calcination.

Zeolites have attracted much attention in the preparation of solid base catalysts. [12,13,14,15] The basicity and catalytic activity of these zeolites can be modulated through ion exchange of alkali and the occlusion of alkali metal oxides in zeolite cages by decomposition. However, the preparation procedures for these modified zeolites have some disadvantages. For ion-exchanged zeolites, the exchanged samples need to be washed with distilled, deionized water to remove excess alkali remaining in the ETS-10 zeolite cages. [13] Furthermore, the treatment process requires a long time and produces much waste water.

In the present study, a modified artificial zeolite for catalysis of the transesterification of *Jatropha curcas* L. seed oil was developed using a simple preparation process. This catalyst preparation technique has many advantages: (1) compared with ETS-10 and NaX zeolites, artificial zeolites are cheaper; (2) artificial zeolites are used directly as a support without any pretreatment; and (3) after impregnation with potassium acetate, artificial zeolite samples were dried and then simply calcined in a muffle furnace. Unlike NaX occluded catalysts, [13,14] artificial zeolite-supported potassium acetate was thermally decomposed in an uncontrolled manner and the catalyst sample was prepared easily. To the best of our knowledge, this is the first time that a catalyst of artificial zeolites loaded with $CH_3COOK$ has been adopted for biodiesel production from *J. curcas* oil, a plant belonging to the Euphorbiaceae family with seed oil that is non-edible and a good material for industrial biodiesel production. [16] After calcination for 5 h at 823 K, the artificial zeolite catalyst loaded with 47 wt.% $CH_3COOK$ exhibited the highest basicity and the best catalytic activity for the reaction. The catalytic activity was evaluated in terms of the methyl ester content of the product after transesterification of *J. curcas* oil. The optimum reaction conditions were determined using an orthogonal experimental method.

## 2. EXPERIMENTAL

### 2.1. Catalyst Preparation

Artificial zeolites ($Na_2O{\cdot}Al_2O_3{\cdot}xSiO_2{\cdot}yH_2O$) were obtained from Shanghai Qingxi Chemical Science and Technology Ltd. (Shanghai, China). $CH_3COOK$/artificial zeolite supported catalysts were prepared by impregnating artificial zeolites with an aqueous solution of potassium acetate. Samples with various $CH_3COOK$ loadings were impregnated for 12 h to ensure that the $CH_3COOK$ diffused and dispersed thoroughly over the surface and through the pores of the artificial zeolites. The samples were then dried overnight at 383 K and calcined (typically at 823 K) in air for 5 h to yield readily usable catalysts. In experiments, catalyst samples with loading amounts of 9,23,33,41,44,47 and 50 wt.% (relative to the total mass of the catalyst before calcination) were designated as 9%, 23%, 33%, 41%, 44%, 47% and 50% $CH_3COOK$/artificial zeolites, respectively. [11]

### 2.2. Catalyst Characterization

The basic strength (H_) of the solid base was assessed using Hammett indicators. [17,18,19] In our experiments, the following Hammett indicators were used: bromthymol blue (H_=7.2), phenolphthalein (H_=9.8), 2, 4-dinitroa-niline (H_=15.0), and nitroaniline (H_=18.4). Approximately 50 mg of the catalyst sample was shaken with 10 mL of anhydrous ethanolic solution of Hammett indicator and left to equilibrate for 2 h. [20] Then the color change of the solution was observed. When the solution exhibits a color change, this indicates that the basic strength of the catalyst is stronger than the indicator used. However, when the solution produces no color change, the basic strength of the catalyst is weaker than that of the indicator used. The basicity of the catalysts was determined by titration with a Hammett indicator and a 0.02 mol/L anhydrous ethanolic solution of benzene carboxylic acid. [6] It should be noted that Hammett indicator titration can only give qualitative information about the basic properties of catalysts.

X-Ray diffraction (XRD) patterns of the samples were recorded on a Rigaku D/MAX-2200 powder X-ray diffractometer with Cu $K_\alpha$ ($\lambda$=0.154nm) radiation using an acceleration voltage of 40 kV and a current of 30mA, over a $2\theta$ range of 0-65° with a step size of 0.04° at a scanning speed of 3°/min. The data were processed using DiffracPlus software. The phases were identified using the Power Diffraction File (PDF) database (JCPDS, International Center for Diffraction Data).

IR spectra of the samples were measured using the KBr pellet technique. Spectra were recorded on a Shimadzu IR-Prestige-21 spectrometer with resolution of 4 $cm^{-1}$ over the range 400-4000$cm^{-1}$.

### 2.3. Transesterification Reaction

Jatropha curcas oil was prepared by squeezing seeds of J. curcas from Luodian county, Guizhou Province, southwest China. The crude oil obtained was then further purified by filtering out solid impurities and refined to reduce the water content. According to gas chromatography (GC) analysis, the fatty acids of *J. curcas* oil consisted of: palmitic acid (12.47%), palmitoleic acid (2.10%), stearic acid (6.42%), oleic acid (32.04%), and

 

linoleic acid (42.47%). The acid value of the oil was approximately 2.63mg KOH/g, and an average molecular weight of 880g/mol was calculated from the saponification value (Sv=194mg KOH/g).

A 250-mL three-necked glass flask equipped with a water-cooled condenser, thermometer and magnetic stirrer was charged with 110.0g (125mmol, calculated from the average molecular weight) of *J. curcas* oil, different volumes of methanol and various amounts of catalyst. The mixture was vigorously stirred and refluxed for the required reaction time. After completion of methanolysis, the mixture was filtered and excess methanol was recovered by rotary evaporation. The liquid phase was transferred into a separatory funnel and allowed to settle; the upper layer, the biodiesel product, was analyzed by GC.

### 2.4. Analysis Methods

The external standard method was adopted for GC product analysis. An Agilent 6890GC instrument equipped with a flame ionization detector was used. The chromatographic conditions were as follows: column, HP-Innowax (30m× 0.32mm, 0.25μm); inlet temperature, 523K; detector temperature, 523K; split ratio, 20:1; oven temperature program, 463K for 3min, ramp at 15K/min to 513K, hold for 8min; injection volume, 1μL; carrier gas, $N_2$ at 1.0mL/min; air flow, 450mL/min; $H_2$ flow, 40mL/min.

## 3. RESULTS AND DISCUSSION

### 3.1. Basic Strength of the Catalyst

**Table 1** shows the basic strength of the parent artificial zeolite (entry 1) and various $CH_3COOK$/artificial zeolite catalysts calcined at different temperatures. The basic strength of catalyst samples with $CH_3COOK$ loading of ＜33wt.% and calcined at 823 K are in the range 7.2<H_＜9.8 (entries 2–4). The basic strength increased to 15.0＜H_＜18.4 when the $CH_3COOK$ loading exceeded 33 wt.% (entries 5–＜9). This indicates that there are at least two types of active base sites in the supported catalysts.

For loading of <33wt.%, the amount of $CH_3COOK$ is not enough to cover all of the support surface and incorporation of potassium ions into the vacancies of the support is mainly through strong salt-support or oxide-support interaction. [20] New active base species emerge when $CH_3COOK$ loading exceeds 33wt.%, indicating that $(CH_3COOK)_n$ -support interaction plays an important role in this process. However, the basic strength of 47 wt.% $CH_3COOK$/artificial zeolite calcined at a temperature less than 623 K showed no increase compared with the artificial zeolite (entries 1, 10, 11). This is likely because $CH_3COOK$ loaded onto the artificial zeolite is not decomposed at temperature less than 623 K. The catalysts calcined between 623 and 973 K exhibit similar basic strength (entries 12-15). According to the definition of Tanabe, [21] these catalyst samples, with base strength in the range 15.0＜H_＜18.4, can be regarded as strong bases.

### 3.2. Basicity of the Catalyst

**Table 2** summarizes the basicity of a series of $CH_3COOK$/artificial zeolite catalysts calcined at different temperatures, as determined using Hammett indicators. As shown in **Table 2**, the basicity of catalysts calcined at 823 K first increases and then decreases with the increasing $CH_3COOK$ loading (entries 2–8), with 47 wt.% $CH_3COOK$/artificial zeolite exhibiting the highest

**Table 1.** Basic strength of various $CH_3COOK$/artificial zeolite catalysts calcined at different temperatures.

| Entry | Samples | Calcination temperature (K) | Basic strength (H_) |
|---|---|---|---|
| 1 | Artificial zeolite | – | 7.2＜H_＜9.8 |
| 2 | Artificial zeolite | 823 | 7.2＜H_＜9.8 |
| 3 | 9%$CH_3COOK$/artificial zeolite | 823 | 7.2＜H_＜9.8 |
| 4 | 23%$CH_3COOK$/artificial zeolite | 823 | 7.2＜H_＜9.8 |
| 5 | 33%$CH_3COOK$/artificial zeolite | 823 | 15.0＜H_＜18.4 |
| 6 | 41%$CH_3COOK$/artificial zeolite | 823 | 15.0＜H_＜18.4 |
| 7 | 44%$CH_3COOK$/artificial zeolite | 823 | 15.0＜H_＜18.4 |
| 8 | 47%$CH_3COOK$/artificial zeolite | 823 | 15.0＜H_＜18.4 |
| 9 | 50%$CH_3COOK$/artificial zeolite | 823 | 15.0＜H_＜18.4 |
| 10 | 47%$CH_3COOK$/artificial zeolite | – | 7.2＜H_＜9.8 |
| 11 | 47%$CH_3COOK$/artificial zeolite | 523 | 7.2＜H_＜9.8 |
| 12 | 47%$CH_3COOK$/artificial zeolite | 623 | 15.0＜H_＜18.4 |
| 13 | 47%$CH_3COOK$/artificial zeolite | 723 | 15.0＜H_＜18.4 |
| 14 | 47%$CH_3COOK$/artificial zeolite | 923 | 15.0＜H_＜18.4 |
| 15 | 47%$CH_3COOK$/artificial zeolite | 973 | 15.0＜H_＜18.4 |

**Table 2.** Basicity of various $CH_3COOK$/artificial zeolite catalysts calcined at different temperatures.

| Entry | Samples | Calcination temperature (K) | Basicity (mmol KOH/g) |
|---|---|---|---|
| 1 | Artificial zeolite | – | 0 |
| 2 | Artificial zeolite | 873 | 0 |
| 3 | 9%$CH_3COOK$/artificial zeolite | 823 | 0.0246 |
| 4 | 23%$CH_3COOK$/artificial zeolite | 823 | 0.1393 |
| 5 | 33%$CH_3COOK$/artificial zeolite | 823 | 0.3122 |
| 6 | 41%$CH_3COOK$/artificial zeolite | 823 | 0.3527 |
| 7 | 47%$CH_3COOK$/artificial zeolite | 823 | 0.4058 |
| 8 | 50%$CH_3COOK$/artificial zeolite | 823 | 0.3786 |
| 9 | 47%$CH_3COOK$/artificial zeolite | – | 0.2079 |
| 10 | 47%$CH_3COOK$/artificial zeolite | 523 | 0.2540 |
| 11 | 47%$CH_3COOK$/artificial zeolite | 623 | 0.2832 |
| 12 | 47%$CH_3COOK$/artificial zeolite | 723 | 0.3689 |
| 13 | 47%$CH_3COOK$/artificial zeolite | 923 | 0.2956 |
| 14 | 47%$CH_3COOK$/artificial zeolite | 973 | 0.1654 |

basicity (0.4058 mmol KOH/g; entry 7). This is similar to the findings of Xie *et al*. [11] The calcination temperature also affects catalyst basicity. It is evident from **Table 2** that catalysts calcined at 823K had the highest basicity (entries 7, 9−14). It was noted that 47% $CH_3$ COOK/artificial zeolite without calcination had higher basicity than 23% $CH_3COOK$/artificial zeolite calcined at 823 K (0.2079 vs. 0.1393 mmol KOH/g, entries 9 and 4).

## 3.2 Basicity of the Catalyst

**Table 2** summarizes the basicity of a series of $CH_3COOK$/artificial zeolite catalysts calcined at different temperatures, as determined using Hammett indicators. As shown in **Table 2**, the basicity of catalysts calcined at 823 K first increases and then decreases with the increasing $CH_3COOK$ loading (entries 2−8), with 47 wt.% $CH_3COOK$/artificial zeolite exhibiting the highest basicity (0.4058 mmol KOH/g; entry 7). This is similar to the findings of Xie *et al*. [11] The calcination temperature also affects catalyst basicity. It is evident from **Table 2** that catalysts calcined at 823 K had the highest basicity (entries 7, 9−14). It was noted that 47% $CH_3COOK$/artificial zeolite without calcination had higher basicity than 23% $CH_3COOK$/artificial zeolite calcined at 823 K (0.2079 vs. 0.1393 mmol KOH/g, entries 9 and 4).

## 3.3. Lnfluence of Catalyst Preparation Conditions

### 3.3.1. Lnfluence of $CH_3COOK$ Loading

The catalytic activity of the catalysts was evaluated by comparing the FAME content of the transesterification products. The effect of $CH_3COOK$ loading on the catalytic activity is shown **Fig. 1**. As the $CH_3COOK$ loading increases from 9% to 47%, the methyl ester content increases. The highest methyl ester content (91.58%) was obtained for 47 wt.% $CH_3COOK$ loading. However, the FAME content decreased slightly for a further increase in $CH_3COOK$ loading, which may be due to partial covering of basic sites by $K_2O$ species from the excess $CH_3COOK$ on the surface of the composite. It is important to point out that the conversion decreased significantly when potassium salt loading exceeded the critical limit for the transesterification of soybean. [11]

### 3.3.2. Influence of Calcination Temperature

**Figure 2** shows the influence of calcination temperature on the catalytic activity in the temperature range from 523 to 923 K. The optimal calcination temperature observed was 823 K. At this temperature, the methyl ester content reached 91.58%. However, when the calcination temperature increased to 923 K, the catalyst activity decreased. Such results are in line with the basicity properties shown in **Table 2**, indicating that higher basicity results in higher conversion and higher methyl ester content. However, the FAME content obtained using 47 wt.% $CH_3COOK$/artificial zeolite calcined at 523 K is lower than that obtained using 23 wt.% $CH_3COOK$/artificial zeolite calcined at 823 K, although the basicity of the former is higher than that of the latter (0.2540 vs. 0.1393 mmol KOH/g). This implies that basicity is the most important, but not the only factor affecting the activity of these supported catalysts.

## 3.4. FTIR Analysis

IR spectroscopy was used to investigate the $CH_3COOK$/artificial zeolite catalysts. The results are shown in **Fig. 3**. For the parent artificial zeolite, two absorption bands at

 

**Table 3.** Results of orthogonal experiment L9_3_4 for base-catalyzed transesterification and range analysis.

| Experimental no. | Factors and levels | | | Experimental results |
|---|---|---|---|---|
| | A | B | C | Methyl ester content(%) |
| 1 | 1 | 1 | 1 | 42.35 |
| 2 | 1 | 2 | 2 | 65.02 |
| 3 | 1 | 3 | 3 | 62.38 |
| 4 | 2 | 1 | 3 | 74.39 |
| 5 | 2 | 2 | 1 | 91.08 |
| 6 | 2 | 3 | 2 | 81.85 |
| 7 | 3 | 1 | 2 | 62.56 |
| 8 | 3 | 2 | 3 | 88.89 |
| 9 | 3 | 3 | 1 | 87.12 |
| I | 56.58 | 59.77 | 71.03 | |
| II | 82.44 | 81.66 | 75.51 | |
| III | 79.52 | 77.12 | 72.00 | |
| R | 25.86 | 21.90 | 4.48 | |

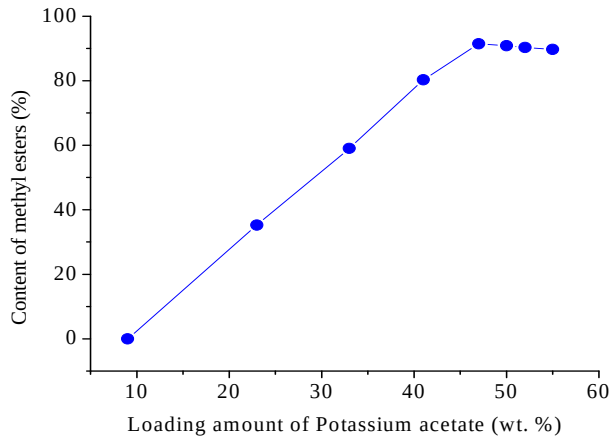


**Figure 1.** Influence of $CH_3COOK$ loading on the content of methyl esters. Reaction conditions: methanol/oil molar ratio, 10:1; catalyst amount, 2wt.%; reaction time, 4h; and methanol reflux temperature.

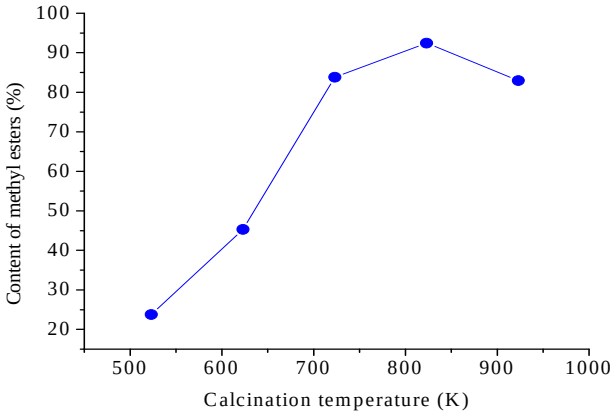


**Figure 2**. Influence of calcination temperature on the content of methyl esters. Reaction conditions: methanol/oil molar ratio, 10:1; catalyst amount, 2wt.%; reaction time, 4h; and methanol reflux temperature.

3440 and 1650cm$^{-1}$ were attributed to stretching and bending vibrations of physically absorbed water, respectively. $CH_3COOK$/artificial zeolites catalysts calcined at high temperature (curves b, c, d, f and g in **Fig. 3**) showed intense absorption at approximately 3440 cm$^{-1}$, which could be assigned to $\nu_{OH}$ stretching vibrations of hydroxyl groups attached to the support. Such hydroxyl groups are mainly formed by the reaction of surface-absorbed water with the support during the activation by calcination. [22] When the catalyst samples were calcined at higher temperatures (curves d, f and g in **Fig. 3**), there was very little absorbed water on the support surface. However, there was still a strong absorption peak at~1650cm$^{-1}$. This indicates that the peak at 1650cm$^{-1}$ was mainly due to surface hydroxyl groups and that these surface OH groups were possibly active sites, as reported by Xie and Huang. [23]

Furthermore, the absorption broad band at ~3440cm$^{-1}$ could be partly assigned to stretching vibrations of Al-O-K or Si-O-K groups. [24,25,26] According to Stork and Pott, [27] $K^+$ ions may replace the protons of hydroxyl groups attached to the support during activation. Thus, $K^+$ ions from $CH_3COOK$ could form Al-O-K or Si-O-K groups by replacing the protons of hydroxyl groups attached to the artificial zeolites during activation by calcination, and can probably be considered to be another active basic species of this catalyst in transesterification.

As observed from **Fig. 3**, the absorption intensity at ~3440cm$^{-1}$ increased with the $CH_3COOK$ loading (curves b-d), indicating that an increase in basic sites resulted in an increase in catalytic activity, which is in accordance with the results shown in **Fig. 1**. On the other hand, the intensity of the abso0rption at 3440cm$^{-1}$ decreased at higher calcination temperatures (curves d, f and g), indicating a decrease in basic sites, in line with Hammett basicity measurement (**Table 2**). The absorption peak at ~1552cm$^{-1}$ can be assigned to asymmetric vibration of $COO^-$ [28] of $CH_3COOK$ (curve e), which disappeared after calcination at 823K (curve d), demonstrating that $CH_3COOK$ decomposed completely after calcination at 823 K. In addition, there were some other absorption peaks at ~400-1400cm$^{-1}$ for all samples, which can be attributed to Al-O (or Si-O) symmetric stretching and ring vibration in Al-O and Si-O tetraheda formed through the oxygen atom.

## 3.5. XRD Analysis

XRD patterns of artificial zeolites and $CH_3COOK$/artificial zeolite samples with different $CH_3COOK$ loading are shown in **Fig. 4**. The XRD pattern of artificial zeolites is irregular, which may be related to their structure. After calcination of artificial zeolites loaded with $CH_3COOK$, more regular and distinct diffraction peaks (* and □ in **Fig. 4**) appeared in the XRD patterns.

 

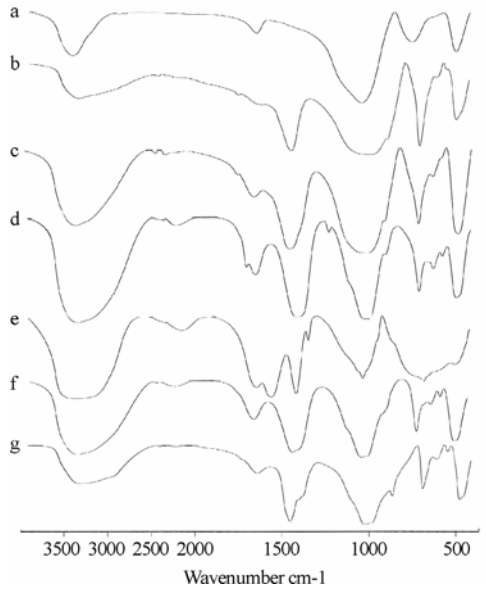


**Figure 3.** FTIR spectra: (a) artificial zeolites; (b) 33% $CH_3$COOK/artificial zeolites calcined at 823 K for 5 h; (c) 41% $CH_3COOK$/artificial zeolites calcined at 823 K for 5 h; (d) 47% $CH_3COOK$/artificial zeolites calcined at 823 K for 5 h; (e) 47% $CH_3COOK$/artificial zeolites without calcination; (f) 47% $CH_3COOK$/artificial zeolites calcined at 923 K for 5 h; and (g) 47% $CH_3$COOK/artificial zeolites calcined at 973 K for 5 h.

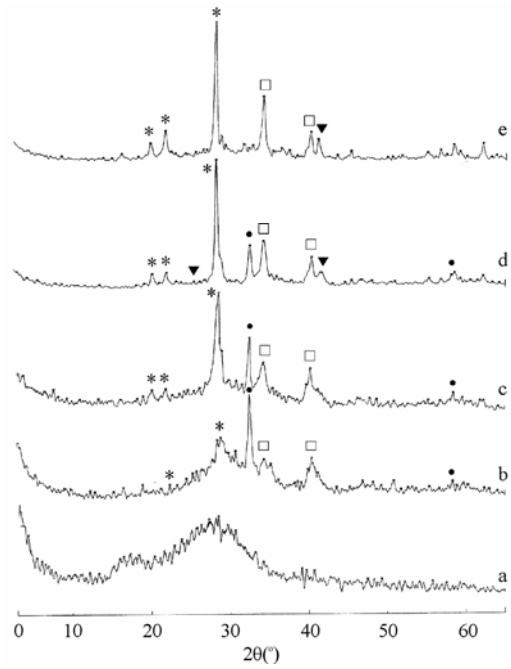


**Figure 4**. XRD patterns: (a) parent artificial zeolites; (b) 33% $CH_3COOK$/artificial zeolites calcined at 823 K for 5 h; (c) 41% $CH_3COOK$/artificial zeolites calcined at 823 K for 5 h; (d) 47% $CH_3COOK$/artificial zeolites calcined at 823 K for 5 h; and (e) 47% $CH_3COOK$/artificial zeolites calcined at 923 K for 5 h. * $KAlSiO_4$, Kalsilite; □ $K_{0.85}Na_{0.15}AlSiO_4$; ● $K_2Al_2O_4$; and ▼ $K_2O$.

This is possibly due to the reaction of $CH_3COOK$ with the support during activation, resulting in the more regular and stable structure necessary for catalysis.

As shown in **Fig. 4**, when the $CH_3COOK$ loading was below 47wt.% (curves b and c), the XRD patterns contained only diffraction peaks ($2\theta$ =20.5°,22.3°,28.6°, 34.6°,40.6°) assigned to new species formed by reaction between $CH_3COOK$ and the support during the activation process. These diffraction peaks can probably be ascribed to two new species, KAlSiO4 (Kalsilite; *) and $K_{0.85}Na_{0.15}AlSiO_4$ (□), formed by the movement of $K^+$ from $CH_3COOK$ into the crystal lattices of the support and subsequent reaction. There were no characteristic peaks for $CH_3COOK$ or $K_2O$, probably due to good dispersion of $K^+$ derived from $CH_3COOK$ on artificial zeolites in the form of various compounds, while a $K_2O$ phase undetectable by XRD may have dispersed onto the artificial zeolite surface as a monolayer. [29] In addition, $2\theta$ diffraction peaks at 32.8° and 58.6° can probably be ascribed to $K_2Al_2O_4$ (•), also obtained by reaction between $K^+$ and the support.

However, when the $CH_3COOK$ loading increased to 47 wt.%, the characteristic XRD peaks of $K_2O$ ($2\theta$= 25.8°,41.9°) were detected (curve d in **Fig. 4**). According to the results shown in **Fig. 1** and **Table 2**, this $K_2O$ species may account for the high catalytic activity and basicity of the catalyst, because 47% $CH_3COOK$/artificial zeolites calcined at 823K for 5h exhibited the highest catalytic activity and basicity. Furthermore, when the calcination temperature increased to 923K, the characteristic XRD peak at $2\theta$ =32.8° vanished, presumably because $K_2Al_2O_4$ (•) was destroyed at higher calcination temperatures.

Taken together, the characterization results indicate that $K_2O$ (derived from $CH_3COOK$) and surface hydroxyl groups, as well as Al-O-K (or Si-O-K) groups, were probably the active sites mainly responsible for the transesterification of *J. curcas* oil with methanol.

### 3.6. Optimization of the Transesterification Reaction

For the transesterification reaction, orthogonal experiments were carried out to determine the optimum reaction conditions. The effects of various factors on the reaction were also studied. The orthogonal scheme chosen and the data obtained are shown in **Table 3**.

As shown in **Table 3**, the extent to which the transesterification of *J. curcas* oil was affected in terms of the range (R) value was A＞B＞C, namely, oil/methanol ratio (A) first, followed by catalyst amount (B) and reaction time (C). Taking the FAME content into account, the optimum reaction conditions were $A_2B_2C_2$; namely, oil/methanol ratio, 1:10; catalyst amount, 2wt.%; and reaction time, 4h.

The molar ratio of *J. curcas* oil to methanol is the

 

most important factor affecting the transesterification to methyl esters (**Table 3**). Theoretically, three moles of methanol are required for one mole of triglyceride to yield one mole of glycerol and three moles of FAME. However, a slight excess of methanol is required to drive the equilibrium to the product side, because the transesterification reaction is reversible. [1] With an increase in the oil/methanol molar ratio, the conversion increased considerably. However, further addition of methanol not only had no significant effect on the conversion, but also seriously affected glycerine separation due to the increase in solubility. [30] Thus, the optimum molar ratio of *J. curcas* oil to methanol to produce methyl esters was 1:10.

The amount of catalyst is another important factor that affects the reaction. With no catalyst, transesterification does not occur. When the amount of catalyst was insufficient, the FAME content was very low (entries 1, 4, 7). Saponification took place when the amount of catalyst was increased to 3%, leading to product emulsion and making separation difficult. The FAME content and product yield were also influenced (entries 3, 6, 9). As revealed in orthogonal experiments, 2 wt.% catalyst was appropriate for this transesterification reaction.

The final factor affecting transesterification is the reaction time. When the reaction time is too short, the conversion of vegetable oil to methyl esters is incomplete, and conversion increases with the reaction time. However, when the reaction reaches equilibrium, prolonged reaction time does not increase the FAME content of the product, but increases the cost for biodiesel production. In homogeneous base-catalyzed transesterification, the reaction time is usually less than 1 h. For heterogeneous transesterification the reaction time needs to be longer, because the system components, the base catalyst, methanol and *J. curcas* oil in the present study, require a longer contact time. According to orthogonal experiments, an optimum reaction time of 4 h was chosen.

An experiment was carried out under above optimum reaction conditions, a product yield of 94.27% and methyl ester content of 91.58% were obtained after transesterification.

## 4. CONCLUSIONS

Easily prepared solid-base catalysts using artificial zeolites as a support were developed for the transesterification of *J. curcas* oil with methanol to produce biodiesel. The $CH_3COOK$/artificial zeolites solid catalysts exhibited high catalytic activity in the transesterification process. The methyl ester content exceeded 91% when the catalyst with 47 wt.% $CH_3COOK$ was calcined at 823 K for 5 h. Catalyst characterization revealed that $K_2O$, surface hydroxyl groups and Al-O-K (or Si-O-K) groups are the main basic sites. Furthermore, the activity of the catalysts depends strongly on their basicity. Orthogonal experiments revealed the following optimum reaction conditions: oil/methanol ratio, 1:10; catalyst amount, 2wt.%; and reaction time, 4h. No water washing step is needed thus no waster water was produced during this process. The information mentioned above establishes certain basis for industrial biodiesel production from *J. curcas* seed oil using the heterogeneous catalysts. Further investigations on the reaction mechanism and active sites are under way in our laboratory.

## ACKNOWLEDGEMENT

This work is financially supported by Program for New Century Excellent Talents in Chinese University (NCET-05-0818), Key Science and Technology Project of Guizhou Province (No. 20076004), and the National Key Technology R&D Program (2006BAD07A12).

## REFERENCES

[1] Ma, F. and Hanna, M. A. (1999) Biodiesel production: A review. Bioresour Technol, **70**, 1−15.

[2] Ramadhas, A. S., Jayaraj, S. and Muraleedharan C. (2005) Biodiesel production from high FFA rubber seed oil. Fuel, **84**, 335−340.

[3] Schuchardt, U., Sercheli, R. and Vargas, R. M. (1998) Transesterification of vegetable oils: A review. J Braz Chem Soc, **9**, 199−210.

[4] Graboski, M. S. and McCormick, R. L. (1998) Combustion of fat and vegetable oil derived fuels in diesel engines. Prog Energy Combust Sci, **24**, 125−164.

[5] Watkins, R. S., Lee, A. F. and Wilson, K. (2004) Li-CaO catalysed tri-glyceride transesterification for biodiesel applications. Green Chem, **6**, 335−340.

[6] Xie, W. L. and Li, H. T. (2006) Alumina-supported potassium iodide as a heterogeneous catalyst for biodiesel production from soybean oil. J Mol Catal A: Chem, **255**, 1−9.

[7] Gryglewicz, S. (1999) Rapeseed oil methyl esters preparation using heterogeneous catalysts. Bioresour Technol, **70**, 249−253.

[8] Ono, Y. and Baba, T. (1997) Selective reactions over solid base catalysts. Catal Today, **38**, 321−337.

[9] Clark, J. H. and Macquarrie, D. J. (1996) Environmentally friendly catalytic methods. Chem Soc Rev, **25**, 303−310.

[10] Kim H J, Kang B S, Kim M J, Park Y M, Kim D K, Lee J S, Lee K Y. Transesterification of vegetable oil to biodiesel using heterogeneous base catalyst. Catal Today 2004; 93−95: 315−320.

[11] Xie, W. L., Peng, H. and Chen, L. G. (2006) Transesterification of soybean oil catalyzed by potassium loaded on alumina as a solid-base catalyst. Appl Catal A: Gen, **300**, 67−74.

[12] Bordawekar, S. V. and Davis, R. J. (2000) Probing the basic character of alkali-modified zeolites by $CO_2$ adsorption microcalorimetry, butene isomerization, and toluene alkylation with ethylene. J Catal, **189**, 79−90.

[13] Suppes, G. J., Dasari, M. A., Doskocil, E. J., Mankidy, P. J. and Goff, M. J. (2004) Transesterification of soybean

 

oil with zeolite and metal catalysts. Appl Catal A: Gen, **257**, 213–223.

[14] Doskocil, E. J. and Mankidy, P. J. (2003) Effects on solid basicity for sodium metal and metal oxide occluded NaX zeolites. Appl Catal A: Gen, **252,** 119–132.

[15] Leclercq, E., Finiels, A. and Moreau C. (2001) Transesterification of rapeseed oil in the presence of basic zeolites and related solid catalysts. J Am Oil Chem Soc, **78**, 1161–1165.

[16] Gubitz, G. M., Mittelbach, M. and Trabi, M. (1999) Exploitation of the tropical oil seed plant Jatropha curcas L. Bioresour Technol, **67**, 73–82.

[17] Forni, L. (1974) Comparison of the methods for the determination of surface acidity of solid catalysts. Catal Rev, **8**, 65–115.

[18] Gorzawski, H. and Hoelderich, W. F. (1999) Preparation of superbases and their use as catalysts for double-bond isomerization. J Mol Catal A: Chem, **144**, 181–187.

[19] Xie, W. L., Huang, X. M. and Li, H. T. (2007) Soybean oil methyl esters preparation using NaX zeolites loaded with KOH as a heterogeneous catalyst. Bioresour Technol, **98**, 936–939.

[20] Chen, Y. and Zhang, L. F. (1992) Surface interaction model of γ-alumina-supported metal oxides. Catal Lett, **12**, 51–62.

[21] Tanabe, K. (1985) Catalysis by acids and bases. in: B. Imelik, C. Nacceche, G. Condurier, Y. BenTaarti, J. C. Vedrine (Eds.), Elsevier, Amsterdam, 1–1.

[22] Nakamoto, K. (1970) Infrared spectra of inorganic and coordination compounds. John Wiley, New York, 98–98.

[23] Xie, W. L. and Huang, X. M. (2006) Synthesis of biodiesel from soybean oil using heterogeneous KF/ZnO catalyst. Catal Lett, **107**, 53–59.

[24] Krupay, B. W. and Amenomiya, Y. (1981) Alkali-promoted alumina catalysts: I. Chemisorption and oxygen exchange of carbon monoxide and carbon dioxide on potassium-promoted alumina catalysts. J Catal, **67**, 362–370.

[25] Iordan, A., Kappenstein, C., Colnay, E. and Zaki, M. I. (1998) Surface contribution to the interfacial chemistry of potassium modified oxide catalysts. J Chem Soc Faraday Trans, **94**, 1149–1156.

[26] Amenomiya, Y. and Pleizier, G. (1982) Alkali-promoted alumina catalysts: II. Water-gas shift reaction. J Catal, **76**, 345–353.

[27] Stork, W. H. J. and Pott, G. T. (1974) Studies of compound formation on alkali/γ-aluminum oxide catalyst systems using chromium, iron, and manganese luminescence. J Phys Chem B, **78**, 2496–2506.

[28] Bilger, S., Syskakis, E., Naoumidis, A. and Nickel, H. (1992) Sol-gel synthesis of strontium-doped lanthanum manganite. J Am Ceram Soc, **75**, 964–970.

[29] Jiang, D. E., Zhao, B. Y., Xie, Y. C., Pan, G. C., Ran, G. P. and Min, E. Z. (2001) Structure and basicity of γ-Al2O3-supported MgO and its application to mercaptan oxidation. Appl Catal A: Gen, **219**, 69–78.

[30] Meher, L. C., Sagar, D. V. and Naik, S. N. (2006) Technical aspects of biodiesel production by transesterification-a review. Renew Sust Energy Rev, **10**, 248–268.

 

# Call for Papers

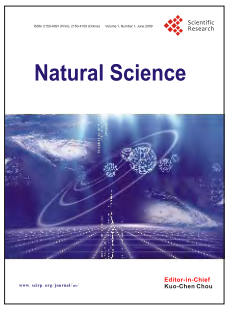


# Natural Science

**A Journal Published by Scientific Research Publishing, USA**
**www.scirp.org/journal/ns**



Natural Science is an international journal dedicated to the latest advancement of natural sciences. The goal of this journal is to provide a platform for scientists and academicians all over the world to promote, share, and discuss various new issues and developments in different areas of natural sciences. All manuscripts must be prepared in English, and are subject to a rigorous and fair peer-review process. Accepted papers will immediately appear online followed by printed hard copy. The journal publishes original papers including but not limited to the following fields:

- **Astronomy & Space Sciences**
  - Astronomy
  - Astrophysics
  - Atmospheric Science
  - Space Physics
- **Earth Science**
  - Geography
  - Geology
  - Geophysics/Geochemistry
  - Oceanography
- **Chemistry**
  - Analytical Chemistry
  - Biochemistry
  - Computational Chemistry
  - Inorganic Chemistry
  - Organic Chemistry
  - Physical Chemistry
- **Life Science**
  - Cell Biology
  - Computational Biology
  - Genetics
  - Immunology
  - Medicine/Diseases
  - Microbiology
  - Molecular Biology
  - Neuroscience
  - Pharmacology/Toxicology
  - Physiology
  - Psychology
  - Virology
- **Physics**
  - Applied Physics
  - Atomic, Molecular, and Optical Physics
  - Biophysics
  - High Energy/Particle Physics
  - Material Science
  - Plasma Physics
- **Others**
  - Education
  - History of Science
  - Science and Innovations

We are also interested in: 1) Short Reports—2-5 page papers where an author can either present an idea with theoretical background but has not yet completed the research needed for a complete paper or preliminary data; 2) Book Reviews—Comments and critiques.

## Notes for Intending Authors

Submitted papers should not be previously published nor be currently under consideration for publication elsewhere. Paper submission will be handled electronically through the website. For more details, please access the website.

## Website and E-Mail

http://www.scirp.org/journal/ns ns@scirp.org

**Natural Science, 2009, 1, 1-62**
Published Online June 2009 in SciRes (http://www.scirp.org/journal/ns).

# TABLE OF CONTENTS

## Volume 1, Number 1, June 2009



 

ISSN: 2150-4091